ELECTRONIC TRANSPORT IN POLYPYRROLE FILMS

Inaugural-Dissertation

zur
Erlangung des Doktorgrades der
Mathematisch-Naturwissenschaftlichen Fakultät
der Heinrich-Heine-Universität Düsseldorf

vorgelegt von
Carlos César Bof' Bufon
aus Linhares - Brasilien

Düsseldorf
November 2006

Aus dem Institut für Experimentelle Physik der kondensierten
Materie der Heinrich-Heine-Universität Düsseldorf

Gedruckt mit der Genehmigung der
Mathematisch-Naturwissenschaftlichen Fakultät der
Heinrich-Heine-Universität Düsseldorf

Referent: Prof. Dr. Thomas Heinzel

Koreferent: Prof. Dr. Klaus Schierbaum

Tag der mündlichen Prüfung: 18.01.2007

to my Mother

Table of Contents

Abstract

The effects of the polymerization-temperature, -potential as well as of voltammetric cycling on the chain length and the conductivity of polypyrrole (PPy) films are investigated. The studies provide further proof for the existence of at least two different types of PPy, the so-called PPy I and PPy II. The generation and control of these different types of PPy depends on the polymerization conditions. UV-vis measurements demonstrate that PPy II comprises significantly shorter chains than PPy I (8-12 vs. 32-64 units); moreover, both film conductivity and localization length are found to increase with the fraction of PPy II. A metal-insulator transition is observed in the galvanostatically grown samples by decreasing the polymerization temperature, while the potentiostatically grown films exhibit a correlation between both the chain and localization lengths. The counter-intuitive relationship between conductivity and chain length is interpreted in terms of disorder-dominated transport, in which the shorter chains of PPy II support the formation of delocalized electronic states, thereby increasing the conductivity.

A novel technique used for deposition and patterning of PPy films prepared by vapor-phase polymerization is demonstrated. This technique allows the deposition of the PPy thin films (between 6 nm and 170 nm) with low roughness onto a processed silicon substrate. The PPy thin films behave as granular systems. The system shows an electronic transport strongly influenced by Coulomb interactions. In addition, a PPy thin film can be used as an oxygen detector and the operation of a PPy thin-film field-effect transistor at room temperature is demonstrated. Transport measurements indicate that the transistor works as Schottky barrier-type field-effect transistor.

Zusammenfassung

Die vorliegende Arbeit befasst sich mit dem Einfluss von Polymerisationstemperatur und -potential sowie zyklischer Voltammetrie auf Kettenlänge und Leitfähigkeit von Polypyrrol (PPy)-Filmen. Die Untersuchungen untermauern die Existenz von mindestens zwei verschiedenen Arten von PPy, bezeichnet als PPy I und PPy II. Die Erzeugung dieser verschiedenen PPy-Arten lässt sich über die Polymerisationsbedingungen steuern. UV-vis-Messungen zeigen, dass PPy II aus wesentlich kürzeren Ketten besteht als PPy I (8 bis 12 bzw. 32 bis 64 Einheiten). Weiterhin steigen sowohl Leitfähigkeit als auch Korrelationslänge mit dem PPy II-Gehalt des Films an. In galvanostatisch gewachsenen Proben beobachtet man einen Metall-Isolator-Übergang, wenn die Polymerisationstemperatur reduziert wird, während potentiostatisch gewachsene Filme eine Korrelation zwischen Kettenlänge und Korrelationslänge aufweisen. Der zunächst unerwartete Zusammenhang zwischen Kettenlänge und Leitfähigkeit wird im Rahmen eines durch Unordnung dominierten Transportmechanismus interpretiert: Die kürzeren Ketten des PPy II unterstützen die Entstehung von delokalisierten elektronischen Zuständen und erhöhen dadurch die Leitfähigkeit.

Es wird eine neue Technik zur Deposition und Strukturierung von PPy-Filmen durch Gasphasenpolymerisation demonstriert. Diese Methode erlaubt die Herstellung von dünnen PPy-Filmen (zwischen 6nm und 170nm) mit geringer Rauhigkeit auf einem vorstrukturierten Siliziumsubstrat. Der dünne Film verhält sich wie ein granulares System. Der elektronische Transport in diesem System ist stark durch Coulomb-Wechselwirkungen beeinflusst.

Dünne PPy-Filme können als Sauerstoff-Detektoren verwendet werden, zudem wurde die Funktion eines PPy-Dünnschicht Feldeffekttransistors bei Raumtemperatur demonstriert. Transportmessungen weisen darauf hin, dass die Funktionsweise dieses Transistors mit der eines Schottky-Barrieren-Feldeffekttransistors vergleichbar ist.

Motivation and Objectives

Motivation

The idea of plastic electronics is an issue that still sounds strange, even considering that since the first observation of electric conductivity in iodine oxidized polypyrrole 43 years have already past [1, 2, 3]. In addition, the majority of polymer materials behaves first and foremost insulating: they were used, studied and developed as insulators in the first place. By an additional doping, these polymers can become either semiconducting or conducting. This was the discovery of A. J. Heeger, A. G. MacDiarmid and H. Shirakawa, winners of the Nobel Prize in Chemistry in 2000. They showed that polyacetylene doped by iodine can reach a state of high electrical conductivity comparable to the level of metals [4, 5].

Therefore, with the possibility of controlling the electrical characteristics of polymers by external doping, a novel category of electronic components, with additional features such as low-cost production and flexibility, became more attractive to the industry. The applications can be separated in two groups according to their principle of operation. The first one utilizes the high conductivity as main property. Conducting adhesives, antistatic clothes and electronic devices like diodes and transistors are examples. Chemical and biochemical sensors, artificial muscles and optical devices, like those used in modern organic displays are examples of the second group which uses the electroactivity properties of conducting polymers.

In order to explore the electroluminescence properties, an *organic light-emitting diode* (OLED) was first made by placing between two metallic contacts a semiconducting film of poly(p-phenylenevinylene) [6]. Today, it is possible to find OLEDs in applications varying from displays of mobile phones to 40 inches TV screens. The *organic field-effect transistor* (OFET) was also developed. The first OFET [7] was processed by using the polymer as an active layer upon a pre-patterned structure of doped-Si/SiO_2/metalic contacts, and nowadays the integrated all-polymer field-effect transistor is a reality. Wherever the required clock frequency is not high (kHz regime for instance), the application of organic devices are viable. In terms of fundamental research, the electrical transport in conducting polymers as well as the challenges to improve the crystallinity of the material, among others issues, have kept researchers busy. Despite the advances already reported, fundamental research is still necessary to support the fast technological progress that organic electronics has achieved in the last years [8].

Among the conducting polymers, polypyrrrole (PPy) has become one of the most studied conductive polymers in the past decade [9]. When compared to other semiconducting polymers, it combines advantages such as low oxidation potential, solubility in water of the pyrrole monomers [10, 11, 12], high conductivity (1000 S/cm) at room temperature [13, 14, 15], as well as stability of charged samples under ambient conditions [1]. These properties make PPy both commercially and scientifically interesting. The low oxidation potential, for instance, allows polymerization in water.

The application of PPy films as active layers in sensors has been demonstrated [11], i.e., in gas detectors for NH_3, NO_2 or H_2S [18, 19, 20, 21], or as key elements in biosensors for enzymes and antibodies [22]. PPy has also been applied as artificial muscles [23], antistatic layers, anticorrosion coatings [24], batteries and supercapacitors [11, 12, 25]. Recently, a field effect has been observed in PPy nanowires prepared electrochemically from porous alumina templates [26]. Furthermore, it has been shown that chemical synthesis of PPy films from pyrrole vapor [11, 27] on a patterned Fe(III)/Fe(II) oxidizing film enables the operation of transistors [28]. Full utilization of this potential, however, is hampered by the poor crystallinity of PPy [29], and by the difficulties in patterning the films.

The electric transport in PPy films and fibers reflects the amorphous character the material despite of some indications of local ordering. The picture of a system formed by metallic grains separated by tunnel barriers [30, 31] has been widely used to explain a large fraction of

---

[1] 10% drop in conductivity after ∼6 months exposure to the atmosphere [16, 17]

the measurements performed. By manipulating some of the synthesis parameters, it is possible to change the degree of charge localization. The changes in the degree of localization can be direct measured, e.g. by the temperature dependence of the conductivity or by reflectivity measurements in the far infrared [32].

Objectives

The aim of this work was to investigate the electrical properties of PPy films systematically, in particular their dependence on various synthesis and measurement parameters, in order to gain a deeper understanding of the transport properties as well as to find novel applications of this versatile material.

Chapter 1

Introduction

1.1 Synthesis of polypyrrole

Polypyrrole (PPy) is synthesized by polymerization of the monomer pyrrole (Py) either electrochemically or chemically, a process that takes place via oxidation steps. The electrochemical polymerization is preferred by researchers because it provides cleaner material and a better control of the morphological parameters, such as thickness and roughness [33]. On the other hand, the chemical polymerization does not require a sophisticated setup to be implemented. The vapor-phase synthesis (VP) is a type of chemical polymerization that is proposed as an alternative to electrochemical polymerization when patterning and thin films (thinner than 100 nm) are required [34].

The goal of this section is to present the basic concepts, methods and techniques for the preparation of PPy films. It starts with the polymerization and doping. The next step is to introduce the electrochemical polymerization technique by describing the setup characteristics. The last section deals with the chemical polymerization, where a short overview of the vapor-phase technique is offered.

1.1.1 Polymerization mechanism

Pyrrole (Py) is an organic compound formed by four carbon atoms, five hydrogen atoms and one nitrogen atom (C_4H_5N) in a ring shape. The structure of Py is shown in Fig. 1.1.

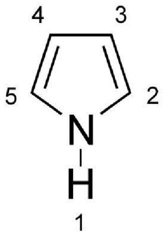

Figure 1.1: *Py monomer representation. The corners 3 and 4 are the β positions while the corners are 2 and 5 the α positions.*

Regardless of the method applied to polymerize, the starting point of the polymerization is basically the dimerization. In spite of the simplicity at beginning, the complete understanding of the synthesis mechanism of PPy, as well of the others conductive polymers, is still under discussion [33].

Among the main polymerization schemes proposed in the literature [10, 35, 36, 37, 38], the one most often used is the Diaz's mechanism [39, 40]. In this mechanism, first the monomers are oxidized forming the radical cations, as shown in Fig. 1.2, by transferring one electron from each monomer ring participating in the reaction to either electrode or oxidizing agent solution, depending on the process used.

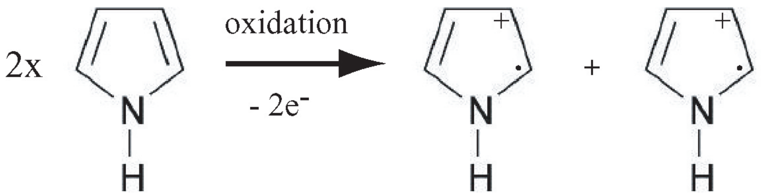

Figure 1.2: *Step 1 - Oxidation.*

In the next step, two radical cations dimerize by forming a bond between their α-position (corners 2 and 5 at Fig. 1.1). The product of the dimerization is called *dihydromer di-cation* (see Fig. 1.3).

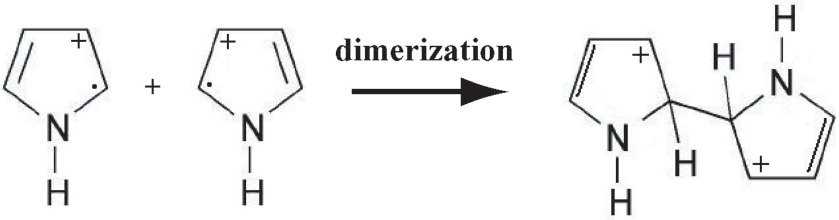

Figure 1.3: *Step 2 - Dimerization.*

The third step is the deprotonation where two protons are released from the dihydromer di-cation to form a dimer (Fig. 1.4).

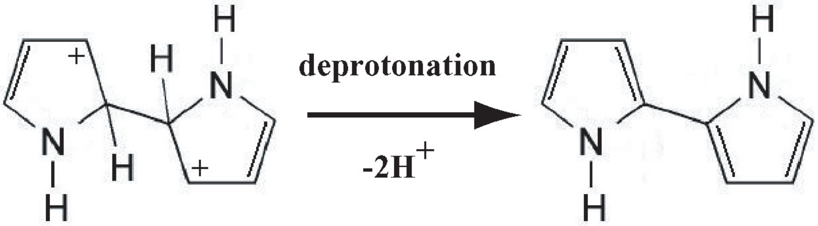

Figure 1.4: *Step 3 - Deprotonation.*

The dimer is then oxidized and once the unpaired electrons are now delocalized over two rings, the oxidation potential of a dimer is lower than the oxidation potential of a single monomer and, consequently, less reactive. In the following reaction step, accordingly to Diaz [39, 40], the dimer radical cation reacts with a monomer radical cation forming a trimer di-cation, which after deprotonation, gives rise to a neutral trimer. Therefore, the polymerization occurs in steps (dimer $\rightarrow$ trimer $\rightarrow \cdots \rightarrow$ oligomer $\rightarrow \cdots \rightarrow$ polymer), following the sequence *oxidation*, *coupling* and *deprotonation* for each step. Furthermore, α-bonds are predominant while the number of bonds at β-position (corners 3 and 4 at Fig. 1.1) tends to increase with increasing chain length. In addition, X-ray photo-electron spectroscopy (XPS) experiments have shown that β-couplings are associated with structural disorder, resulting a PPy film with poor crystallinity [41, 42, 43]. By using methyl groups, it is possible to block the β-couplings, ensuring exclusive bonds at α-position. This procedure increases the crystallinity of the PPy by increasing the order along the chain [44].

However, in the last 10 years, the analysis of the mechanism of electrochemical polymerization indicates that the synthesis mechanism of conjugated polymers does not involve a chain propagation process, with successive coupling steps of the starting radical cation, as proposed by

Diaz's [45, 46]. The oligomerization preferably occurs by consecutive dimerization steps leading from a dimer to a tetramer and then to an octamer (see Fig. 1.5) [45, 46, 47, 48, 49, 50, 51, 52]. Additionally, in all cases where the reaction rates between different reactive oligomers and the starting monomer are similar, trimers and pentamers may be formed within the initial period of oligomerization as well. The reactivities of the generated oligomeric intermediates depend on their respective charging level. Consequently, the applied formation potential steers the chain length of the resulting product. Thus, low oxidation potentials produce short chain lengths due to the fact that the oxidation level of the intermediates is low and, consequently, their reactivities decrease. The same effect is induced by lowering the temperature, which lowers the rate constants of the second-order coupling reactions [53].

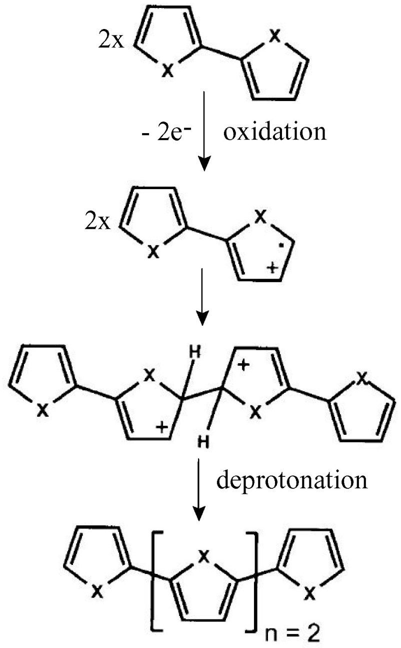

Figure 1.5: *Polymerization by dimerization steps.*

1.1.2 Doping process

Synthesis and doping of PPy occurs simultaneously [54]. During the oligomerization, to maintain the charge neutrality, counterions diffuse into the PPy film from the reaction medium used to polymerize. Consequently, the final polymer composition is a solid-state PPy film, containing counterions (e.g., Cl^- or PF_6^-) positioned between the chains.

In order to reach the charge neutrality due to the presence of counterions, positive charges (holes) are transferred from the substrate into the PPy film, resulting in a final charge concentrations between 0.25 and 0.33 holes per ring [55, 56]. This charge concentration range has been supported by several experimental works [17, 32, 42, 54, 57, 58] by analyzing both chemically and electrochemically synthesized films with different types of dopants. The PPy film as-grown is in the charged state. The "doping" in polymers as described above, is very different from conventional semiconductor doping, where the dopants are generally embedded into the lattice and donate charge carriers to the semiconductor.

1.1.3 Electrochemical polymerization

The electrochemical polymerization deals with processes that involves charge transfer between two characteristic chemical phases, one electronically conducting (the electrodes) and the other ionically conducting (the electrolyte). The polymerization occurs at the interface electrode/electrolyte in an electrochemical cell. The electrochemical cell is a system composed of electrodes and electrolyte. The two-electrode cell is formed by a working electrode (WE), where the polymerization takes place, by a reference electrode (RE) and by the electrolyte. Fig. 1.6 (a) shows a sketch of the electrical diagram of the cell described.

The most common reference electrodes are the *silver-silver chloride electrode* (Ag/AgCl) and the *saturated calomel electrode* (SCE), whose potentials are 0.197 V and 0.242 V against the NHE potential, respectively [59]. NHE is the *normal hydrogen electrode*, an international primary reference electrode. For an ideal RE, the reference potential does not change upon passage of current.

The electrolyte is based on a solution of conductive salt in an either organic or inorganic solvent. Furthermore, in the case of PPy synthesis, the Py monomers are additionally mixed to the synthesis electrolyte.

The potential applied by the power supply against a reference electrode ($\mathrm{V_{appl}\,(vs.\,RE)}$) is determined for a two-electrode cell by

$$\mathrm{V_{appl}\,(vs.\,RE)} = \mathrm{V_{WE}\,(vs.\,RE)} - \mathrm{IR_{el}} \tag{1.1.1}$$

where $\mathrm{V_{WE}\,(vs.\,RE)}$ is the potential of the WE against the potential of

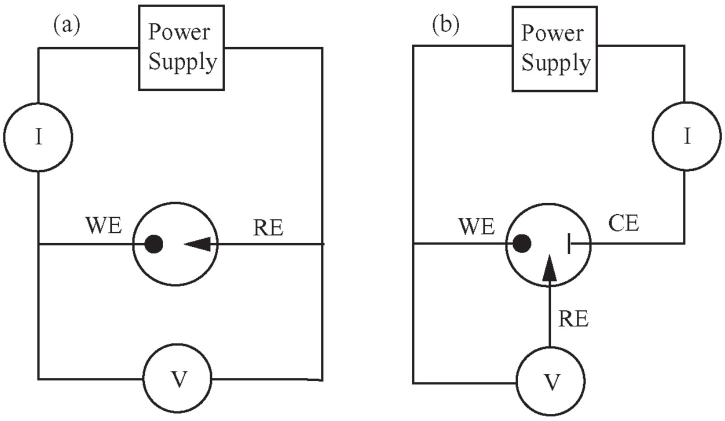

Figure 1.6: *(a) Electrical connection to a two-electrode cell.(b) Electrical connection to a three-electrode cell. WE the working electrode, RE the reference electrode and CE the counter electrode. Adapted from [59].*

the RE, and IR_{el} is the voltage drop upon the electrolyte. The current-voltage characteristics for a two-electrode cell combines the reaction of interest, that occurs at the WE, and the effects in the bulk electrolyte. For this reason, the two-electrode cell is only used in situations where $IR_{\mathrm{el}} \ll V_{\mathrm{WE}}\,(\mathrm{vs.\,RE})$. Consequently, $V_{\mathrm{appl}}\,(\mathrm{vs.\,RE})$ is assumed to be equal to $V_{\mathrm{WE}}\,(\mathrm{vs.\,RE})$. However, in experiments involving organic solvents at lower polymerization temperatures, $IR_{\mathrm{el}} \gg V_{\mathrm{WE}}\,(\mathrm{vs.\,RE})$ is expected, which makes a three-electrode cell necessary.

Fig. 1.6 (b) shows a three-electrode cell diagram. In such a configuration, the current is passed between the WE and a counter electrode (CE). Since the current through the RE is considered negligible, the effects from the bulk electrolyte are almost excluded when the RE is close enough to the WE.

By changing the WE potential, it is possible to control the electron transfer process. As the WE potential is driven towards more negative values, the electron energy increases and electrons are transferred to the vacant electronic states in the electrolyte. The electron transfer process from *electrode to electrolyte* is called *reduction*. The reverse process, namely the electron transfer from *electrolyte to electrode*, is called *oxidation* and is achieved by driving the WE potential to sufficiently positive values.

As described in section 1.1.1, PPy synthesis starts by removing one electron from the Py monomer (*oxidation*), in order to form a dimer (Figs. 1.2 to 1.4). Since the Py monomers are part of the electrolyte, the polymerization consists of transferring electrons from the electrolyte to the electrode by driving the WE potential to more positive values.

The solvent must be chosen carefully since it should be stable at the oxidation potential of Py. Since Py has a low oxidation potential, aqueous electrolytes can be used for polymerization as well. Organic solvents with a high dielectric constant, like acetonitrile (ACN) or propylene carbonate (PC), have the advantage of allowing the synthesis at high growth potentials [59] and low temperatures, in the best cases, down to -43.8^{o}C and -49.2^{o}C, respectively.

The electrodes are also chosen in accordance with the oxidation potential of Py and with the necessity of maximizing the charge (holes) injection into the PPy films, for which the band-gap energy is reported to be in the range $3.0\,\mathrm{eV} - 3.2\,\mathrm{eV}$ [60]. Platinum (Pt), gold (Au) and indium-tin oxide (ITO) coated glass, all having high work functions ($5.8\,\mathrm{eV}$, $5.1\,\mathrm{eV}$ [61] and $4.3\,\mathrm{eV} - 5.1\,\mathrm{eV}$ [62, 63], respectively) are the most common materials for WE and CE.

PPy can be synthesized electrochemically by the followings techniques: galvanostatic (constant current) [64], potentiostatic (constant potential) [65], or potentiodynamic (changing the potential in steps and measuring the current) [66]. In the galvanostatic polymerization, a constant current is applied between the WE and CE, while the potential is measured between WE and RE. For the potentiostatic polymerization, the potential is applied between the WE and CE but it is adjusted to keep the difference of potential across the WE and RE constant. In this case, the current flowing across the WE and CE is measured.

Electrochemical polymerization is limited to synthesis on metallic substrates. Consequently, this method is not particularly well suited for applications that require a multi-terminal geometry. In fact, to characterize electrochemically grown PPy films electrically, it is necessary either to grow a sufficiently large thickness of at least $50\,\mu$m, which allows their mechanical transfer from the polymerization electrode onto a suitable electrode geometry [67], or to synthesize them on electrically isolated electrodes which get bridged by lateral PPy growth [68].

1.1.4 Chemical polymerization

The chemical polymerization is the simplest method used to synthesize PPy. It occurs by mixing the Py monomers with an oxidizing agent. The widely employed oxidizing agents are Fe_3Cl_2 (Fe(III)) [69, 70], H_2O_2 : HCl [71, 72, 73], H_2SO_4 [74], and $CuCl_2$ [75]. This method has been employed in the fabrication of antistatic materials, the coating of insulator substrates and the impregnation of nylon clothes by using Fe(III) as oxidizing agent[76].

Despite its simplicity, this traditional method is limited by the difficulty to prepare thin films. Nevertheless, by changing the manner of exposing the Py monomers to oxidizing agents, it is possible to improve the method.

In 1986, Mohammadi and coauthors [27] proposed the so called vapor-phase polymerization, where a substrate (either insulator or conductor) is first coated by the oxidizing agent and then exposed to Py vapor, evaporated from a liquid-phase source at certain temperature. By changing concentration and type of oxidizing agent, as well as the Py evaporation temperature, both the conductivity and the roughness can be optimized [77, 78, 79].

Fe(III) is the main oxidizing agent used to prepare PPy films [11]. However, when the application requires smooth films, the synthesis procedure becomes complex, since the amount of chlorine ions inside the film must be reduced by rinsing and baking, in order to avoid the salt crystallization [78]. The conductivity measured from the Fe(III) oxidizing films was found to be strongly dependent on the thickness between 200 nm and 500 nm. For films ranging from 20 nm to 100 nm and above 600 nm the conductivity is reported to be independent of the thickness [77].

Patterning of the PPy films was achieved by exposing a thin Fe(III) layer to UV-light, through a lithographic mask, so that Fe(II) is formed in the irradiated regions [28]. Since Fe(II) does not oxidize Py, just the not irradiated region, covered by Fe(III) is able to polymerize the PPy pattern (see the illustration in Fig. 1.7 (a) to (c)). This procedure of patterning suffers from residues of both Fe(II) and Fe(III) into the PPy film [80]. On SiO_2, they adhere very well, becoming an inconvenience once a good electrical isolation between two independent devices on the same substrate is required. Furthermore, Fe is one of the most common metallic contaminants in silicon technology [81, 82, 83], what makes the synthesis of PPy by using Fe(III) incompatible with the silicon processing technology. The same analysis is valid to $CuCl_2$.

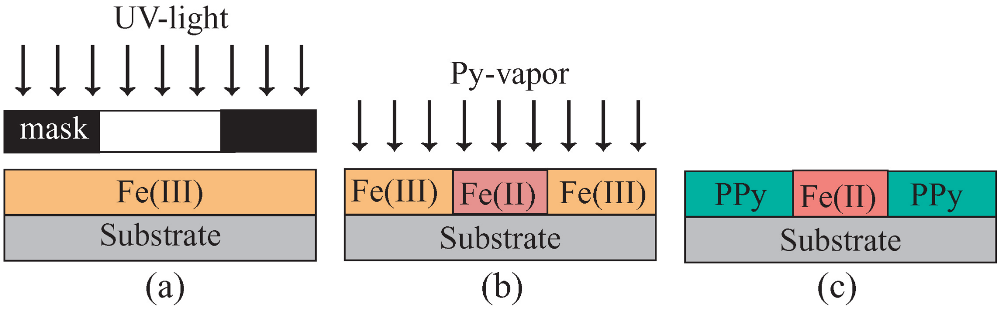

Figure 1.7: *Patterning of a PPy film by using the Fe(III) oxidation. (a) A thin Fe(III) layer is deposited onto a substrate and exposed to UV-light, through a lithographic mask. In this process Fe(III) is transformed in Fe(II) when irradiated by UV-light. (b) Next the film is exposed to Py-vapor. (c) The Fe(III) region on the film oxidizes Py forming PPy while the Fe(II) region remains unchanged.*

1.2 Electrochemical characterization

The electrochemical characterization includes the determination of the the redox potential of a molecule, atom or ion. The redox potential is a measure of the energy at which the reduction or oxidation occurs. Therefore, this redox energy can be regarded as a fingerprint of the polymer.

The aim of this section is to introduce the basic concepts of cyclic voltammetry (CV), which is the most used technique to measure the redox potentials of conducting polymers.

1.2.1 Cyclic voltammetry

A large part of understanding of the redox processes and the charge-transfer kinetics in several kinds of materials comes from the CV [84, 85].

CV consists of scanning the potential at the WE, with a constant rate, and measure the current resulting from this potential. The three-electrode electrochemical cell (Fig. 1.6(b)) is also applied to CV, but the electrolyte used is monomer free (only solvent and conductive salt). During the cyclic voltammetry, the potential is applied between the WE and the CE. The values measured are $\mathrm{V_{WE}}$ (vs. RE), that is related to the reaction, and the current between the WE and the CE. This current depends basically on the chemical reactivity of the electroactive species and the ratio of the reaction rate to the potential scan rate. The plot of current vs. $\mathrm{V_{WE}}$ (vs. RE) is called a *cyclic voltammograms*.

By scanning the potential of the WE from positive to more negative values, the material probed (that is either diluted in the electrolyte or deposited upon the electrode) is *reduced*. Accordingly, by driving the potential from negative to more positive values, the system is *oxidized*. Fig. 1.8 shows a cyclic voltammogram of hexachloroiridate(IV) performed in a water/potassium nitrate electrolyte [86].

Hexachloroiridate(IV) is a didactic system used to study the reversible redox reaction. By scanning the potential in a negative direction (from 1.1 V to 0.3 V), the system is reduced at $\sim 0.68\,\mathrm{V}$ from hexachloroiridate(IV) to hexachloroiridate(III). This half cycle is called *anodic wave*, since the electron is transferred from the electrode to the electrolyte. The reduction point is represented by the peak with anodic

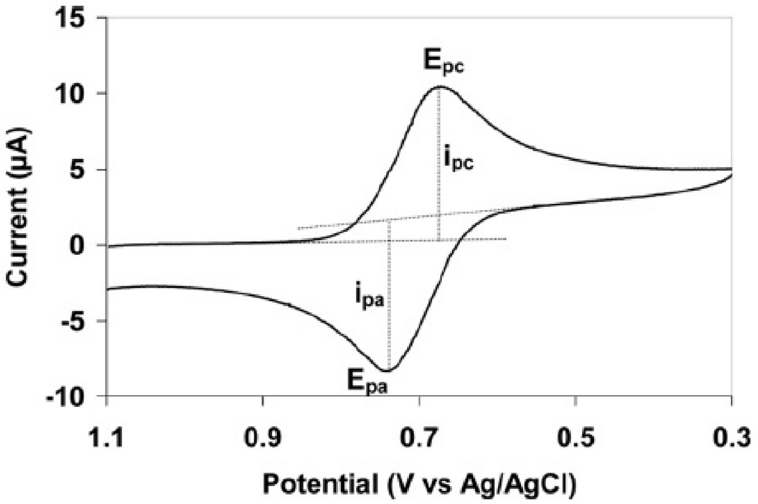

Figure 1.8: *Cyclic voltammogram of hexachloroiridate(IV) performed in a water/potassium nitrate electrolyte. Adapted from [86].*

potential E_{pa} and anodic current i_{pa}. Afterwards, sweeping the potential from 0.3 V to 1.1 V the reoxidation occurs at ~ 0.73V, corresponding to a transition from hexachloroiridate(III) to hexachloroiridate(IV). Once the system has released an electron from electrolyte to electrode, the second half cycle is called a *cathodic wave*. The oxidation peak is represented by the cathodic potential E_{pc} and cathodic current i_{pc} [86]. Summarizing, the set of values [E_{pc}, i_{pc}] and [E_{pa}, i_{pa}] measured are the characteristic redox potentials of Hexachloroiridate(IV).

1.2.2 Polypyrrole film characterization

Recent measurements [87] show that PPy films typically contain PPy I and PPy II, two variants of PPy that can be clearly distinguished phenomenologically, for example, in CV (see Fig. 1.9). The PPy film evaluated was prepared by galvanostatic polymerization at 100nA in a solution of 0.1M Py, 0.1M $TBAPF_6$, 1 wt% of H_2O and 1% of 10^{-5}M HCl in ACN, at 20 °C. The amount the HCl and H_2O added increases the acidity of the electrolyte and guarantees the formation of PPy II. The CV was performed in a monomer-free solution of 0.1M $TBAPF_6$ in ACN at $-20\,^\circ$ C, by using a scan rate of 100 mVs^{-1}. It is also known that as the growth temperature decreases or low formation potentials are applied, more PPy II is formed. Until recently, however, it has not been clarified which quantitative structural differences exist between

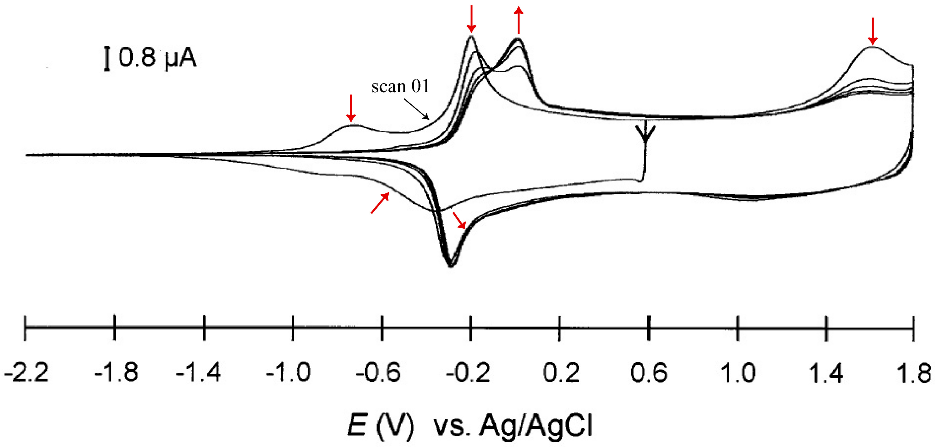

Figure 1.9: *Electrochemical solid-state transition of PPy II to PPy I promoted by increasing the potential during the CV. After 12 scans in the range of 0.60V to -2.2V, the scan range was extended to 1.8V to -2.2V. The red arrows indicate how the traces evolve over cycling. Adapted from [87].*

PPy I and PPy II [87].

To characterize and change the charge concentration of the polymer, CV in an electrolyte solution free of monomers is an established and powerful method [9, 88]. The polymer chains are discharged during the reduction step (from 0.60 V to −2.2 V in the CV at Fig. 1.9), a process which is compensated by anions (PF_6^-) that drift out of the film and/or by the insertion of cations (TBA^+) into the film, respectively [87]. The reverse processes occur during oxidation [89, 90, 91] which is sometimes referred to as p-doping of the polymer.

The current-voltage curves for PF_6^--doped PPy, performed during CV, exhibit a reduction wave at −0.28 V (vs. Ag/AgCl) and an oxidation wave at 0 V for a PPy I and −0.23 V for PPy II [87].

It is well-known that CV induces a variety of further processes and effects. The formation of σ-bonds between chains during oxidation and their breakage during subsequent reduction steps have been discussed [89, 90]. Furthermore, in situ conductivity measurements during CV show a characteristic hysteresis loop, indicating structural changes [92], in particular flattening of twisted chains as well as σ-bond formation [87, 93] and intermolecular π-interaction [94, 95, 96]. Moreover, the volume and the mass of the films change as a function of the potential and the history of the film; finally, the cycling partly transforms PPy II into PPy I [87, 97], as represented in Fig. 1.9.

CV has also been used to characterize chemically prepared PPy films [72, 78]. Fig. 1.10 shows the CV of PPy synthesized in solution containing 1.5 ml of Py, 50 ml of 30% H_2O_2 and 1-2 drops of concentrated HCl, deposited onto a Pt electrode [72]. The CV was performed in an electrolyte containing 0.1M of the conductive salt $LiClO_4$ in water. The peroxide PPy film shows an oxidation peak at 0.2 V vs. SCE and a reduction peak at −0.35 V vs. SCE, what is equivalent to 0.25 V vs. Ag/AgCl and −0.30 V vs. Ag/AgCl, respectively.

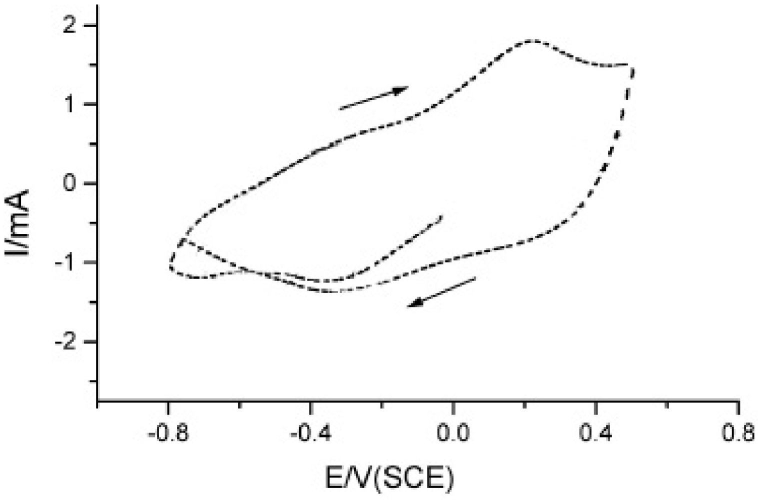

Figure 1.10: *CV for a PPy sample synthesized in solution of* $H_2O_2 : HCl$ *and deposited onto a Pt electrode. Adapted from [72].*

1.3 Electronic characterization

1.3.1 Electronic transport in conducting polymers

The electronic transport in conducting polymers is usually determined by the thermally assisted hop of charges between localization centers. These localization centers are potential wells created by the disorder level of the polymer. Taken into account the three dimensional (3D) variable range hopping (VRH) model proposed by Mott [98], the density of states near the Fermi level is assumed to be non-zero, and the hopping sites are randomly distributed in energy and position into a band (with extension M) around the Fermi level $\mathrm{E_F}$ (see Fig. 1.11 (a)).

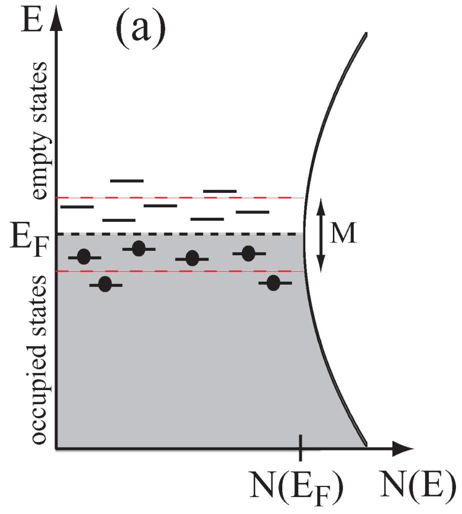

Figure 1.11: *Schematic illustration of the localized states. (a) In the 3D VRH the charges are localized inside a band of extension M, where the density of states around the Fermi level is assumed constant. The gray region represents the occupied localized states. (b) Zoom-in in the region of constant* $N(E)$*.*

The transport occurs when localized charges tunnel inelastically or elastically ("hop") from an occupied state to an empty one, as illustrated in Fig. 1.11 (b). The conductivity in such a system depends on the probability of hopping from one state to another which is given by

$$P = \nu_{ph} \exp\left(-\frac{\Delta E_h}{k_b T} - \frac{2r_h}{L_c}\right) \tag{1.3.2}$$

where ν_{ph} is the characteristic frequency of the phonon, $\Delta \mathrm{E_h}$ is the difference of energy between the two states, $\mathrm{r_h}$ the hopping distance and

L_c is a characteristic radius that determines the decay rate of the wave function $\psi(r_h) \propto \exp(-r_h/L_c)$ [98]. L_c is also called the *localization length.* Therefore, two localized states interact by the overlap of their wave functions, and the conductivity is proportional to the hopping probability. The temperature dependence of the conductivity, for the 3D VRH, is expressed by

$$\sigma(T) \propto \exp\left[-\left(\frac{T_0}{T}\right)^{1/4}\right] \tag{1.3.3}$$

with

$$T_0 = \frac{16}{k_B N(E_F) {L_c}^3} \tag{1.3.4}$$

where $N(E_F)$ is the density of states at the Fermi level and k_B the Boltzmann constant.

In the case where conductivity depends on the Coulomb interactions of the localized charges, the density of states is zero at the Fermi level ($N_{ES}(E_F) = 0$) and $N(E) \propto {E_{ES}}^2$ for a 3D system, where E_{ES} is the charge energy of the localized state. Fig. 1.12 shows a schematic illustration of the energy dependence of the density of states in the VRH including the Coulomb interaction of the localized charges. ΔE_{ES} is the Coulomb gap.

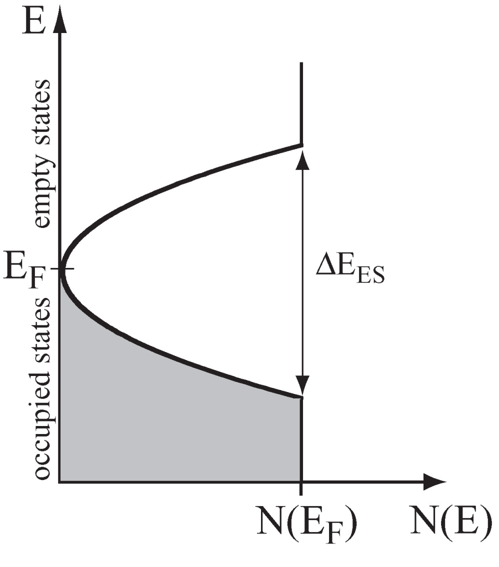

Figure 1.12: *Schematic illustration of the Coulomb gap near to the Fermi level.* ΔE_{ES} *is the Coulomb gap.*

This VRH conductivity between charges in the presence of Coulomb interactions is called *Efros-Shklovskii VRH* (ES-VRH) [99, 100]. In the ES-VRH, σ(T) decreases with decreasing the temperature following the dependence,

$$\sigma \propto \exp\left[-\left(\frac{T_0}{T}\right)^{1/2}\right] \tag{1.3.5}$$

where

$$T_0 = \frac{2.8e^2}{4\pi\varepsilon_0\varepsilon_r k_B\xi} \tag{1.3.6}$$

ξ is the localization length in the ES-VRH, ε_0 the vacuum dielectric constant and ε_r the relative dielectric constant of polymer. The gap in the ES-VRH vanishes for temperatures above a critical temperature $\mathrm{T_c}$ (soft gap), where the 3D VRH is expected [100, 101]. Nevertheless, in systems where the Coulomb gap exists for all temperatures (hard gap), N(E) is zero also in the vicinity of the $\mathrm{E_F}$. By considering a localization center with a radius $\mathrm{r_c}$, the Coulomb blockade energy $\mathrm{E_c}$ is given by [102, 103, 104]

$$E_c = \frac{e^2}{4\pi\epsilon_0\epsilon_r r_c}. \tag{1.3.7}$$

$\mathrm{E_c}$ is the energy necessary to transfer one electron from an occupied state to an empty one. In the Coulomb blockade regime, the conductivity is dependent of the charge transfer between two states and it is described by [105]

$$\sigma_c(T) = \sigma_0 \exp\left(-\frac{E_c}{2k_BT}\right). \tag{1.3.8}$$

The Coulomb blockade effect is widely observed in metallic granular systems [106]. Normally such a system is formed by an array of metallic particles separated by some kind of insulator, that creates a barrier for the charges [106]. When the barrier is ideal, $\mathrm{N(E_F)} = 0$ for all temperatures, and the conductivity of the system is expected to follow eq. 1.3.8. But when the insulator contains some degree of doping and the localization centers are randomly spread, a non-zero density of states at the vicinity of the Fermi level can exist [105]. Consequently, the Coulomb interaction between localized sites gives rise to a soft

Coulomb gap in the background of the finite density of states near to the Fermi level [105]. At low enough temperatures this effect generates an ES-VRH like dependence where $\sigma(\mathrm{T})$ is expressed by eq. 1.3.5. But in the context of electronic transport through a granular system, the coefficient T_0 at eq. 1.3.6 has a different meaning [105, 107]. In the ES-VRH, ξ is the localization length for tunneling across a much longer distance than the radius of a grain $\mathrm{r_g}$ [99]. By considering that the tunneling between two separated grains occurs through the insulator with thickness $\mathrm{d_g}$, the localization length for a granular system is given by $\xi_\mathrm{g} = \mathrm{a_t r_g/d_g}$, where a_t is the tunneling decay length in the insulator [105, 108]. Taking into account these considerations, the coefficient T_0 for a granular system with a soft gap can be rewritten as [105]

$$T_0 = \frac{2.8e^2 d_g}{4\pi\varepsilon_0\varepsilon_r k_B\, ar_g} \tag{1.3.9}$$

The conductivity of PPy is reported to be strongly dependent of the method adopted to polymerize - chemically [32] or electrochemically [67] - as well as the control parameters of polymerization (e.g., the synthesis temperature [14], the type [15] and concentration [109] of counterions , polymerization potential/current density [29], solvent [110], etc.). Mechanical stretching and film thickness are also presented as parameters to change the conductivity in PPy films [77, 111, 112]. Films electrochemically synthesized at low temperatures (e.g. -40°C) have conductivities around $\sim 500\,\mathrm{S/cm}$ at room temperature, a value which can be increased up to $\sim 1500\,\mathrm{S/cm}$ when the film is stretched [13, 14, 15].

In the insulating regime of PPy, it is assumed that charge transport takes place via 3D VRH [98]. Another characteristic property of this phase a positive magnetoresistivity, where $\rho(\mathrm{B}) \propto \mathrm{B}^2$ for lower magnetic fields and $\rho(\mathrm{B}) \propto \sqrt{\mathrm{B}}$ for higher fields [109, 113, 114].

In the metallic regime, on the other hand, various models suggest a power law [67, 113, 114] or an exponential dependence [115] of the resistivity on the temperature. Here, a *metallic regime* is usually defined as a regime where the resistivity extrapolated to $\mathrm{T} = 0$ remains finite, while for a *true metal* the resistivity decreases with decreasing temperature.

According to the scaling theory, the metallic conductivity is modeled by a power law dependence

$$\sigma = \sigma + \alpha\sqrt{T} + \beta T^{p/2} \qquad (1.3.10)$$

where the second term on the right-hand side originates from electron-electron interactions [114], while the third term takes localization effects into account [115, 116, 117]. The model presented by McMillan [118] shows that once the electron wave packets, with a length scale $\mathrm{L_m}$, assume the same value of the correlation length ξ_m (value in which the system crosses over from critical to metallic or insulating regime), $\sigma(0)$ is given by

$$\sigma(0) \approx 0.1\frac{e^2}{\hbar}\frac{1}{L_m} \qquad (1.3.11)$$

where $\mathrm{L_m}$ localization length in the metallic regime.

The reflectivity of metallic PPy films has been studied over a wide range of frequencies [119, 120, 121]. These measurements strongly suggest that in the metallic regime, only a small fraction (a few percent at most) of the charge carriers participate in the conduction mechanism, while the majority of the charges is strongly localized.

Recently published results have shown that *true metallic* behavior is possible in conducting polymers [122]. The measurements were performed in polyaniline (PANI) samples, processed by two different methods: the conventional one that uses an aqueous medium containing aniline, and the self-stabilized dispersion method (SSDP). SSDP uses a biphasic (organic and aqueous) mixture to polymerize. Samples with different conductivities were prepared by this method. Fig. 1.13 (a) shows the temperature dependence of the resistivity for PANI samples. Nevertheless, true metallic behavior has not been observed in PPy up to now.

Several studies have reported a metal-insulator transition in PPy, which is driven by varying the doping concentration [13, 109], the counterion type [123], or the polymerization temperature [29, 67, 119]. Fig. 1.13 (b) presents a log-log plot of the temperature dependence of the normalized resistivity for PPy doped with $\mathrm{PF_6}^-$ and polymerized at different temperatures [67]. The sample M1 is in the metallic regime (finite resistivity at T = 0), the samples Mc1 to Mc3 are found on the transition metal-critical regime while the samples Ic1 and Ic2 are in the insulator-critical regime. The samples I1 and I2 are at the insulator side of the transition. Theoretical considerations imply that the

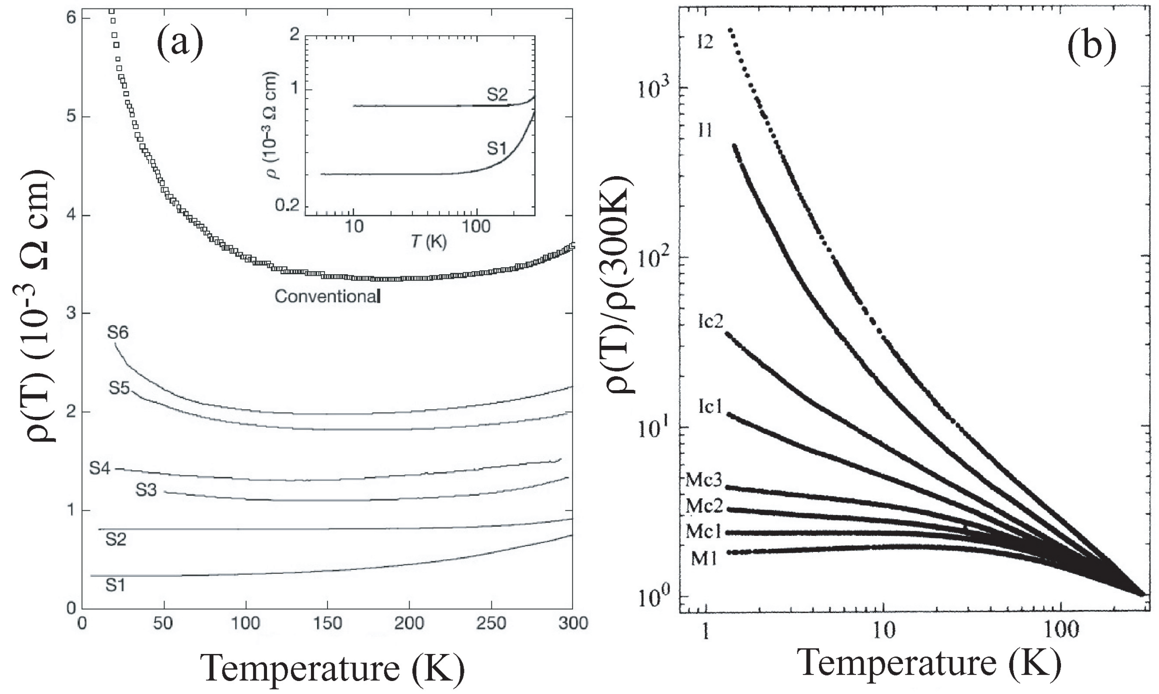

Figure 1.13: *(a) Temperature dependence of resistivity, $\rho(T)$. Data from a conventional PANI film are represented by open squares. This trace is compared with the samples prepared by the SSDP method (S1 to S6). For more highly conducting samples (S5 to S1), the resistivity minimum weakens and shifts to lower temperature and eventually disappears in the S1 and S2 samples (as shown more clearly in the inset). Take from [122]. (b) Log-log plots of the temperature dependence of the normalized resistivity for PPy doped with* PF_6 *and polymerized at different temperatures. Taken from [67].*

two critical parameters for the metal-insulator transition are the interchain coupling strength and the disorder: as the system crosses from the insulating into the metallic phase, one-dimensional (1D) states (localized on a single chain) evolve into 3D states, which are delocalized over several chains with short-range order and form a metal [124, 125].

The electronic properties of PPy films are related to the concentration of interchain links or side chains, as reported by Joo and coworkers [32]. The interchain links and side chains are indicated in Fig. 1.14. By comparing charge transport and structural properties of both electrochemically and chemically synthesized samples, they concluded that the insulator regime, for chemically prepared PPy, is associated with the reduction of interchain links or side chains and the weaker interchain interaction. In addition, the electrochemically polymerized samples are found in the critical and metallic regime. These samples also had a higher concentration of interchain links or side chains.

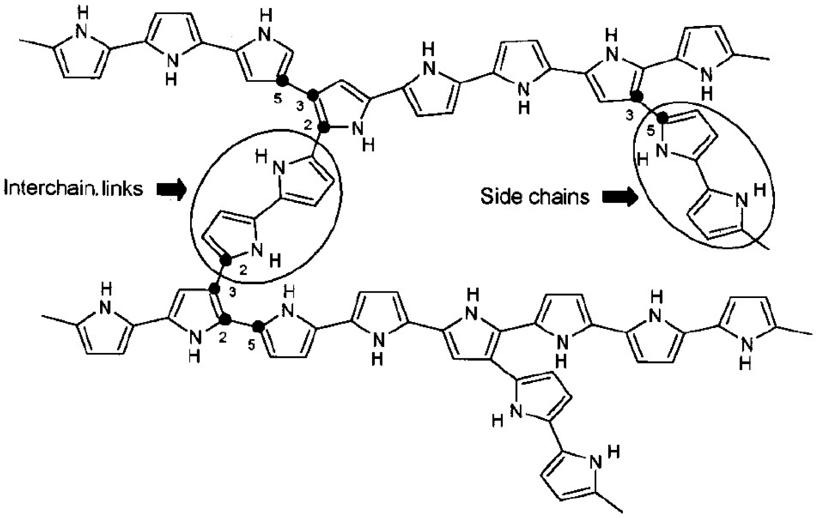

Figure 1.14: *Schematic chemical structure of interchain links or side chains through 2,3 coupling modes of PPy. Taken from [32].*

1.3.2 Electric-field dependence of the conductivity

The electric field dependence of the conductivity was observed in PPy films prepared by anodic deposition [126]. At low temperatures, the p-toluensulfonate doped PPy, shows a nonlinear conductivity when subjected to electric fields around 50 V/cm. Such a system is assumed to be formed by metallic grains separated by tunnel barriers [30, 31], which are generated by variations in the charge density. The inter-grain tunneling model has been considered to give a better description of the system than VRH, but it does not explain the temperature dependence of the conductivity at very low temperatures. In addition, the measurements have shown that the conductivity decreases with decreasing temperature. More recently, the same group [127] reported an electric field induced transition from an insulating state to a highly conductive one, also by using p-toluensulfonate doped PPy samples.

This kind of non-equilibrium transition was also reported in other amorphous materials such as polythiophene [128] and yttrium silicide ($Y_{0.19}Si_{0.81}$) [129]. In the first case, the electric transport was investigated in field-effect transistor structure whose active channel was made by polythiophene (see Fig. 1.15).

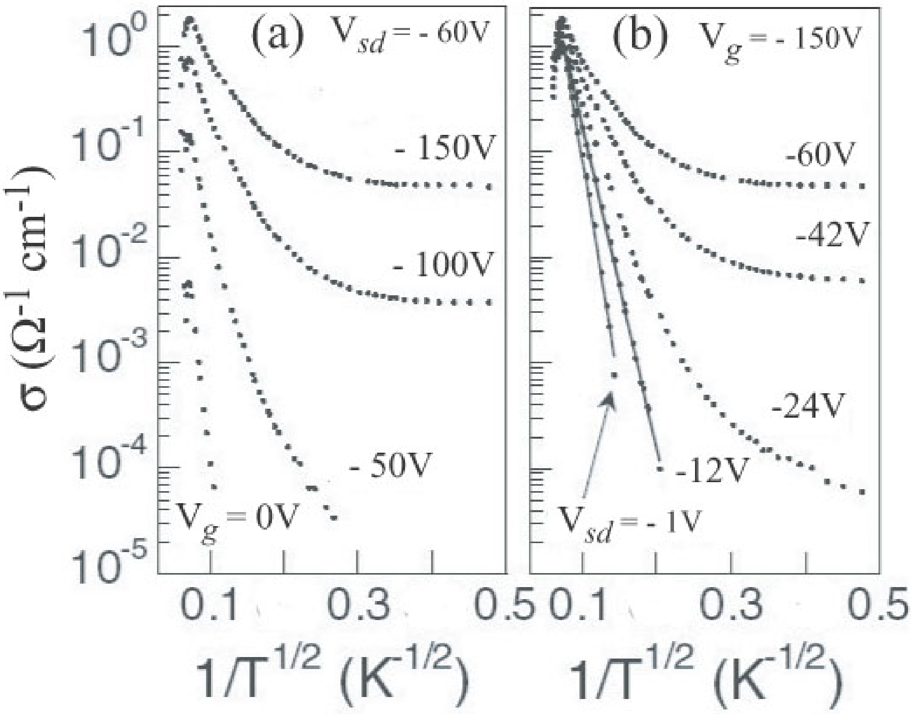

Figure 1.15: *Conductivity vs.* $T^{-1/2}$ *of a polythiophene field effect transistor (FET) (a) at* V_{sd} = *-60V and varying* V_g. *The metallic regime is indicated to be at* V_g = *-60V. (b) At* V_g = *-150V for varying* V_{sd}. *The straight lines are exponential fits to the data. The fit to the* V_{sd} = *-1V data follow the ES-VRH while the* V_{sd} = *-24V data are fitted to a power law. In this plot, the metallic regime is found at* V_{sd} = *-60V. Taken from [128].*

The measurements show that by varying both gate and source-drain voltages it is possible to change the temperature dependence of the conductivity. Such changes are interpreted as a transition from an insulator to metallic regime. The metallic regime is reached once a small fraction ($< 0.01\%$) of the localized charges tunnel through the potential barrier because of the applied the electric-field. In the insulating state, the data is fit by the VRH with Coulomb interactions (ES-VRH).

The second experiment [129] shows that the temperature dependence of the conductivity also can be described by the ES-VRH below 2K and for small electric fields. The activated transport is observed for temperatures higher than 10 K. The measurements show a non-linear current-voltage behavior, what is explained in terms of a percolation path. At low electric fields, the current flows through a very irregular path that constitutes the most resistive case. Such paths are obtained by using isotropic percolation theory [129, 130, 131]. Under a very high electric field, the hops occur anisotropically along the field direction and independent of temperature (directed percolation). In such a regime, the high electric field increases the energy of the charge in order to overcome the energy fluctuation due to the disorder [132, 133].

1.4 Structural characterization

1.4.1 Crystallographic structure

The crystallographic structure of PPy has been determined by using electron diffraction techniques [44]. The PPy films, with thickness from 0.5 μm to 2 μm, were grown electrochemically and discharged to the neutral state by reduction from the as-grown doped state. The β-couplings, which are responsible for the increase of the disorder [41, 43], were blocked during the synthesis by using methyl groups [44, 134]. This procedure is reported to improve the crystallinity of the PPy film, although both types of PPy structures - with and without β-couplings - were found to have poor crystallinity. The crystalline regions are supposed to be randomly oriented in the neutral PPy film and have some preferred orientation in the films, once the β-couplings are blocked. The large amount of structural disorder in PPy films was also verified by ultraviolet photoelectron spectroscopy (UPS) [135] and X-ray photoelectron spectroscopy (XPS) [42].

The PPy chain structure has been assumed to be linear and planar with alternating head orientation, as represented in Fig. 1.16. The values indicated in Fig. 1.16 are in good agreement with first-principles calculations reported by Bredas and coworkers [55].

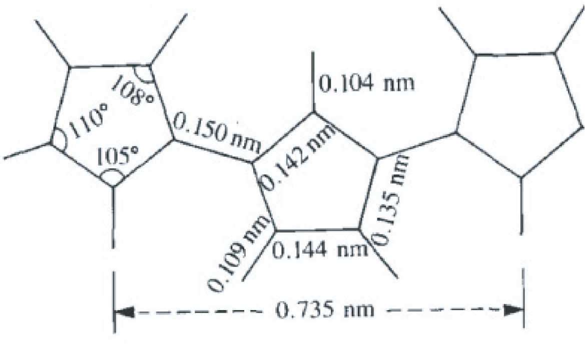

Figure 1.16: *Linear chain structure for neutral PPy. Taken from [44].*

1.4.2 Chain length

The electrochemical and optical properties of PPy are strongly correlated with the chain length [136]. UV-vis absorption spectra have shown that changes in both concentration of charges and structure, due to the processes of oxidation and reduction, clearly influence the optical properties of the polymer [56, 137, 138]. Zotti and coworkers have measured the electronic and electrochemical parameters of well-defined neutral oligopyrroles [136]. From the cyclic voltammetry, the redox potentials of oligopyrroles (chains set from one to seven rings) were determined and associated to the chain length. In addition, the energy of the maximum absorption (E_λ) for each oligomer chain length was extracted from the UV-vis spectra. Fig. 1.17 (a) shows the electronic spectrum of the pentapyrrole (five rings) in three distinct states: the reduced state (P_5), the first oxidation state (${P_5}^+$) and the second oxidation state (${P_5}^{++}$). The oxidation states are indicated in the cyclic voltammogram (see Fig. 1.17 (b)) by the two oxidation peaks, one at -0.28 and another at -0.08V, for ${P_5}^+$ and ${P_5}^{++}$, respectively.

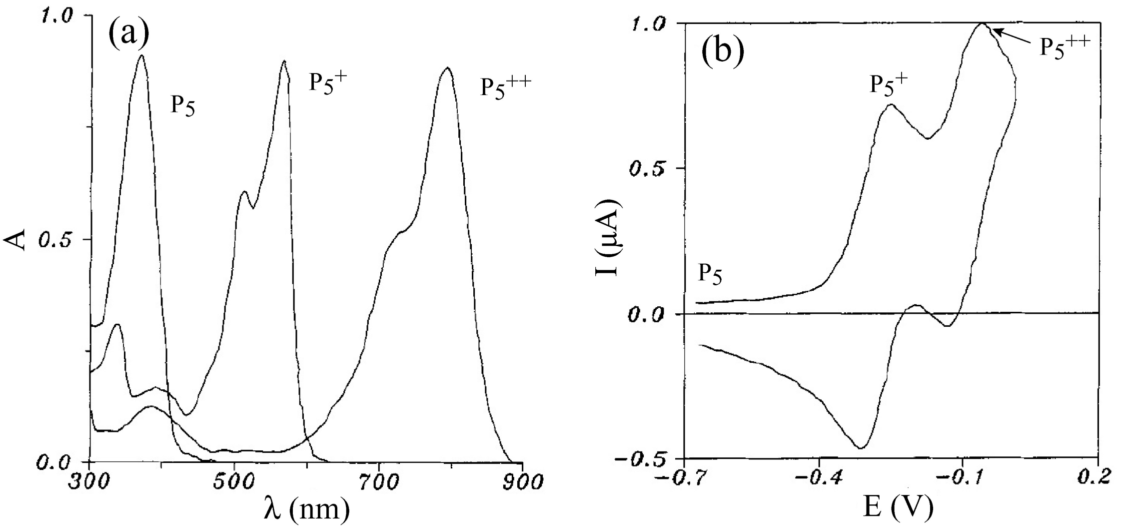

Figure 1.17: *(a) The electronic spectrum of the pentapyrrole in three distinct states: the reduced state (P_5), the first oxidation state (${P_5}^+$) and the second oxidation state (${P_5}^{++}$). (b) Pentapyrrole cyclic voltammogram. The peak at -0.28V corresponds to ${P_5}^+$ state while that one at -0.08V refers to the state ${P_5}^{++}$. Adapted from [136].*

Parameters such as energy of polyconjugated polymers are known to scale linearly with the inverse of the degree of polymerization (number of rings) [139]. According to their results a longer polymer chain has an absorption maximum at a lower energy (longer wavelength) than a shorter polymer chain (Fig. 1.18).

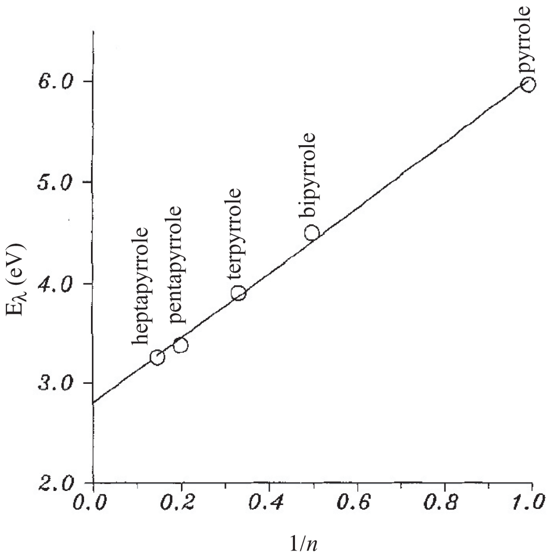

Figure 1.18: *E_λ vs. $1/n$, where n is the number of pyrrole units. Figure adapted from [136].*

1.4.3 Surface morphology

The morphological analysis of the PPy film surfaces has been mostly performed by scanning probe microscopy (SPM) and scanning electron microscopy (SEM). The surface morphology depends on both the growth method and the parameters of polymerization. As an example, Xu and coworkers [140] reported that by adding a tiny amount of Fe in the solution used to electrochemical polymerization the morphology of a PPy film can be changed. Fig. 1.19 shows the SEM images of the surface of PPy films deposited onto a Au-coated glass and prepared without (a) and with (b) Fe.

The addition of Fe in solution is made by the insertion of Fe(III). For this reason both chemical and electrochemical polymerization occurs simultaneously leading to a formation of a more compact film. The image reveled that the porosity of the PPy decreases after the insertion of Fe.

By associating the morphological changes with volume changes, Surez [141] evaluated the effects of the reduction and oxidation processes upon PPy films. For films prepared in aqueous solution of sodium

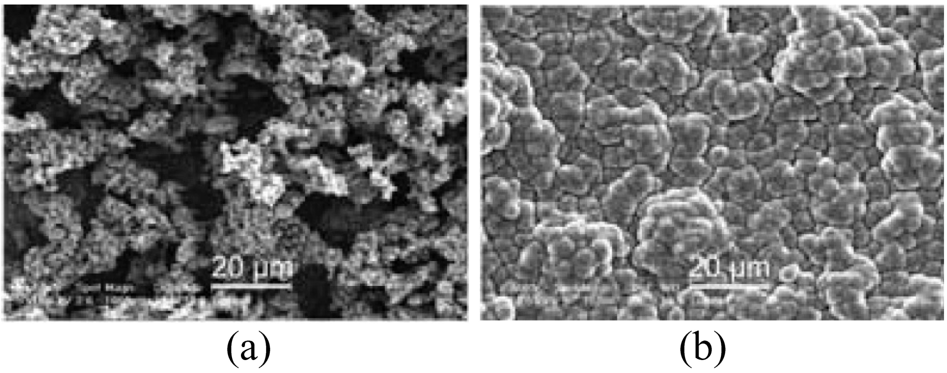

Figure 1.19: (*a) Top view of a PPy film grown with a solution free of Fe.(b) Top view of a PPy film grown with after insertion of a tiny amount of Fe. Figure adapted from [140].*

p-toluenesulfonate, the polymer swells during the reduction and shrinks during the oxidation process. In addition, the roughness of electrochemically grown films is reported to increases by increasing the film thickness.

In general, the surface morphology for PPy thin films (below $\sim 1.0\,\mu$m) have shown typically an egg-like-shaped structure, although the size and shape are slightly depending on the polymerization parameters [33, 64, 141, 142, 143]. The AFM image in Fig. 1.20 (a) shows the surface morphology of a ~ 10 nm thick PPy film, deposited on a gold coated silicon substrate after 2 s of electrochemical polymerization in water [144]. Fig. 1.20 (b) shows the same film after 20 s.

The same group reported [144], by using the current-sensing atomic force microscopy (CS-AFM), that the top of the egg-like structure is more conducting than the valleys. This behavior is related to the fact that the top of the egg-like structure ca be easily oxidized during the formation process [64]. In addition, it was observed that the conductivity can be increased by increasing the film thickness.

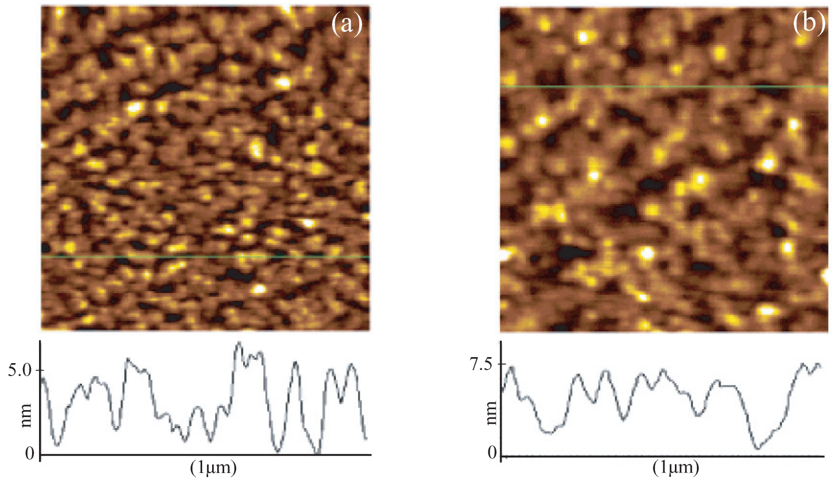

Figure 1.20: *(a) Top view of a ∼10nm thick PPy film, deposited on a gold coated silicon substrate after 2s of electrochemical polymerization in water. (b) Top view of the same film after 20s of polymerization . Adapted from [144].*

1.5 Devices

1.5.1 Polypyrrole sensors

PPy has been widely used as active layers in both gas [18, 19, 20, 21] and biochemical [22, 145] sensors. Van and coworkers have reported the sensitivity of PPy to nitrogen dioxide (NO_2)[146]. This sensitivity depends strongly of the film thickness and of the polymerization temperature. Since PPy is a p-doped polymer, when exposed to NO_2 the doping level increases, because of its acceptor behavior [147], and consequently an increase of the conductivity is observed. Conversely, by exposing PPy to electron donating gases, like ammonia (NH_3), causes a reduction of the carrier density and therefore an increase in resistivity [19]. The sensitivity to gas exposition is also observed to be dependent on the charge state of the polymer. After a reduction process, PPy exhibits a higher sensitivity to some gases (such as PCl_3, SO_2 and NO_2) as compared to the charged state. Experiments with Fourier transform infrared spectroscopy (FTIR) [148] have shown that once exposed to NO_2 in the reduced state, PPy gets doped by the anion NO_2^-, as described in the reaction scheme below:

$$\mathrm{PPy}^* + \mathrm{NO_2} \rightleftarrows \mathrm{PPy}^+ + \mathrm{NO_2^-}(\mathrm{ion}) \qquad (1.5.12)$$

where PPy^* is the reduced state of PPy and PPy^+ the p-doped state.

The sensitivity to H_2O_2 is the key to use PPy in biosensors [22]. Fig. 1.21 presents the variation of the normalized conductivity of a PPy film when exposed to different concentrations of H_2O_2 [149].

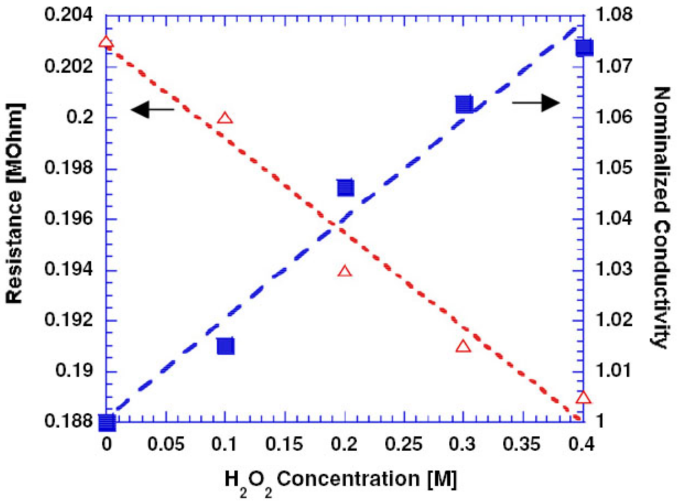

Figure 1.21: *Normalized conductivity of a PPy film when exposed to different concentrations of H_2O_2. Adapted from [149].*

The normalized conductivity increases linearly as the concentration of H_2O_2 increases. In the presence of oxygen, glucose can be oxidized to yield gluconic acid and H_2O_2, as presented in the following scheme [150]:

$$\text{glucose} + O_2 \overset{\text{GO}}{\longrightarrow} \text{gluconic acid} + H_2O_2 \tag{1.5.13}$$

where GO is the glucose oxidase. From the reaction, the concentration of glucose can be determined by measuring the amount of H_2O_2 produced during the reaction. In order to build a sensor, GO is embedded within a PPy matrix [149, 150]. The conductivity changes when glucose reacts with the GO embedded and produces H_2O_2, which oxidizes the PPy matrix. Consequently, the effect of the oxidation is that more holes are injected from electrode to polymer.

In addition, several experiments have shown that PPy in both the reduced [41, 56, 151] and the oxidized [152, 153, 154, 155] form are sensitive to oxygen. Some of then [41, 151], have suggested that the original counterion (such as Cl^- or PF_6^-), which was embedded during the polymerization, is replaced by OH^- after the film reduction and subsequent exposure to oxygen.

1.5.2 Field-effect transistor

Metal-oxide-semiconductor field-effect transistor

In order to analyze the operation of OFETs, this Section describes a n-channel metal-oxide-semiconductor field-effect transistor (n-MOSFET) [61]. The n-MOSFET structure is shown in Fig. 1.22 (a). Fig. 1.22 (b) shows the energy band diagram for the gate/$\mathrm{SiO_2/p-Si}$ structure. For a gate voltage V_g higher than the threshold voltage V_t, an inversion layer is formed in the interface $\mathrm{SiO_2/p-Si}$ by depleting holes and accumulating electrons from the n^+ doped-Si (the green region in Fig. 1.22(a)). V_t is the voltage necessary to open the n-channel. Once the n-channel is opened by V_g, the current I_d flows due to the drain voltage V_d. This is the *linear regime* of operation as indicated in the current-voltage characteristics of a n-MOSFET (see Fig. 1.23(a)).

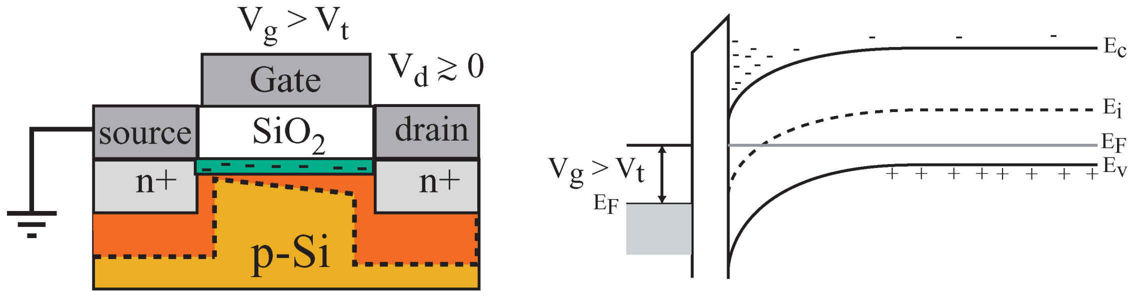

(a) (b)

Figure 1.22: *(a) n-MOSFET positively biased. (b) For* $V_g > V_t$ *an inversion layer (in green) is formed in the interface* $SiO_2/p-Si$ *by depleting positive charges and accumulating those from the* n^+ *doped-Si. The red region is the depletion layer.* V_t *is the threshold voltage,* E_F *the Fermi level,* E_c *is the conduction band,* E_v *the valence band and* E_i *the intrinsic Fermi level.*

By increasing V_d, the n-channel length near to the drain contact tends to zero (see Fig. 1.23(b)). This point is called *pinch-off point* and it occurs when $V_d = V_{sat}$, where V_{sat} is saturation voltage, that determines in which V_d the transistor operates in the *saturation regime* (see Fig. 1.23 (a)). The red arrow in Fig. 1.23 (a) indicates the direction in which V_g increases. From the current-voltage characteristics of the n-MOSFET, its possible to verify that I_d increases by increasing both V_d and V_g.

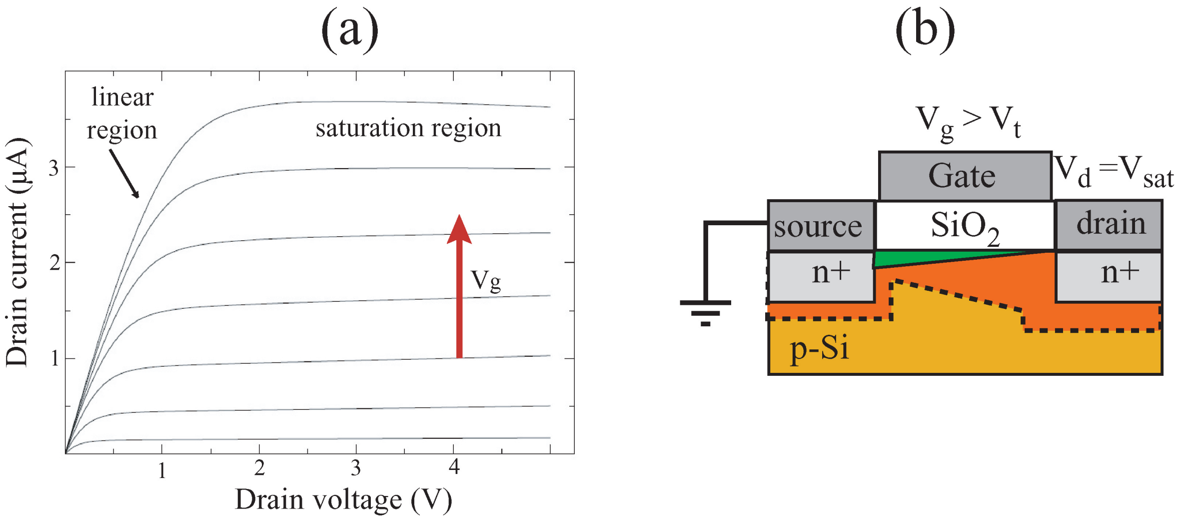

Figure 1.23: *(a) Current-voltage characteristics of a n-MOSFET. The red arrow indicates the direction that* V_g *increases. (b) n-MOSFET positively biased For* $V_d = V_{sat}$*, the n-channel length near to the drain contact tends to zero.* V_{sat} *is saturation voltage, that determines in which* V_d *the transistor operates in the saturation regime.*

Thin-film-transistor

The Thin-film-transistor (TFT) is currently used in amorphous silicon transistors [156] since its structure is very well suited for materials with high resistivities [157]. Therefore, the operation description of the TFT can also be applied to OFETs. In this case, the TFT is formed by a thin polymer layer, deposited upon a dielectric/metal structure (see Fig. 1.24). The two electrodes (source and drain) make a ohmic contact with the polymer. This type of transistor operates in the *accumulation* regime instead the *inversion* regime as observed in n-MOSFETs [61].

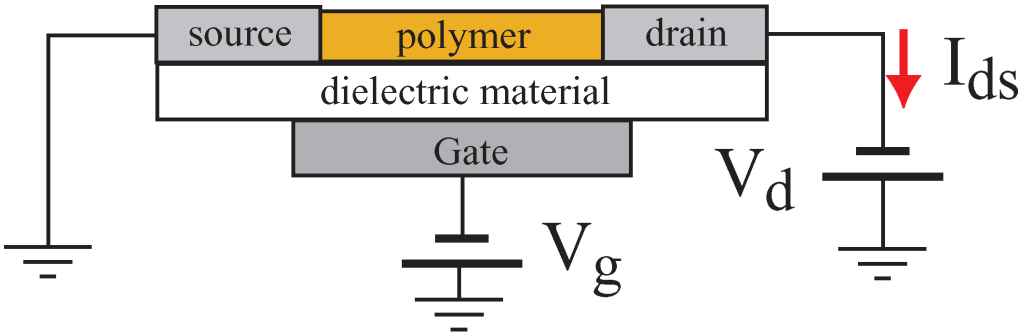

Figure 1.24: *Structure of a thin-film transistor (TFT)*

Once biased as shown in Fig. 1.24, the drain current is controlled via the gate voltage that changes the density of holes accumulated at the interface polymer/dielectric. The I_d at low V_d (linear regime) is described by [157]

$$I_d = \frac{Z}{L}\mu_{TFT}C_i\left(V_g - V_t - \frac{V_d}{2}\right)V_d \qquad (1.5.14)$$

where Z is the channel width, L the channel length, μ_{TFT} the mobility (here assumed constant), C_i the dielectric material capacitance (per unit area) and V_t the threshold voltage. V_t is the voltage for which the channel conductance is equal to that of the polymers layer. In the saturation regime, the transistor operation is explained by

$$I_{d,sat} = \frac{Z}{2L}\mu_{TFT}C_i(V_g - V_t)^2 \qquad (1.5.15)$$

Fig. 1.25 shows the typical current-voltage characteristic of a TFT [158]. The channel was made by α,ω-dihexylsexithiophene and the insulator by poly(methyl-methacrylate) (PMMA).

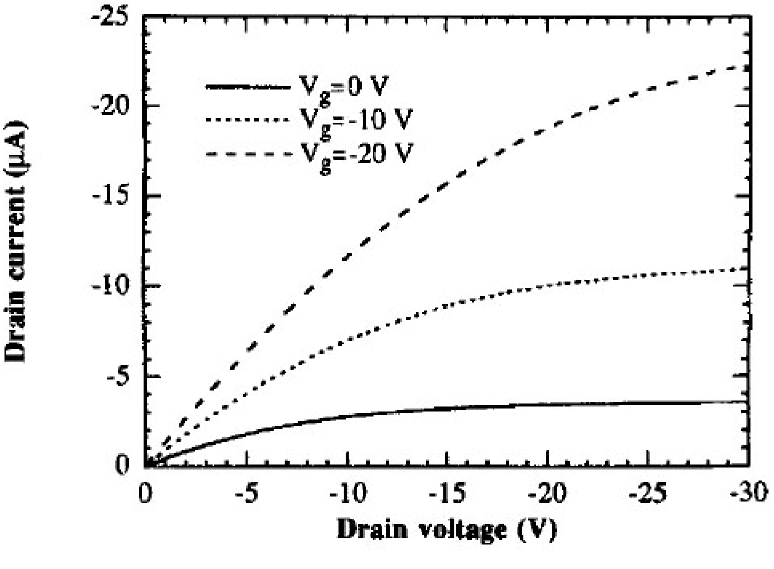

Figure 1.25: *Current-voltage characteristic of a TFT, with a channel made by α,ω-dihexylsexithiophene and the insulator by poly(methyl-methacrylate) (PMMA). Taken from [158].*

As indicated by the current-voltage plot in Fig. 1.25, by driven V_g towards negative values, the drain current tends to increase. I_d also increases with increasing the V_d.

Polypyrrole field-effect transistor

There are two reports in the literature demonstrating that transistor operation in PPy is possible [26, 28]. In the first case [26], the channel was made by a single PPy fiber terminated by cobalt contacts. The PPy fibers were synthesized inside an anodic aluminum oxide template by sequential electrochemical deposition of cobalt, PPy and cobalt. After removal of the template, a single fiber is placed upon a doped-Si/SiO$_2$ substrate where in a subsequent step the electrode regions are defined by e-beam lithography, followed by deposition of a titanium-gold contact. Fig. 1.26 presents the dependence of the drain current (I_d) vs. the drain voltage (V_d) for negative gate voltages (V_g).

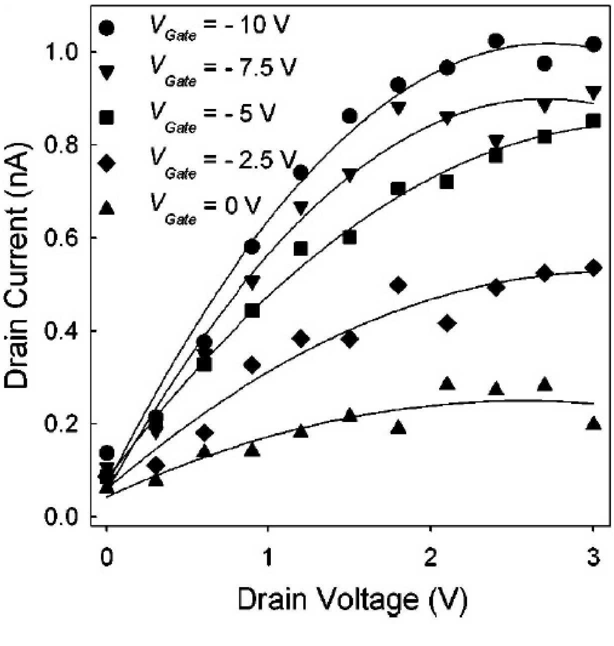

Figure 1.26: *Output characteristic of the PPy transistor. Taken from [26].*

The second PPy transistor [28] was fabricated by vapor-phase polymerization. The oxidant solution (Fe(III)) was spin-coated upon a 500 nm film of poly(vinylcinnamate) (PVCN). The lithographic process is similar to that one described in Section 1.1.4 (the transformation of Fe(III) in Fe(II)). In this device, both channel and gate were made by PPy (see Fig. 1.27 (a)). Fig. 1.27 (b) presents the electrical characteristics of the transistor made by vapor-phase polymerization.

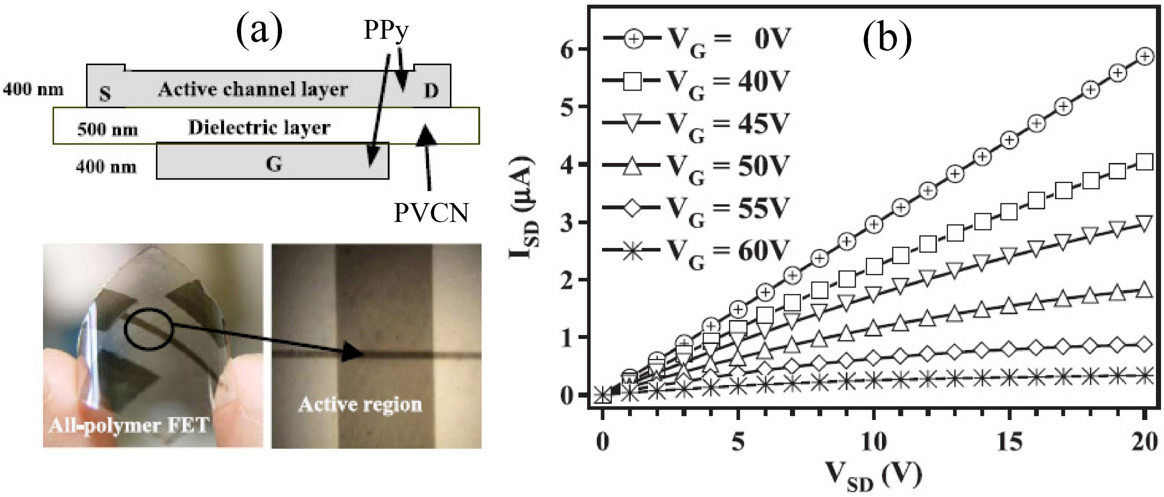

Figure 1.27: *(a) Schematic structure of the PPy transistor made by vapor-phase deposition (top) and the photo of the device (bottom).(b) Electric characteristic of the transistor. Adapted from [28].*

The first point to consider in the evaluation of these devices is the preparation process. In the Co-PPy-Co transistor, the synthesis process is quite complicated, especially the step to separate a single fiber from the template. The second device has the inconvenience of using Fe(III) as oxidant agent. The disadvantages of such a process is described in Section 1.1.4. Both device fabrication processes are definitively not compatible with standard silicon processing. By comparing the electric behavior of both devices with the models discussed above (n-MOSFET and TFT) one can verify that, (a) the Co-PPy-Co transistor behavior cannot be explained by the models, while (b) the electric characteristics of the Fe(III) transistor is in agreement the TFT model [157, 159].

Chapter 2

Sample preparation

This chapter describes both the setup and the processes used for the preparation and the patterning of PPy films. PPy films with thicknesses between 500 nm up to 5 μm were prepared electrochemically by galvanostatic and potentiostatic polymerization. Thin films (from 6 nm to 170 nm) were grown via vapor-phase polymerization.

A simple preparation method for PPy thin films by chemical polymerization is demonstrated. The technique is compatible with conventional silicon processing and is free of contaminating elements such as Fe and Cu. By using the H_2O_2 : HCl - solution to oxidize the Py, homogeneous and smooth PPy films are defined on a doped and oxidized silicon substrate containing a lateral Pt electrode geometry.

Appendix A contains a description of the main the parameters involved in each sample prepared.

2.1 Electrochemical setup

Substrate

In the setup presented here, the film grows directly on the substrate, called *chip*, that acts as the WE and is suited for resistivity studies. The chip (Fig. 2.1) consists of four Pt electrodes, patterned by photolithography. The Pt electrodes were deposited on top of a structure formed by a silicon wafer doped with phosphorus (P) (supplied by Sico Wafer GmbH) and covered by a 100 nm SiO_2 layer. The breakdown electric field of the SiO_2 was found around 4.5×10^6 V/cm. The smallest separation between electrodes is 2 μm.

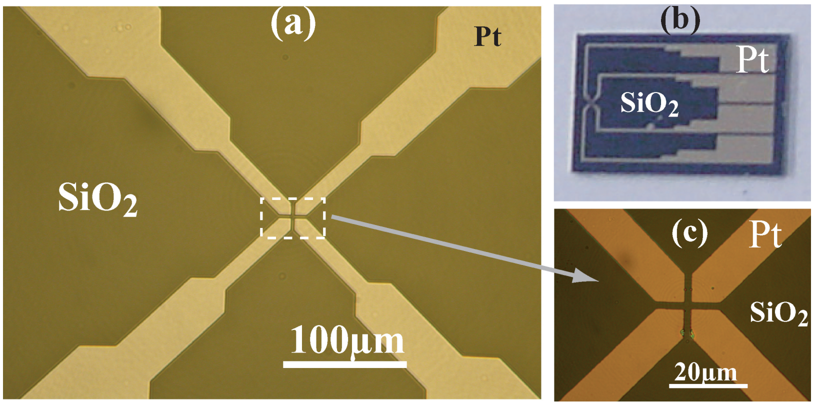

Figure 2.1: *(a) Four Pt electrodes, patterned by microlithography on (b) top of a silicon wafer, doped with P and covered by a* 100 nm SiO_2 *layer. (c) Zoom-in onto the four Pt electrodes with a contact separation of* 2 μm.

Fig. 2.2 shows a sketch of the photolithographic process of the chip. In the first step, the photoresist is spin-coated onto the silicon wafer (Fig. 2.2 (a)). After baking, the solvent is evaporated from the photoresist and the pattern is defined by exposing the coated wafer to UV-light through a mask (Fig. 2.2 (b)). Then, the exposed region in the photoresist is removed by the developer (Fig. 2.2 (c)) and the metallic electrodes are prepared (Fig. 2.2 (d)) by evaporation of 20 nm of Ti followed by 130 nm of Pt. By the liftoff step (Fig. 2.2 (e)), the photoresist is removed and the metallic layer in contact to the SiO_2 surface remains. The electrodes were processed by IMTEK at the University of Freiburg.

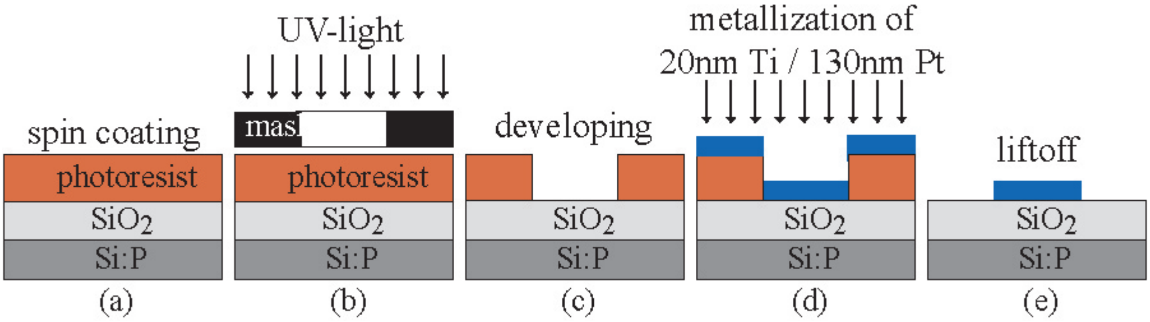

Figure 2.2: *Sketch of the photolithographic process on the chip. (a) The photoresist is spin-coated onto the silicon wafer. (b) After baking the pattern is performed on the photoresist surface by exposing the coated wafer to UV-light through a mask. (c) The pattern on the photoresist is developed and (d) the metallic electrodes are made by evaporation of* 20 nm *of Ti followed by* 130 nm *of Pt. (e) By liftoff, the photoresist is removed and the metallic electrode in contact with the* SiO_2 *surface remains.*

Glass electrode holder

In order to grow a PPy film, the chip must be inserted in the glass electrode holder (Fig. 2.3 (a)). The holder is a glass probe with four Pt contacts and a CE placed in a teflon head (see Fig. 2.3 (b)). The four Pt contacts are mounted at the head so that the pads at chip are clamped to them (see inset in Fig. 2.3 (b)). Each contact at the probe can be externally and independently connected to the potentiostast/galvanostat.

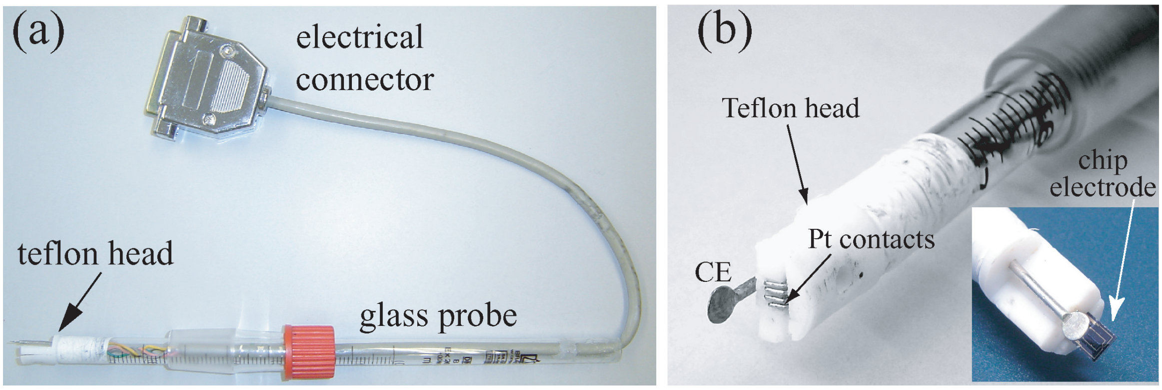

Figure 2.3: *(a) The glass probe. (b) Teflon head and (inset) the chip inserted in the head.*

The CE is made by a 4 mm diameter Pt disc assembled 5 mm away from the WE. In this work, all the electrochemical potentials are measured against an Ag/AgCl reference electrode (RE), whose distance from the WE is adjusted for minimization of the electrolyte bulk effects.

Electrochemical cell

The electrochemical experimental setup consists of two sets of three-electrode electrochemical cells (Fig. 2.4 (a)). One set is used for polymerization and the other one for characterization by cyclic voltammetry (CV). Both cells are connected to a three-terminal potentiostast / galvanostat Metrohm μ-Autolab (Fig. 2.4 (b)). The cells are designed to keep the whole system under inert atmosphere of argon (Ar) during growth and CV. The growth cell is coupled to a heat exchanger to allow the synthesis at variable temperatures (Fig. 2.4 (c)). Here, the growth temperature can be set from room temperature down to 213 K, by connecting the heat exchanger to an ethanol cooling system.

PPy can be synthesized electrochemically by the followings techniques: galvanostatic (constant current) [64], potentiostatic (constant potential) [65], or potentiodynamic (varying the potential and measuring the current) [66].

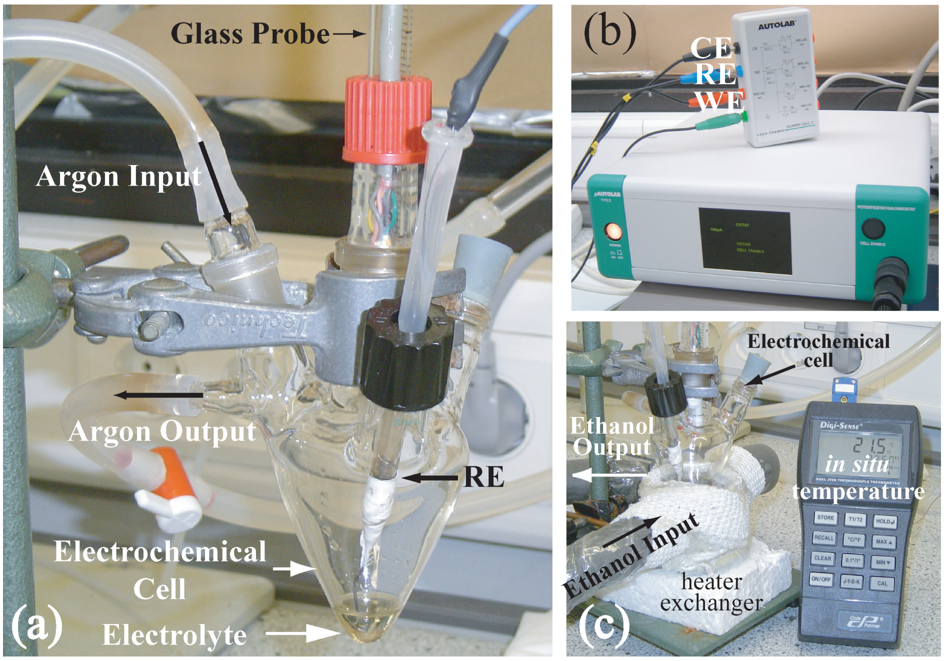

Figure 2.4: *(a) The three-electrode electrochemical cell, (b) potentiostast/galvanostat Metrohm μ-Autolab and (c) the electrochemical cell connected to a heat exchanger.*

2.2 Galvanostatic polymerization

Both current density and growth temperature play an important role in determining the electrochemical [66] and electronic [14] characteristics of PPy films. For this reason, the PPy films were grown galvanostatically under Ar overpressure and with the synthesis solution at temperatures of 293 K and 273 K, within an accuracy of 0.1 K. The electropolymerization was carried out at a current density of 6.6 mA/cm^2, applied for 30 s, which was supplied by a standard three-electrode potentiostast/galvanostat.

The electrolyte for polymerization was formed by 0.5 M of the conductive salt tetra-n-butylammonium hexafluorophosphate (TBAPF$_6$), 0.5 M Py, 1% distilled water, and 1% of hydrochloric acid (HCl) in acetonitrile (ACN). Py and ACN were distilled under argon atmosphere before the solution preparation, while TBAPF$_6$ was vacuum dried immediately before use. After preparing the mixture, the solution was purged with argon for 20 minutes.

The current applied between working and counter electrode starts oxidizing the monomer Py to Py$^+$ at a constant rate (see Chapter 1, Fig. 1.2). Fig. 2.5 shows the potential of the WE, measured against the RE (V$_{\mathrm{WE}}$ (vs. Ag/AgCl)) as a function of the polymerization time for growth at 273 K (sample EG01) and 293 K (sample EG06, see details in Appendix A).

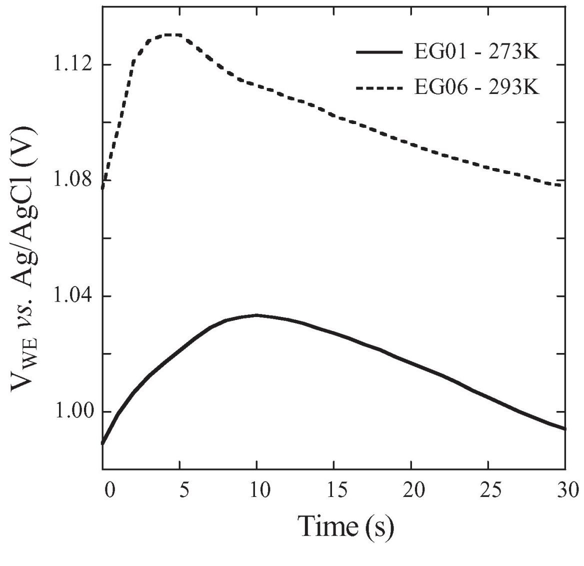

Figure 2.5: V$_{\mathrm{WE}}$ (vs. Ag/AgCl) *as a function of the polymerization time for samples at* 273 K *(sample EG01) and* 293 K *(sample EG06), grown galvanostatically at* 6.6 mA/cm^2 *during* 30 s.

The plot shows that V_{WE} (vs. Ag/AgCl) decreases with the polymerization time after reaching a maximum after $\sim$ 5 s for EG06 and $\sim$ 9 s for EG01. This dependence is associated with the reduction of the reactivity of the system, since the amount of Py available close to the WE tends to decrease [59]. The reactivity also decreases by reducing the temperature, as observed from the temperature dependence of V_{WE} (vs. Ag/AgCl). Consequently, by reducing the temperature, for the same polymerization time and density of current, the amount of polymer produced decreases.

Due to lateral growth, the films formed on the four WE merged at film thicknesses of about 4 μm, thus enabling electrical four-probe measurements. Fig. 2.6 shows the four WE after the polymerization in (a) and the chip-carrier assembling, for a sample grown at 293 K in (b).

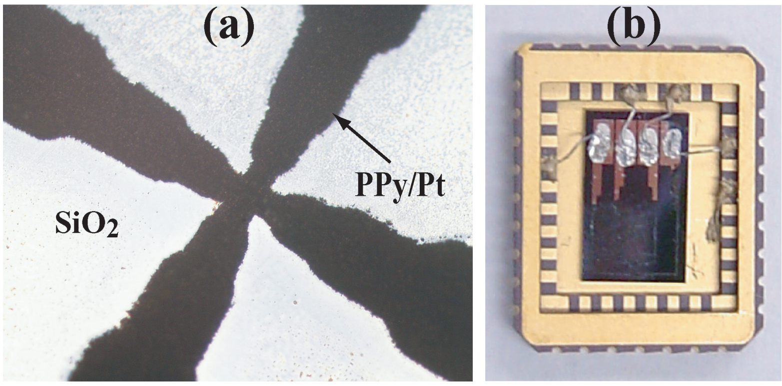

Figure 2.6: *(a) The four WE after the polymerization and (b) the chip-carrier assembly, for a sample grown at* 293 K*.*

2.3 Potentiostatic polymerization

As discussed in Chapter 1, the amount of PPy I and PPy II can be changed by varying the polymerization potential and temperature. Therefore, several PPy films were prepared by potentiostatic polymerization at a temperature of 243 K and different growth potentials (from 0.52 V to 1.60 V). Potentials below 0.52 V were below the activation threshold of the polymerization process, while for potentials above 1.60 V, the solution degraded. The polymerization was carried out in a solution of 0.1 M of the conductive salt lithium perchlorate ($LiClO_4$)

and 0.5 M of Py in propylene carbonate (PC). As will be shown in Chapter 3, the amount of PPy II can be increased by switching the polymerization solution from ACN to PC. The whole system was kept under Ar overpressure during the polymerization. Fig. 2.7 presents the polymerization current as a function of the time for samples grown at different potentials. More details about the potentiostatically grown samples are given in Appendix A.

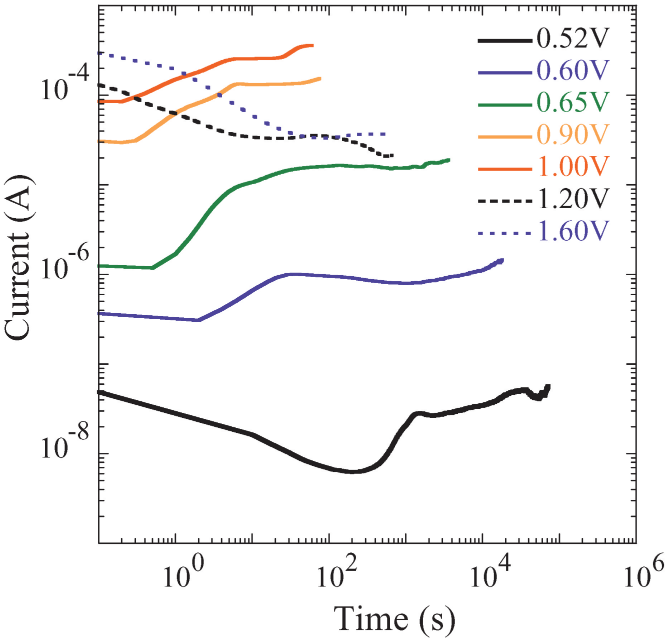

Figure 2.7: *Current as a function of the polymerization time for samples grown under potentials ranging from* 0.52 V *to* 1.60 V*. The polymerization was carried out at temperature of* 243 K.

The film growth rate increases dramatically as the polymerization potential (V_p) is increased from 0.52 V and 1.00 V. The time necessary to grow a PPy film with a thickness of 500 nm at 0.52 V was about 24 hours, in contrast to 1 minute at 1.00 V. It was observed that at low temperatures and potentials, the lateral growth rate is higher that one in vertical direction. For this reason, films with thicknesses smaller than the electrode separation (2 μm) could be connected during the polymerization. In the same range of potentials, the current during growth shows a weak peak at the beginning (after 10 s to a few 100 s), followed by a decrease and then again an increase in time. For potentials higher than 1.20 V the rate of film formation drops. The current during growth drops in the first 30 s and tends to an almost constant value roughly one order of magnitude lower afterwards.

At potentials higher than 1.00 V, the solution began to change its color from transparent to light brown during the polymerization process. The light brown color originates from PPy that gets polymerized in solution, which occurs at high potentials when the voltage drop across the solution is enough to start the polymerization process.

Also, the PPy adhesion to the Pt electrodes is a critical point for films prepared above 1.00 V. These films detached from the electrodes after drying, making the sample preparation unfeasible. The optical microscope images indicate qualitatively that the surface roughness is strongly depending on the polymerization potential. By assuming that the porosity increases with increasing roughness, it is possible to associate the adhesion problem to a reduction of the contact area between Pt and PPy. Then, this reduction of contact area is mostly due to the insertion of a solvent layer or simply due to vacancies between PPy and Pt.

During polymerization, the current was monitored and from it, together with the measured film thickness and area, the charge density involved in the whole synthesis process was calculated. Fig. 2.8 shows the charge density involved during the synthesis as a function of the polymerization potential (V_p).

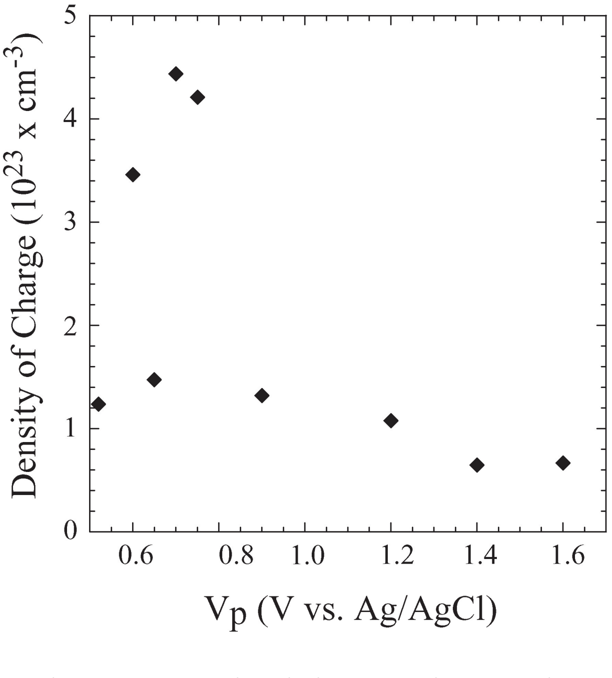

Figure 2.8: *Charge density involved during the synthesis as a function of the polymerization potential (V_p) for the samples synthesized at* 243 K.

The charge density during the growth increases up to 0.70 V and then drops to an almost constant value for V_p higher that 1.00 V. It is important to point out that the charge density value calculated does not necessarily equal the density of embedded counterions. Rather than,

2.4 Vapor-phase growth

The synthesis with $H_2O_2 : HCl$ as oxidizing agent to prepare PPy in solution is an established technique [71, 72, 73]. Nevertheless, in order to get a better control of the polymerization process, instead of mixing the Py monomers with the $H_2O_2 : HCl$ solution, we evaporate them. Fig. 2.9 presents a sketch of a home-made vapor-phase cell used to prepare PPy films. The cell is divided into four parts: heater, Py source, sample chamber and sample cooler. Once evaporated, the monomers are carried by the Ar flux through the connecting tube until reaching the sample chamber, where the substrate covered by the oxidizing agent is located. As the Py monomers get in contact with the solution, they polymerize at the surface of the droplet. This setup allows polymerization control by tuning the Py evaporation temperature (from room temperature up to 473 K), the sample temperature (from room temperature down to 223 K), the argon flux, and the growth time.

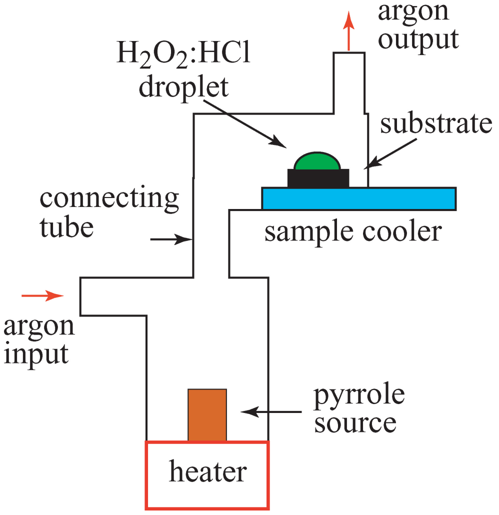

Figure 2.9: *Sketch of the vapor-phase cell for chemical polymerization of PPy.*

Fig. 2.10 shows a picture of a glass substrate covered by a droplet of $H_2O_2 : HCl$ (1000:1 volume fraction), before and after a 30 s exposition to Py monomers, carried by a flux of argon of 0.1 l/h (sample VPH01).

The sample was at room temperature during film formation. Commercially available liquid Py (Aldrich) was evaporated from a source by heating it to 383 K. H_2O_2 acts as oxidizer, while HCl provides the Cl^- counter ions (e.g., the equivalent of acceptors) required for charge neutrality.

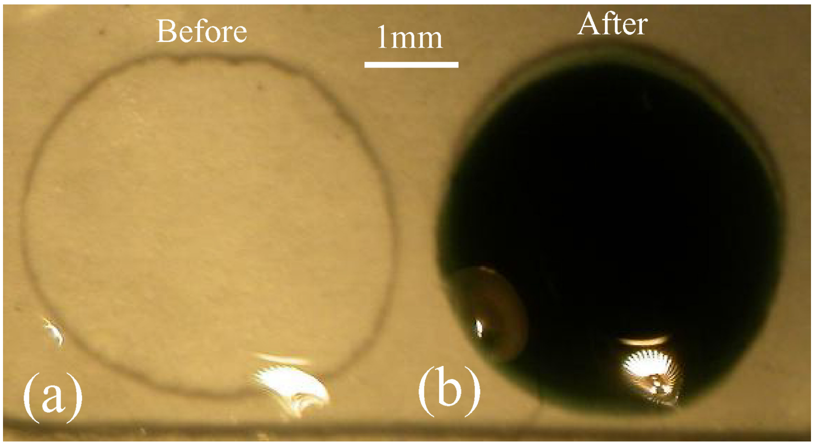

Figure 2.10: *Sample VPH01 - Glass substrate covered by a droplet of* $H_2O_2 : HCl$ *(1000:1 volume fraction), (a) before and (b) after a* 30 s *exposition to Py monomers carried by a flux of argon of* 0.1 l/h.

In spite of the better control of polymerization gained, at first sight, it appears that the PPy obtained is still in solution and cannot be used as a thin film. However, after rinsing the substrate with DI water, it is possible to visualize by optical microscopy that during the polymerization, PPy is not only formed in solution (Fig. 2.10 (b)), but also grows as thin film on the substrate surface, an effect that apparently went unnoticed up to now.

Fig. 2.11 (a) presents an optical image of the glass substrate surface, coated with a thin PPy film. By zooming the image (Fig. 2.11 (b)), it is verified that the film gets thinner from the edge to the center of the droplet. This observation suggests that (a) the polymerization occurs from the edge to the center and (b) that the monomers can diffuse in solution up to a certain distance without reacting with the oxidizing agent.

In fact, this is expected since the concentration of oxidizing agent tends to decrease from the edge (where the polymerization starts at $t = 0$) to the center of the droplet.

Fig. 2.12 shows the atomic force microscope (AFM) images of the sample VPH01 at the points I, II and III, as noted in Fig. 2.11 (b). The film has the well-known morphology of PPy films made by other

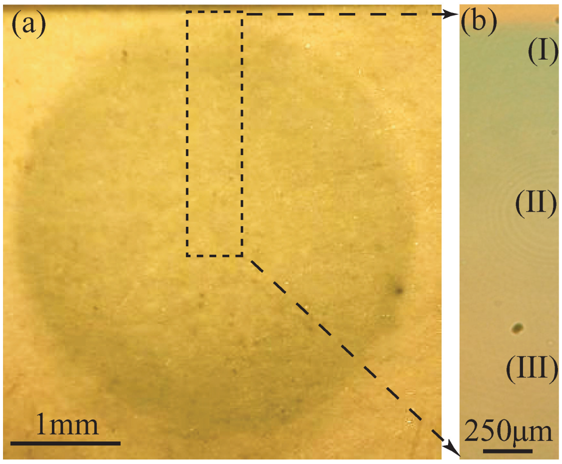

Figure 2.11: *(a) Optical image of the sample VPH01, a glass substrate coated with a thin PPy film. (b) Zoom at the region of interest, showing that the film gets thinner from the edge to the center of the droplet.*

techniques, i.e., egg-like structures with a characteristic size depending of the film thickness [33, 64, 141, 142, 143].

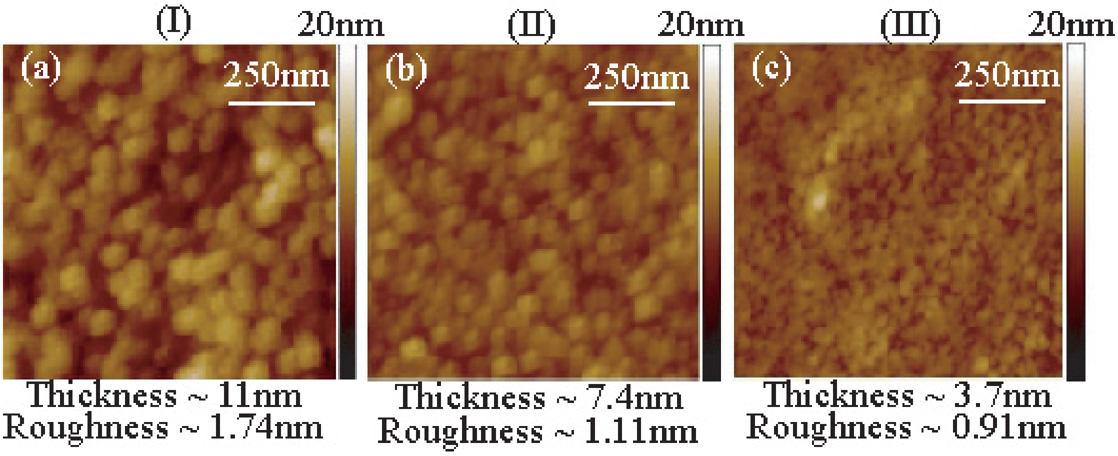

Figure 2.12: *Atomic force microscope (AFM) images of the PPy film at the points I (a), II (b) and III (c), as noted in Fig. 2.11(b).*

2.5 Thin film patterning

Substrate

In case the PPy film is to be applied as active layer in electrical devices, the patterning was made on a substrate formed by Pt contacts (thickness 130 nm), patterned by optical lithography on a thermally oxidized As-doped silicon wafer (resistivity 5 mΩcm) (see Fig. 2.13 (a)).

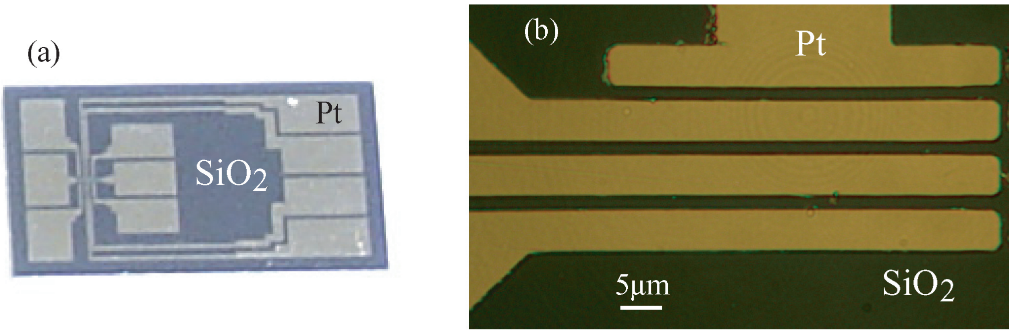

Figure 2.13: *(a) Substrate formed by Pt contacts (thickness* 130 nm*), patterned by optical lithography on a thermally oxidized As-doped silicon wafer. (b) Zoom-in from the four electrode contacts region.*

The oxide has a thickness of 100 nm and a breakdown electric field of $\sim 4.5 \times 10^6$ V/cm. The separation between the Pt electrodes is 2 μm (Fig. 2.13 (b)). The photolithographic process used to pattern the Pt electrodes onto the silicon substrate was the same that one described in Fig. 2.2 at section 2.1. The sample was processed by IMTEK at the University of Freiburg.

Procedure to pattern the polypyrrole thin films

Prior to the polymerization step, conventional photolithography was used to define a photoresist (Microchemicals AZ 5214E) pattern acting as a deposition mask. A 5 μm wide stripe-line channel was used as pattern and placed perpendicular to the four Pt electrodes (Fig. 2.14). After development, the SiO_2 surface was passivated by a hexamethyl disilazane (HMDS) layer. HMDS is normally used to improve the adhesion of photoresist to SiO_2 and to reduce the effect of surface states by replacing the hydroxyl groups at the surface by methyl groups [160, 161, 162].

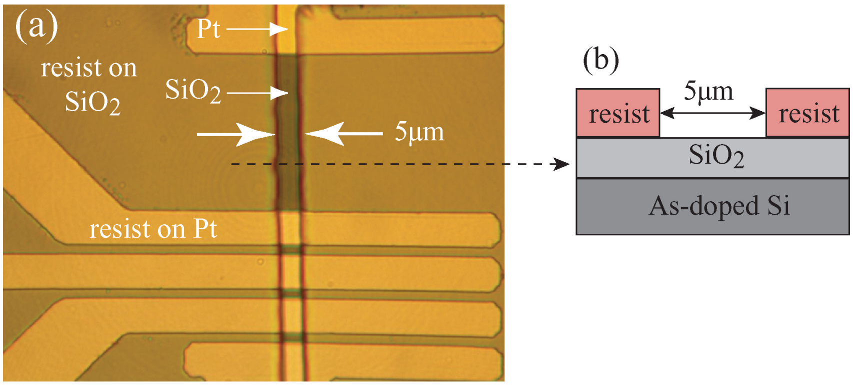

Figure 2.14: *(a) 5 μm wide stripe-line channel patterned by conventional photolithography. (b) Cross section draw of the 5 μm wide stripe-line channel.*

To prepare the sample VPH02, the patterned substrate was mounted inside of the vapor-phase cell under argon flux of 0.1 l/h and a pressure of 1 atm. Py was evaporated from the source at 383 K during 3 minutes, after a droplet of H_2O_2 : HCl (1000:1 volume fraction) being deposited on the surface, with the substrate at room temperature. After polymerization, the process gives rise to a PPy film at the surface (*film A*) of the droplet (see in Fig. 2.15 (a)) and also to PPy in solution. This result differ from the sample VPH01 that exhibits just PPy in solution at a first view. The main reason for such difference is the shorter polymerization time of 30 s for VPH01, in contrast with 3 minutes in the sample VPH02. Species of *film A* were investigated with AFM on samples that were dried (Fig. 2.15 (b)).

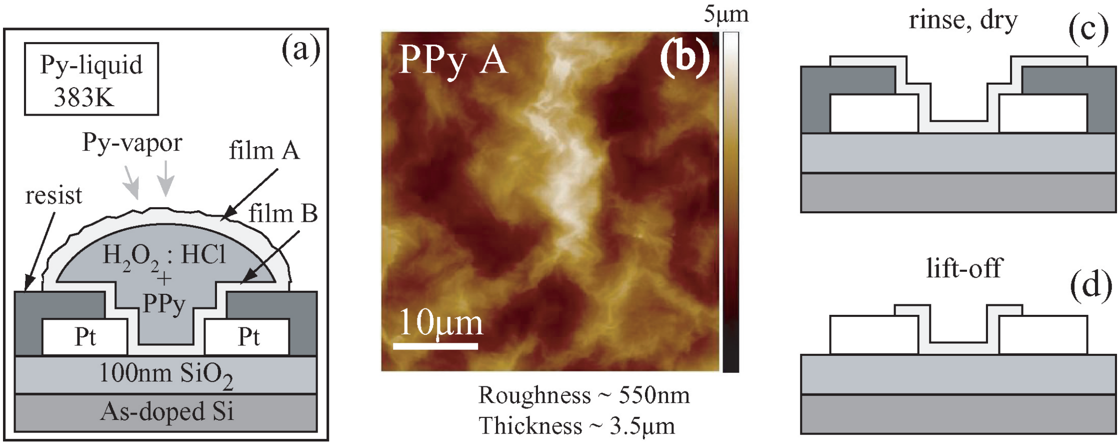

Figure 2.15: *(a), (c) and (d), cross sectional schemes illustrating the sample preparation. (b) AFM image of a dried PPy film A.*

Film thicknesses between 500 nm and 5 μm that scale linearly with the exposure time are found, with a roughness of about 15% of the thickness. In addition, a much thinner and comparatively flat film (*film B* in Fig. 2.15 (a)) forms at that part of the substrate surface which is covered by the droplet.

After polymerization, the solution with *film A* on top is removed by rinsing the sample in DI water (Fig. 2.15 (c)). Afterwards, the photoresist is removed with ethanol in a lift-off process (Fig. 2.15 (d)), and a well-defined geometry of *film B* remains (Fig. 2.16).

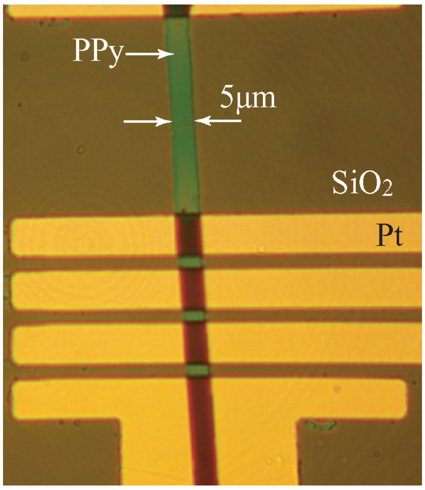

Figure 2.16: *The type* B *PPy film (vertical stripe-line) runs across the Pt electrodes on top of silicon oxide.*

In the standard silicon photolithographic process, the photoresist is removed by either acetone or the appropriate remover for the AZ 5214E (AZ 100). This procedure was avoided since the PPy films demonstrated signs of degradation after to be exposed to these components. The degradation was detected by the increase of the sample resistance (more than 100%), without any evidence of reversibility. The reversibility was checked by washing the sample with DI water and by keeping the sample in vacuum for more than 24 hours.

The *film B* after the lift-off process can be used in applications and its morphology studied with an atomic force microscope (Fig. 2.17 (a)).

The analysis reveals, in this example, an average film thickness of 40 nm with a roughness of 6 nm. The film thickness can be well controlled via the Py vapor exposure time. In addition, the roughness (single standard deviation) is found to scale approximately linearly with the film thickness (Fig. 2.17 (b)). Connected films as thin as 6 nm with a roughness of 1.5 nm could be prepared this way.

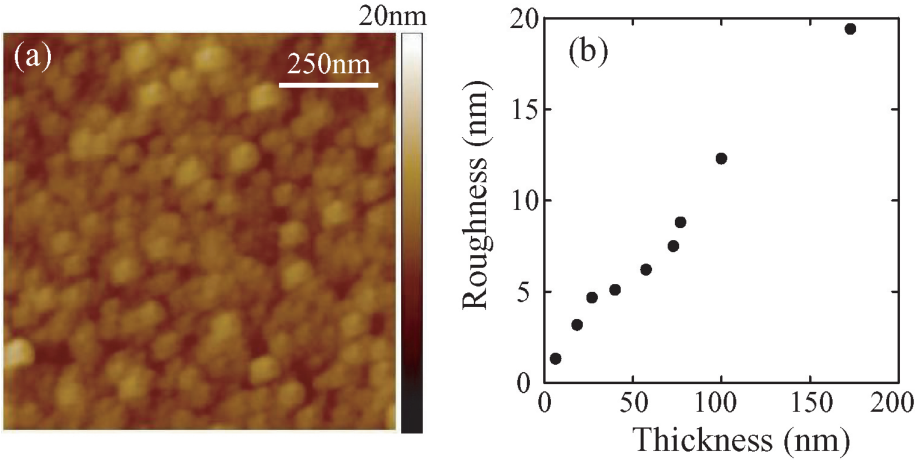

Figure 2.17: *(a) AFM image of the type* B *PPy film morphology in the active region over an area of* $1\,\mu\mathrm{m}^2$*. The gray scale represents the height. (b) Thickness dependence of the roughness.*

By decreasing the synthesis temperature, the rate of polymerization also decreases. The time necessary for the polymerization of a PPy film with thickness of 40 nm was 30 times higher at 278 K than at 293 K (60 minutes and 2 minutes, respectively).

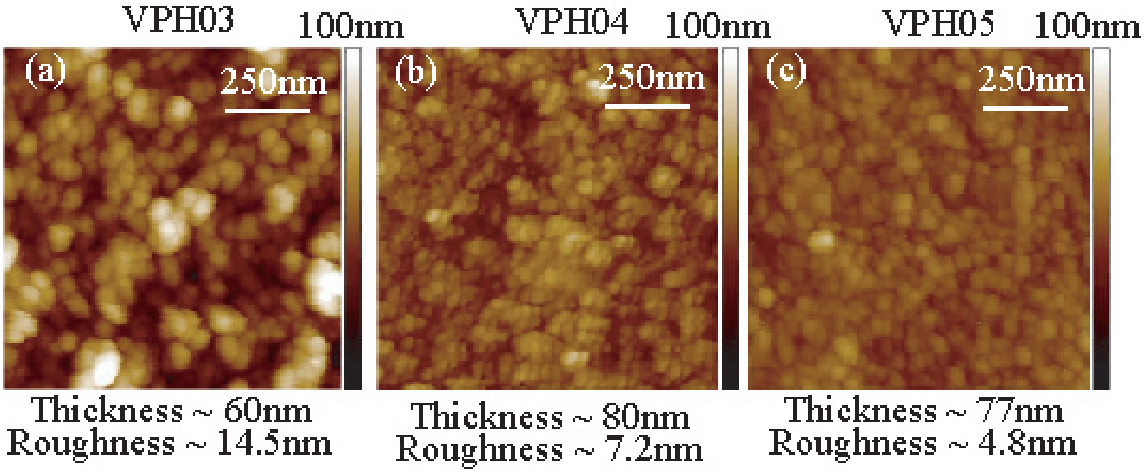

Thickness ~ 60nm
Roughness ~ 14.5nm

Thickness ~ 80nm
Roughness ~ 7.2nm

Thickness ~ 77nm
Roughness ~ 4.8nm

Figure 2.18: *AFM images of the PPy film grown at different temperatures. The sample VPH03 was grown at 293*K*, VPH04 at 282*K *and VPH05 at 277.5*K.

The roughness and the average size of the egg-like structure also shows a dependence of the growth temperature. Fig. 2.18 presents the AFM image of three PPy films with almost the same thickness but grown at different temperatures. The sample VPH03 was grown at 293 K, VPH04 at 282 K and VPH05 at 277.5 K. For more details, see Appendix A.

The size of the egg-like structure for the sample VPH03 was around 70 nm and by decreasing the growth temperature the structure size decreases to around 40 nm for both samples VPH04 and VPH05. The roughness also shows a dependence of the growth temperature as indicated in Fig. 2.18. Therefore, by keeping the solution concentration (H_2O_2 : HCl (1000:1 volume fraction) constant and by using the same type of substrate, the surface roughness of the PPy thin films can be controlled by both the film thickness and the growth temperature. Additionally, it was observed that the polymerization on Pt was faster than on SiO_2.

Besides using Si/SiO_2 as substrate, the patterning process was also successfully reached on glass, Poly(methyl methacrylate) (PMMA), Au films on glass and steel as well. On the other hand, in substrates like gallium arsenide, aluminum and cobalt, which can be etched by H_2O_2 : HCl, the deposition of PPy was not reached. Fig. 2.19 shows a 40 nm tick PPy hall bar defined of glass. The smallest PPy structure patterned has a size close to the photolithographic limit ($\sim 2\,\mu$m).

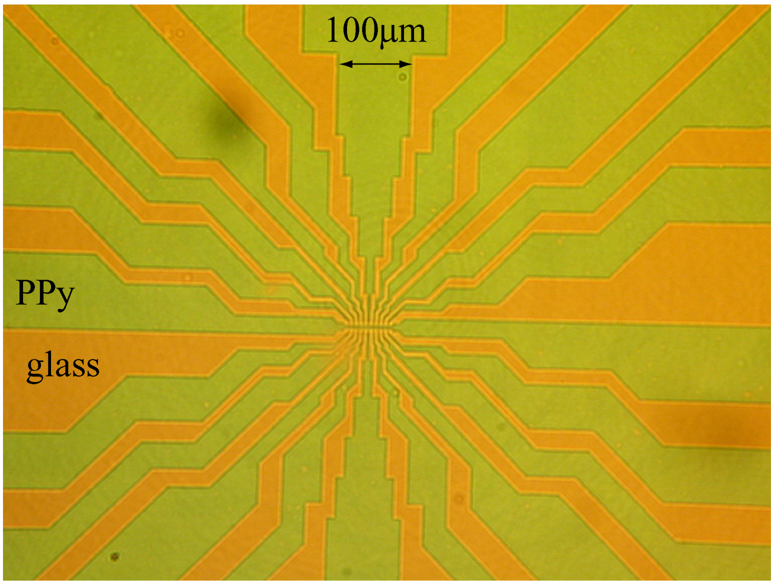

Figure 2.19: *A 40*nm *tick PPy hall bar defined on glass.*

Chapter 3

Characterization of electrochemically grown polypyrrole films

In this chapter, the PPy films grown by electropolymerization are characterized mainly by electronic transport combined with CV and UV-vis spectroscopy.

In the galvanostatically grown samples, the lower polymerization temperature increases both the fraction of PPy II and its conductance and can even drive the films from the insulating into the metallic phase. This phenomenological correlation raises the question that is addressed below, namely whether there is a causal dependence between the PPy II contents and the transport properties. The fraction of PPy II in the films was varied by two means, namely by changing the polymerization temperature as well as by voltammetric cycling. From a combination of UV-vis spectroscopy with electronic transport measurements, at first sight, a surprising picture emerges: PPy II consists of oligomeric chains composed of 8 monomers at most, while PPy I chains are significantly longer. Nevertheless, a larger fraction of PPy II increases the conductivity. It is concluded that the chain length is of subordinate relevance for the resistivity but rather the short-range order as well as the inter-chain separation are most important.

The polymerization potential is also reported as a parameter that can influence the composition of PPy films [87]. The goal in this section is to evaluate the changes in the electric properties of the PPy films by varying the polymerization potential $\mathrm{V_p}$. By changing $\mathrm{V_p}$, the contents of PPy I and PPy II in the film produced change significantly. These changes affect, and can be directly detected in, the electronic transport.

The process used to prepare the samples investigated here was described in Chapter 2. A list of the samples is found in Appendix A.

3.1 Galvanostatically grown films

3.1.1 Electrochemical characterization

After polymerization, the samples grown at 273 K and 293 K, (EG02-EG05 and EG07-EG10, respectively) were discharged (reduced) and recharged (oxidized) by CV in a monomer-free solution of 0.5 M of $TBAPF_6$ in ACN. The cycling was performed with a starting voltage of 1 V, a minimum voltage of −0.8 V (against Ag/AgCl), and a scan rate of 10 mV/s. Fig. 3.1 (a) shows the cyclic voltammogram of a sample grown at 293 K that underwent four cycles (EG10).

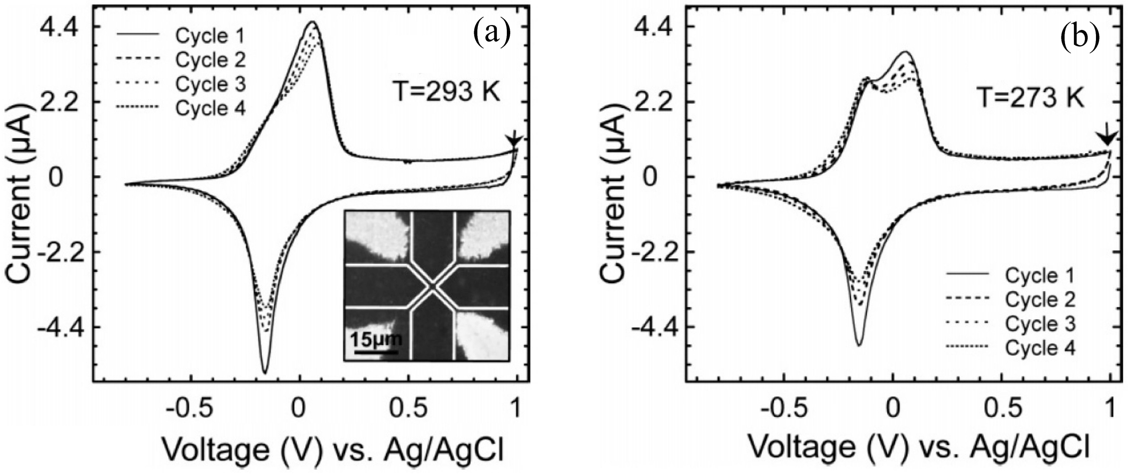

Figure 3.1: *Current-to-voltage characteristics of four consecutive voltammetric cycles for a sample grown (a) at* 293 K *(EG10) and (b) at* 273 K *(EG05). The arrow denotes the starting point. The inset shows the geometry of the PPy films (gray), as seen in an optical microscope. The edges of the Pt electrodes below the film are indicated by the white lines (solid drawn).*

While the reduction peak appears at a constant voltage of −160 mV, a shift of the oxidation peak toward higher potentials is observed. This observation is taken as an indication that *during CV, PPy II is transformed into PPy I*, in agreement with results reported earlier [87]. The presence of PPy II is also indicated by the shoulder in the oxidation peak at −150 mV. Furthermore, a reduction of the peak amplitudes is observed, which is most pronounced between the first and the second cycle. In the cycles after the first one, this apparent decay is usually attributed to the nonzero cycling speed, while the difference between the first two cycles again indicates a structural change in the polymer film, which will be of importance below. The voltammograms of samples grown at 273 K (b) show a more pronounced shoulder on the oxidation peak, indicating that the fraction of PPy II has increased. The PPy I oxidation peak again shifts to higher potentials as the number of cycles increases. From the CV it is clear that *low temperature growth increases the fraction of PPy II.*

3.1.2 UV-vis absorption characterization

To force the formation of PPy I or PPy II, both the temperature and the current [87] were varied in this experiment. To obtain preferably PPy I, the electropolymerization was carried out at room temperature (293 K) using a current of 550μA (sample EG11). To obtain mainly PPy II, electropolymerization was performed at 243 K with a current of 100μA (sample EG12). After polymerization, the films were reduced at a potential of −1.2 V and their UV-vis spectra were measured at room temperature. The UV-vis spectroscopy was made in cooperation with the group of Prof. Heinze at the Department of Physical Chemistry of the University of Freiburg.

PPy samples suited for UV-vis spectroscopy (EG11 and EG12) were polymerized under the same conditions as sample EG01. The polymer was deposited on a quartz substrate coated with indium tin oxide (ITO) where the electroactive area was about 1.5 cm^2. The electrochemical experiments were carried out under argon atmosphere. A Pt grid served as the counter electrode. The reference electrode was an Ag wire. An EG&G PARC Model 175 Universal programmer and a Jaissle potentiostat-galvanostat IMP 88 PC were used for electrochemical control and data recording. The UV-vis spectra were recorded on a Perkin-Elmer Lambda 9.

Electrochemical data and UV-vis spectra obtained at different temperatures give new insights into the structural differences between PPy I and PPy II. As can be seen in Fig. 3.2 (a), the film produced at

293 K and high current (sample EG11) shows the typical cyclic voltammogram of PPy I. The corresponding UV-vis spectrum of PPy I has an absorbance maximum at 426 nm and a shoulder at about 450 nm (Fig. 3.2 (c)). The cyclic voltammogram of the film prepared at 243 K and lower current (sample EG12) shows two oxidation peaks and one reduction peak (Fig. 3.2 (b)). The anodic peak at −0.12 V indicates the oxidation of PPy II, while that at a potential of 0.1 V corresponds to the oxidation of PPy I. Considering the cyclic voltammogram, this film consists of mainly PPy II. In the UV-vis spectrum of the same material after discharging, there is a broad absorbance maximum at

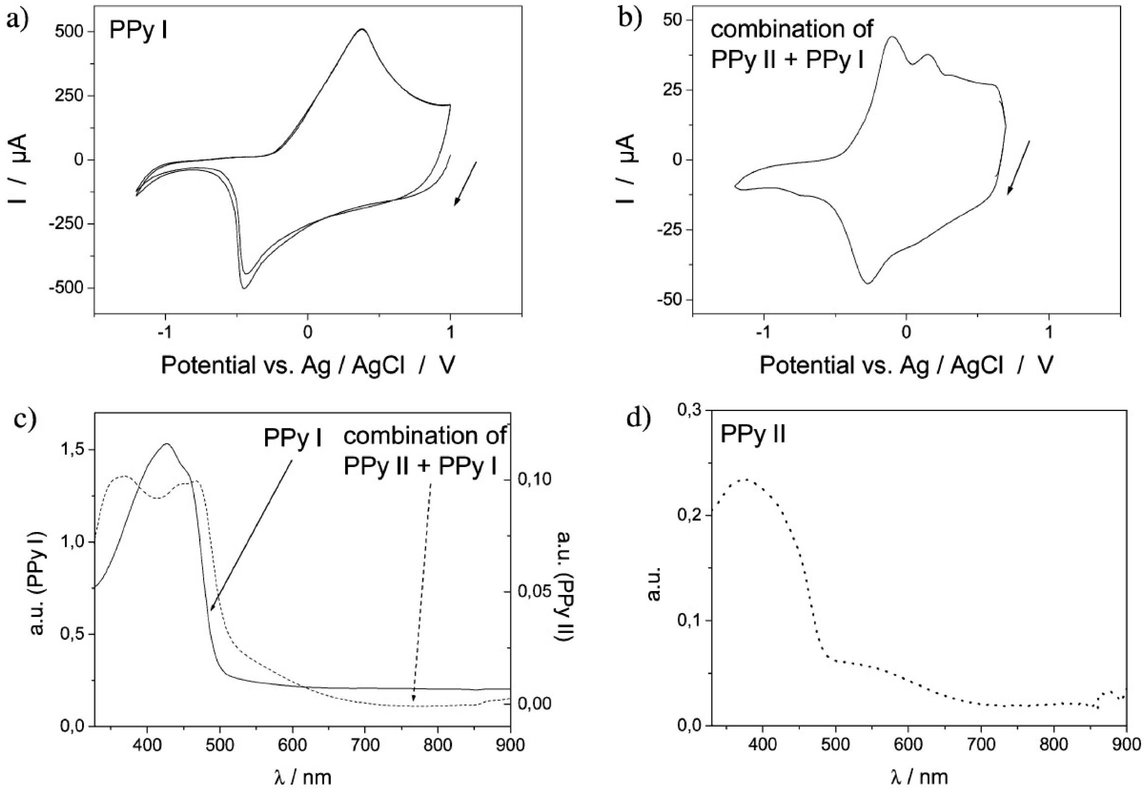

Figure 3.2: *Cyclic voltammograms and UV-vis spectra of PPy films. The films were galvanostatically polymerized under different conditions: (a) sample EG11 in which the main product is PPy I (solid line in c); (b) sample EG12, the main products is a combination of PPy II + PPy I (dashed line in c); (c) UV-vis spectra of PPy II and I, grown at* 293 K *after reduction at a potential of* −1.2 V *(*$TBAPF_6$ *in ACN); solid line represents the pure PPy I samples; dashed line represents the sample with a combination of PPy II and PPy I. (d) UV-vis spectra of the sample EG13, grown at* 293 K*, after reduction at a potential of* −1.2 V *(*$LiClO_4$ *in PC). It is represented by a dotted line and contains mainly pure PPy II.*

about 386 nm for PPy II (Fig. 3.2 (c)). A second absorbance band in the range between 450 and 470 nm is caused by a small portion of PPy I. In addition, the signal caused by PPy I in the UV-vis spectrum can overlap the absorbance curve of PPy II and generates an additional broad absorbance maximum in the long wavelength range. In the given solvent/electrolyte system (ACN / $TBAPF_6$), PPy II could not be obtained in pure form. The synthesis of PPy with $LiClO_4$ in PC (sample EG13) produced films of almost pure PPy II showing an absorption band at 380 nm (Fig. 3.2 (d)).

The number of pyrrole units (n) in a chain can be recalculated from the absorbance maximum by equation 3.1.1, the result of a linear regression of data published by Zotti and coworkers [136] (see Fig. 1.18):

$$\nu = 22676\,\mathrm{cm}^{-1} + 25719\,\mathrm{cm}^{-1} \cdot (1/\mathrm{n}) \qquad (3.1.1)$$

where ν is the wavenumber. By using equation 3.1.1, the number of pyrrole units of pure PPy I in the neutral state is about 32 (max. = 426 nm) to 64 (max. = 450 − 470 nm) and that of PPy II is 8 (max. = 386 nm) up to 12 (max. = 403 nm). Obviously, in the combination of both PPy components, PPy I contains longer chains (number of pyrrole units > 64). It may be that the chains are cross-linked. It should be noted that a correlation between the wavelength and the number of units in the PPy chain ends at a value of 440 nm. Therefore, the number of pyrrole units for longer chains is not precise. Fig. 3.3 shows the data from Zotti [136] and the values calculated for PPy I and PPy II, from Fig. 3.2, included in the same plot. Normally, short monodisperse oligomeric chains form well-ordered structures on deposition [163, 164]. Electrochemical quartz crystal microbalance studies of freshly polymerized PPy II films reveal an increase in mass of these films during repetitive redox switching [87]. This alteration occurs due to the incorporation of solvent and electrolyte into the polymer matrix. The result is an expansion of the polymer volume; therefore, distances increase between the polymer chains and the structural order decreases. Moreover, structural changes occur during repetitive cycling [97], and PPy II is transformed into PPy I including a partial formation of a stable network [87].

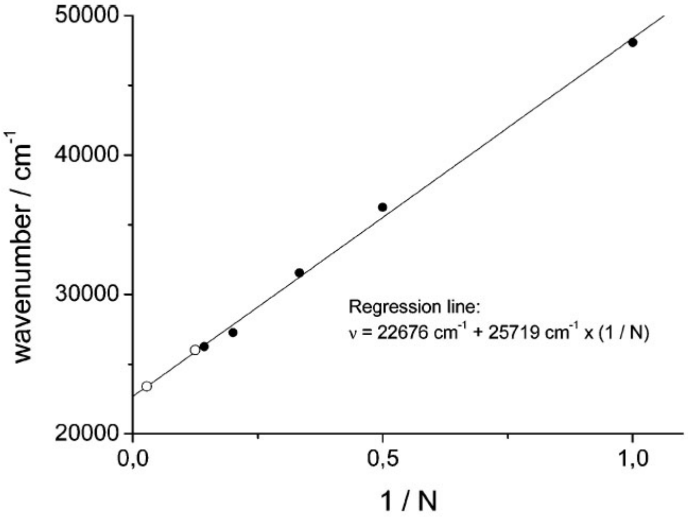

Figure 3.3: *Correlation of wavenumbers vs. 1/n (n = Number of pyrrole units for different oligopyrroles): correlation factor r = 25 719, filled dots, Zotti et al. [136] (see Fig. 1.18); open dots, data taken from Fig. 3.2.*

3.1.3 Resistivity measurement method

The resistances were obtained by standard two- and four-terminal lock-in techniques, with an applied current of 100 nA at a frequency of 13.5 Hz. Fig. 3.4 illustrates both two- and four-terminal configurations. The film resistivity (ρ_{4p}) is obtained from the four-probe resistance R_{4p} by

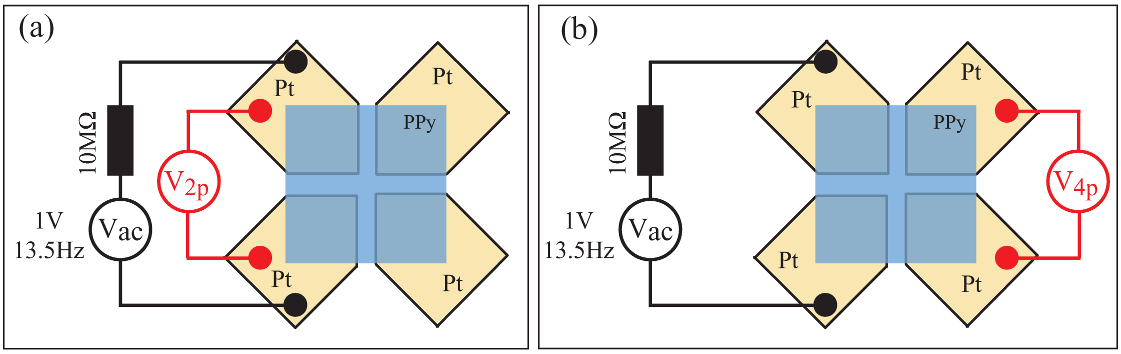

Figure 3.4: *Sketch of the (a) two- and the (b) four-terminal configuration used to measure the resistances of the PPy films. In the two-terminal configuration the current source and the voltmeter are connected upon the same contacts. In the four-terminal the voltage (V_{4p}) is measured at the contacts parallel to those where the current is applied.*

$$\rho_{4p} = \frac{R_{4p}\,A}{L} = \frac{V_{4p}}{I}\,\frac{A}{L} \tag{3.1.2}$$

where I is the constant current, set by the ac voltage (V_{ac}) source and the series resistor R_s, ($I = V_{ac}/R_s$). A is the area perpendicular to the I direction and L is length parallel to I. In the two-terminal configuration the two-probe resistance (R_{2p}) is expressed by

$$R_{2p} = 2R_c + R_{4p} \tag{3.1.3}$$

where R_c is the contact resistance. The method presented to calculate the resistivity is valid only in the case where the four contacts are parallel. For the electrode structure used in this work (see Fig. 2.1), the resistivity must be corrected by a geometric factor obtained from the van der Pauw method [165].

The resistivity calculated by the van der Pauw method is obtained by solving the analytical expression

$$\exp\left[-\frac{\pi d}{\rho_{vp}} R_{mn,op}\right] + \exp\left[-\frac{\pi d}{\rho_{vp}} R_{no,pm}\right] = 1 \tag{3.1.4}$$

where $R_{mn,op} = V_{op}/I_{mn}$ and $R_{no,pm} = V_{pm}/I_{no}$ are the resistances measured at the points indicated in Fig. 3.5. ρ_{vp} is the resistivity measured by the van der Pauw method and d the sample thickness.

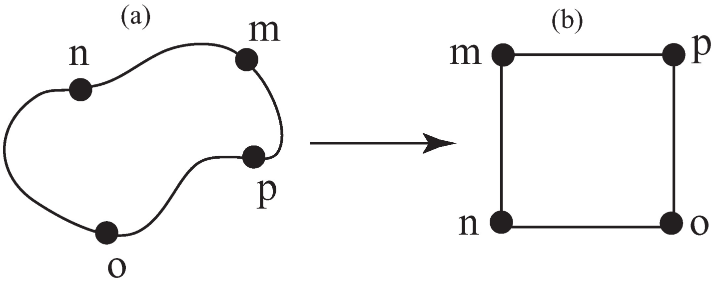

Figure 3.5: *Geometry used to measure the resistivity by the van der Pauw method. A general geometry is presented in the case (a). The case (b) is the one which fits better to the electrode geometry used.*

Taking into account the geometry of the electrodes used to deposit the PPy films, the shape of the surface indicated in Fig. 3.5 (b) represents the best choice. Thus, by considering that $R_{mn,op} = R_{no,pm} = R_{vp}$ in eq. 3.1.4, ρ_{vp} is expressed by

$$\rho_{vp} = \frac{\pi d R_{vp}}{\ln 2} \tag{3.1.5}$$

By dividing eq. 3.1.2 by 3.1.5, the PPy resistivity ρ_{PPy} can be calculated using

$$\rho_{PPy} = \rho_{vp} \cong 4.53\,\rho_{4p} \tag{3.1.6}$$

3.1.4 Frequency dependence of the impedance

Analyzing the frequency dependent capacitance C(f) of the samples allows us to draw conclusions about the evolution of the density of mobile charges. The frequency dependence of the impedance was measured at temperatures of 300 K and 77 K (by using liquid nitrogen), in a frequency range between 10 Hz and 100 kHz using a lock-in amplifier Stanford Research Systems SR830. The measurements were carried using the two-terminal configuration in order to get the information about the interface Pt/PPy. The sketch of the setup used as well as the equivalent circuit are shown in Fig. 3.6. In the equivalent circuit, C_c is the capacitance of the contact Pt/PPy.

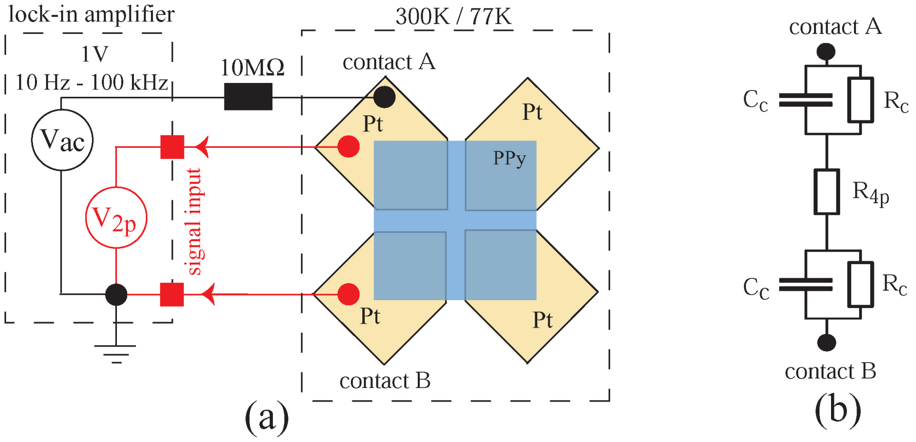

Figure 3.6: *(a) Sketch of the setup used to measure the frequency dependence of the impedance. The sample was measured at 300*K *and 77*K*, in a frequency range between 10* Hz *and 100*kHz *using a lock-in amplifier Stanford Research Systems SR830. (b) Equivalent circuit of the sample.*

In Fig. 3.7, a typical result for the impedance Z(f) is reproduced.

Re(Z) drops markedly around f = 30 kHz, while Im(Z) shows a minimum around 80 kHz. These data are interpreted in terms of the equivalent circuit shown in Fig. 3.6 (b). In the experiment, the voltage of frequency f is applied between contacts A and B, while the current is detected at contact B. The two PPy-Pt contacts are modeled by equal $\mathrm{R_c}$ and $\mathrm{C_c}$, which are a consequence of the interface depletion layer [61].

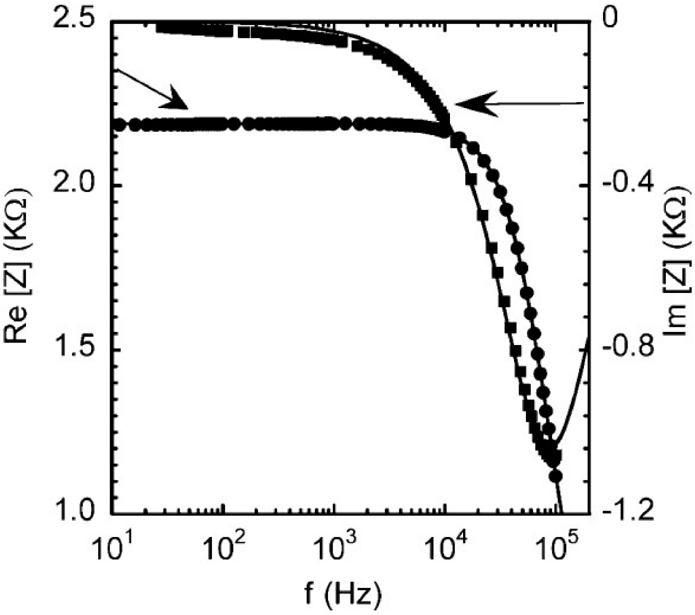

Figure 3.7: *Frequency dependence of the real part (circles) and the imaginary part (squares) of Z(f) at T = 77 K, as measured in a sample grown at 293 K that underwent a single voltammetric cycle. The lines are fits according to the equivalent circuit model (Fig. 3.6 (b)).*

According to this model circuit, the frequency dependence of the impedance components is given by

$$\mathrm{Re(Z(f))} = \frac{2\mathrm{R_c} + \mathrm{R_c}^2\mathrm{R_{4p}}\pi^2\mathrm{f}^2\mathrm{C_c}^2 + \mathrm{R_{4p}}}{4\mathrm{R_c}^2\pi^2\mathrm{f}^2\mathrm{C_c}^2 + 1} \tag{3.1.7}$$

and

$$\mathrm{Im(Z(f))} = -\frac{\mathrm{R_c}^2\pi\mathrm{f}\mathrm{C_c}}{4\mathrm{R_c}^2\pi^2\mathrm{f}^2\mathrm{C_c}^2 + 1} \tag{3.1.8}$$

The resistance of the PPy film itself is $\mathrm{R_{4p}}$ and has been measured independently by four-terminal measurements, which does not show a frequency dependence. Thus, the capacitance and the resistance of the contacts are obtained by fitting the measurements to eqs. 3.1.7 and

3.1.8, using R_c and C_c as fit parameters. The agreement is similar to that one shown in Fig. 3.7 for all samples.

Here the focus is on contact the capacitance per unit area C_c, which is relevant for the analysis. It depends neither on the number of cycles nor on the temperature and equals 1.7 ± 0.2 nF in all samples and at all temperatures. This indicates that the charge density on the polymer chains is independent of the number of cycles as well as of the temperature. Within the Schottky contact model [61], the density of the charge carriers n_{sch} in the semiconductor is given by

$$n_{sch} = \frac{2V_{bi}{C_c}^2}{e\epsilon_0\epsilon_{PPy}} \tag{3.1.9}$$

Here, $C_c = 226 \pm 25\,\mathrm{nF/cm^2}$ in all samples, ϵ_{PPy} is the dielectric constant of the PPy film, and V_{bi} the built-in voltage between Pt and PPy. To estimate n_{sch}, the literature value [146, 166] for $\epsilon_{PPy} = 13.6$ was used, while $V_{bi} \sim 1\,\mathrm{V}$ has been reported [167] for metal-PPy contacts. A value of $n_{sch} = (2.7 \pm 0.4) \times 10^{21}\,\mathrm{cm^{-3}}$ at room temperature is found for all samples. These numbers are in rough agreement with the estimation of the charge deposited during oxidation, as obtained from integration of the oxidation trace of CV (see Fig. 3.1). Here, a charge density of $2.6 \times 10^{21}\,\mathrm{cm^{-3}}$ is found for the first cycle, which decreases to $1.9 \times 10^{21}\,\mathrm{cm^{-3}}$ for the fourth cycle. It is worth noting that the carrier density as obtained from this consideration is not necessarily equal to the density of carriers taking part in transport. Rather, it yields all carriers which become mobile in the strong electric fields present in the contact region. At the much weaker electric fields applied in the bulk, a large fraction of the charge carriers may remain immobile.

3.1.5 Temperature dependence of the resistivity

The measurements as a function of temperature were carried out between 1.6 K and room temperature in an Oxford ^{4}He gas flow cryostat (1.6 – 90 K) equipped with a superconducting magnet (max. field 8 T) and a Linkham nitrogen cryostat (85 – 300 K). Not all samples could be measured down to the lowest temperatures available, either because their resistance increased above the input impedance of the detection circuit (10 MΩ) or because leakage into the silicon substrate became noticeable. The volume of the PPy films was determined from the lateral geometry, in combination with the measurement of the film thickness with an atomic force microscope. The resistivity values were calculated from R_{4p} using the eqs. 3.1.2 and 3.1.6.

The temperature dependence of the resistivity for the samples EG01, EG02 and EG06 is shown in Fig. 3.8. Samples grown at 273 K (EG01 and EG02) have significantly lower resistivities as compared to those grown at 293 K (EG06). Voltammetric cycling increases the resistivity in all samples. However, even after several cycles, the resistivity of a sample polymerized at 273 K remains below that of the one prepared at 293 K that did not undergo CV. This indicates that changes in the growth temperature by 30 K have a stronger influence on the transport properties than CV.

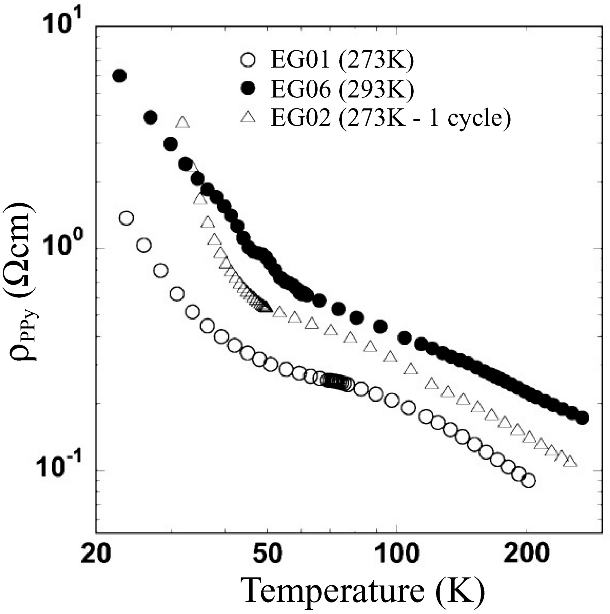

Figure 3.8: *Resistivity vs. temperature for samples grown at* 273 K *(EG01 and EG02) remains below that of films grown at* 293 K *for all temperatures above* 30 K*, even after voltammetric cycling.*

The effect of CV on the PPy conductivity ($\sigma_{PPy} = 1/\,\rho_{PPy}$), which can be quite profound, is evaluated in terms of a phonon assisted transport through a localized system [98, 117]. In Fig. 3.9, the reduced activation energy, W, given by [114, 168],

$$\mathrm{W} = \frac{\mathrm{d}\ln\ \sigma_{\mathrm{PPy}}(\mathrm{T})}{\mathrm{d}\ln\mathrm{T}} \tag{3.1.10}$$

is shown for the 293 K grown sample which did not undergo CV (sample EG06), in comparison to a cycled one (EG07). For $dW/dT > 0$, the system is classified as a metal. For $dW/dT < 0$, the system is an insulator. In the uncycled sample, a positive slope indicates that PPy is in the metallic regime over the whole temperature range, except for $T < 1.9$K, where a strong increase in W is observed. In the cycled sample, the slope is negative at more elevated temperatures, indicating an insulating regime. At temperatures below 10 K, this sample shows a metallic behavior as well. The low temperature anomalies are widely known and attributed to interference corrections [115], which are not investigated here. Hence, the as-grown film is classified as a metal and is transformed into an insulator by a single voltammetric cycle. Further cycling does not change the insulating character.

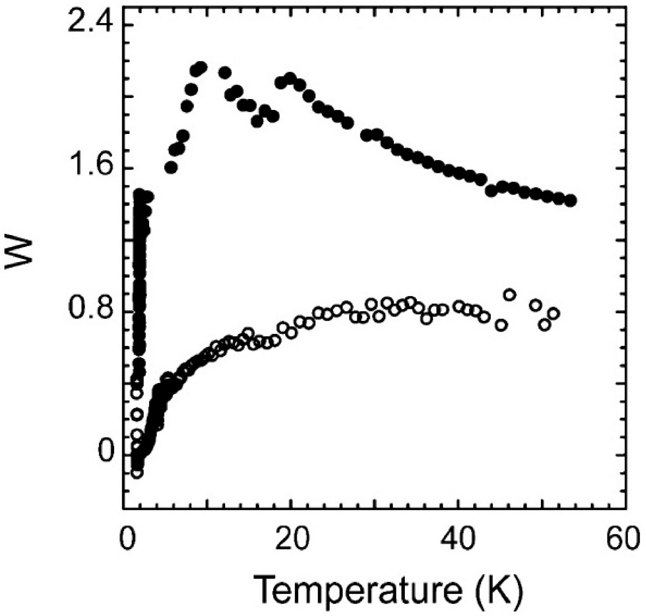

Figure 3.9: (*a) Effect of cycling on the temperature dependence of the reduced activation energy W as observed in an uncycled (open circles, sample EG06) and a cycled (full circles, sample EG07) PPy film.*

This CV-driven metal-insulator transition also manifests itself in the magnetoresistivity $\rho_{\mathrm{PPy}}(\mathrm{B})$ (Fig. 3.10). The resistivity of sample EG06 shows no magnetic field dependence at 2 K, as expected for a carrier system with extended states, for example, within the Drude model [169]. Sample EG07, however, shows a strong, approximately parabolic magnetoresistance. At 8 T, ρ_{PPy} has increased by 30% compared to the value at $\mathrm{B} = 0$. The origin of the parabolic magnetoresistance in strongly disordered media has been discussed already [67]. Basically, within the variable range hopping model, the magnetic confinement adds to the disorder potential and increases the tunnel barriers between the hopping sites.

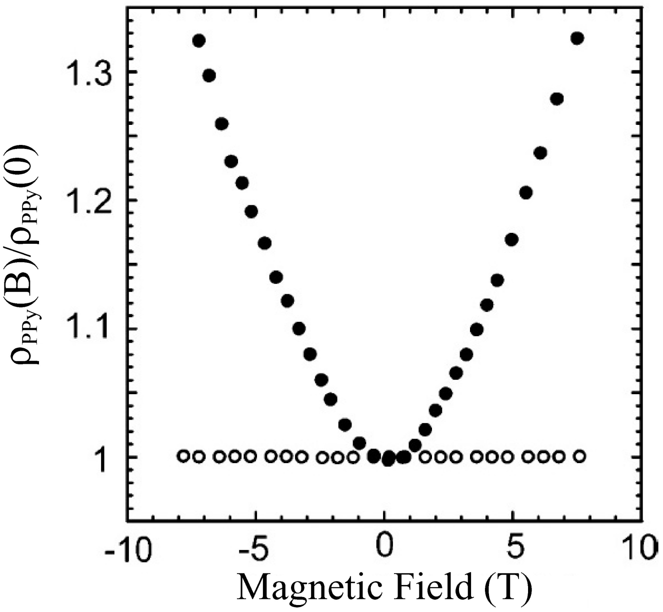

Figure 3.10: *The magnetoresistivities at* $T = 2\,\mathrm{K}$ *with the magnetic field applied perpendicular to the film plane. The uncycled sample (sample EG06) is represented by open circles and the cycled (sample EG07) by full circles.*

From the transport measurements, it is not possible to clarify which of the processes that took place during CV (break/formation of σ-bonds or transformation of PP II into PPy I; for details see Chapter 1) actually caused this transition. However, since the carrier density has remained constant, it is clear that the cycling increases the localization of the electronic states. The localization lengths were extracted by fitting the data to the models appropriate for the corresponding regimes. As discussed in Chapter 1, in the metallic regime (see Fig. 3.11), the temperature dependence can be modeled by a power law dependence,

$$\sigma(T) = \sigma(0) + \alpha\sqrt{T} + \beta T^{p/2} \tag{3.1.11}$$

where the second term on the right-hand side originates from electron-electron interactions, while the third term takes localization effects into account [115, 116, 117]. A fit of the data to eq. 3.1.11 with $\sigma(0)$, α, β, and p as fit parameters is shown by the solid line in Fig. 3.11.

The exponent p is determined as $p = 1.02$. This is reasonable, since $p = 1$ has been predicted theoretically for systems close to the metal-insulator transition [170]. Moreover, a zero temperature conductivity

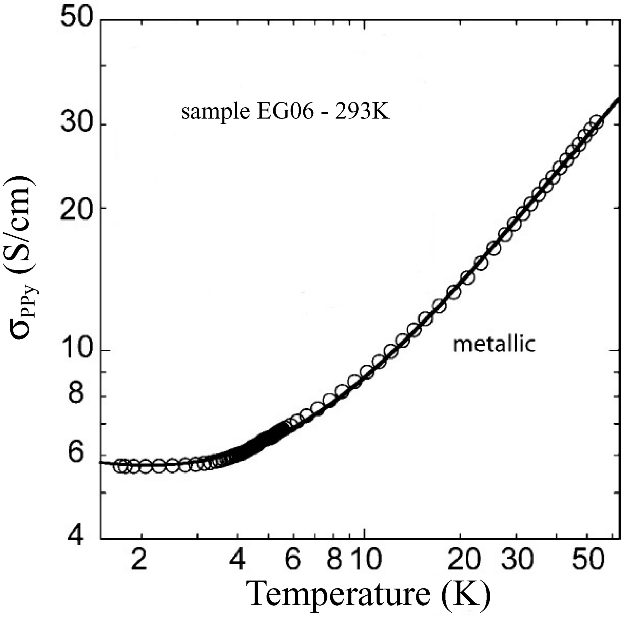

Figure 3.11: *Fits of* $\sigma_{PPy}(T)$ *for the sample EG06 in the metallic regime. The data are represented by the symbols and the fit using eq. 3.1.11 by the solid line. Data values below* 1.9 K *have not been considered.*

of $\sigma(0) = 11.4\,\mathrm{S/cm}$ is found. $\sigma(0)$ is given by [118],

$$\sigma(0) \approx 0.1 \frac{e^2}{\hbar} \frac{1}{L_m} \tag{3.1.12}$$

which allows the estimation of the localization length L_m in the metallic regime to $L_m \cong 21\mathrm{nm}$. This is a surprisingly large number considering the chain lengths of $\sim 12\,\mathrm{nm}$ for PPy I and $\sim 2.95\,\mathrm{nm}$ for PPy II (here, a length of one unit cell of a PPy chain containing two monomers of $0.735\,\mathrm{nm}$ has been assumed [44]). It should be emphasized though, that L_m is not a direct measure of the chain length but rather a characteristic length for the 3D extension of an electronic state that participates in transport. Thus, it is concluded that the relevant electronic states in the metallic regime are extended over several chains.

The 3D VRH model [32, 98] predicts a temperature-dependent conductivity in the insulating regime of

$$\sigma(T) = \frac{\sigma_0}{\sqrt{T}} \exp\left[-\left(\frac{T_0}{T}\right)^{1/4}\right] \tag{3.1.13}$$

Here, the characteristic temperature T_0 is given by

$$T_0 = \frac{16}{k_B N(E_F) {L_c}^3} \tag{3.1.14}$$

where $\mathrm{N(E_F)}$ is the density of states at the Fermi level. To extract $\mathrm{L_c}$, the density of states was assumed to be in agreement with the values reported for PPy in the literature [113, 135], that is, $\mathrm{N(E_F)} = 5 \times 10^{20}\,\mathrm{eV^{-1}cm^{-3}}$. L_c can be determined by fitting the measurements to eqs. 3.1.13 and 3.1.14; see Fig. 3.12.

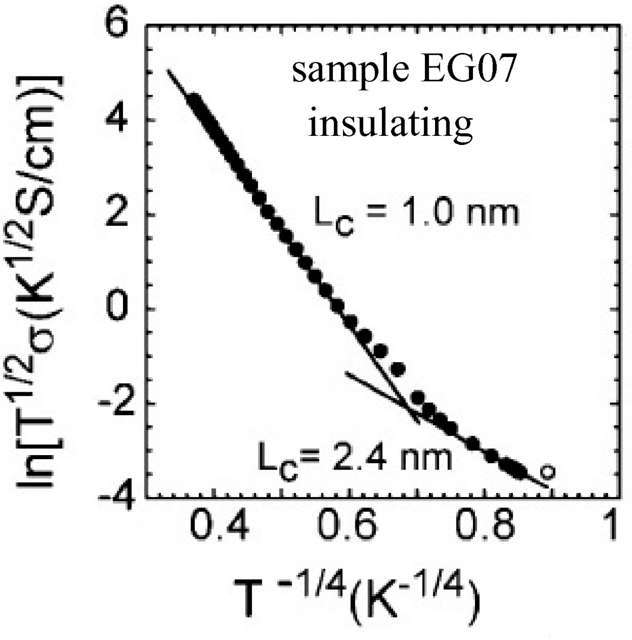

Figure 3.12: *Fits of* $\sigma_{PPy}(T)$ *for the samples EG07 in the insulating regime. The data are represented by the symbols and the fit using eq. 3.1.13 by the solid line. Data values below* 1.9 K *have not been considered.*

In the insulating samples at temperatures above 10 K, $\mathrm{L_c} = 1.0\,\mathrm{nm}$ is found. This indicates that after voltammetric cycling, the charges get localized on a length scale which corresponds to no more than three monomers. Fits to the 1D VRH model are significantly worse, which is taken as a signature that the hopping is 3D in character.

Furthermore, the data were also fitted to an activated transport behavior, $\sigma(T) \propto \exp(-E_a/k_BT)$, where E_a denotes the activation energy. These fits are significantly worse than those shown in Fig. 3.12. This observation leads to the conclusion that transport in the insulating regime does not take place by activation of localized carriers into empty, delocalized states, probably because such states no longer exist in the cycled sample.

Samples grown at 273 K are in the metallic state for temperatures above 40 K, while low-temperature anomalies are found at lower temperatures. Here, the metallic behavior could not be changed by CV, although the resistivity increased somewhat (see Fig. 3.8).

Increasing the growth temperature as well as the first voltammetric cycle decreases the fraction of PPy II in PPy films. Simultaneously, the film resistivity increases. On the other hand, the experimental results show that PPy II consists of significantly shorter chains than PPy I, while the length of PPy I chains increases due to cyclic voltammetry. Therefore, it is concluded that increasing the PPy chain length does not lead to an increase in the conductivity but rather some other mechanism is relevant. The observed increase in resistivity under voltammetric cycling can induce a metal-insulator transition, even though the carrier density is constant. These findings are interpreted in terms of a disorder-dominated behavior. At lower polymerization temperatures, the reaction kinetics is slower, which results in shorter chains, but the film is given more time to form ordered structures, at least on a short range. This reduction of the disorder may be small in absolute terms but nevertheless relevant for the transport properties. Since, according to recent experimental results [119, 120, 121], even in the metallic samples of the highest conductivities generated until now, at least 98% of the charge carriers are localized by disorder and do not contribute to the conductance, a small change in the degree of disorder can cause a dramatic difference in the density of delocalized carriers. The modifications that go along with a single voltammetric cycle can be sufficient to localize all carriers, thus driving the system from the metallic into the insulating phase.

Although a correlation between the PPy II contents and the conductivity was found, this does not necessarily mean that PPy II generates an intrinsically better conducting film than PPy I. It should be emphasized that, beyond the characteristic length scale of localization, the transport measurements do not allow conclusions on the type of disorder introduced. In particular, it is not clear at all which of the mechanisms that takes place during voltammetric cycling is actually responsible for the increased localization. Mechanisms may even be dominant for the disorder which are not relevant for the PPy II-to-PPy I transformation, like, for example, the introduction of oxidative defects. However, the low oxidation potentials as well as the aprotic solvent applied in these studies exclude significant oxidative degradation processes. To give another example, it would be no contradiction to the results presented, if under the conditions favorable for the formation of PPy II, a small amount of very long and highly conductive chains with low disorder were formed as well. To exclude such scenarios, it would be desirable to be able to study the microscopic structure of the films by complementary techniques and correlate them to a conductance on the length scale of individual chains. In particular, the evolution of the morphology of PPy films under cycling has recently been studied in situ by scanning probe techniques [171], with the remarkable result that PPy II forms oriented fibrils with a characteristic size of $20 - 50\,\mathrm{nm}$, while PPy I has a granular structure. When this result is taken into account, it is tempting to attribute the localization length in the metallic sample to the characteristic fibril size.

3.2 Potentiostatically grown films

As discussed in Chapter 1, the polymerization potential is, besides the temperature, a key parameter which determines the properties of PPy films. In addition, it was observed that the samples get worse when the polymerization potential increases above a critical value ($\sim 0.80\,\mathrm{V}$): effects such as film swelling and loss of adhesion to the electrodes are connected to these high polymerization potentials.

For this reason, the objective of this section is to investigate the dependence of both the electrochemical and electronic properties of PPy films as a function of the polymerization potential.

3.2.1 Electrochemical characterization

After potentiostatic polymerization at a temperature of 243 K, the samples (EP01 to EP10) were discharged (reduced) and recharged (oxidized) by CV in a monomer-free solution of 0.5 M $LiClO_4$ in PC. The scan rate used was 10 mV/s. PC was chosen as solution because of the indication from the UV-vis experiments that there is a tendency to obtain a polymer with large amount of PPy II structures (see Section 3.1.2). Therefore, PPy films were prepared at low temperatures, low potentials and using PC. Fig. 4.1 shows the cyclic voltammogram of the sample EP02 grown at 0.60 V.

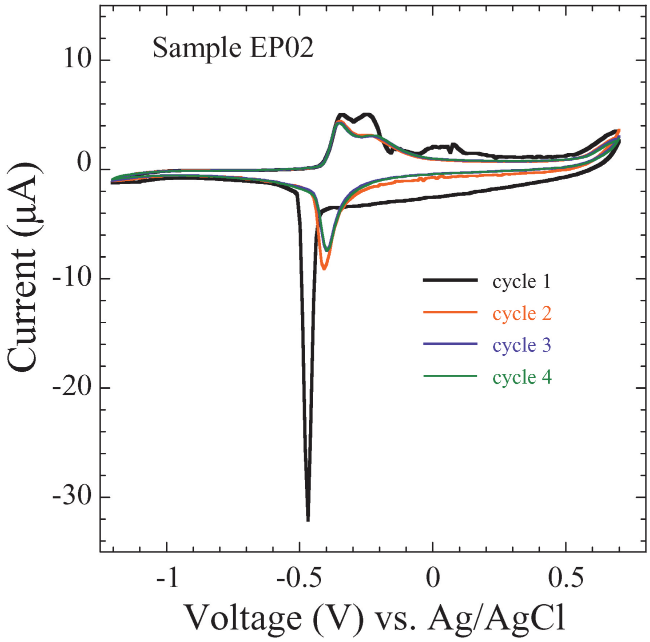

Figure 3.13: *Current-to-voltage characteristics of four consecutive voltammetric cycles for the sample EP02 grown at* 243 K *and* 0.60 V.

In the first cycle the reduction peak appears at −0.47 V, and its value shifts towards the higher potentials by performing the CV. After the third cycle the reduction peak appears at a constant voltage of −0.39 V. In the cycle 1, the oxidation peaks at −0.34 V and −0.24 V indicate the presence of PPy II and PPy I, respectively. A comparatively weaker peak at 0.04 V is attributed to the PPy III [172], whose conductivity was reported to be much lower than those of PPy I and PPy II. The current amplitude of the PPy I peak drops from the first to the second cycle without any observation of an increasing of the PPy II peak. This effect could be explained in terms of an additional increase of the PPy I chain length under cycling. Additionally, to support this point, the peak width increases mostly from cycle 1 to 2. This increase is taken as an indication that the chain length distribution was increased for both species. All the peaks observed during the first oxidation wave change their amplitude strongly in further cycles. However, both peak position and amplitude are constant in cycles following the second one. Thus, the cyclic voltammogram indicates that the sample gets stable over the reduction/oxidation process after the second cycle. This means that over the potential range used for the CV scanning, no transformation of PPy II into PPy I occurs. In addition, it is also possible to consider that a process which forms σ-bonds between chains during oxidation and that breaks during the subsequent reduction step, gets reversible after the second cycle. Another observation is that even preparing films at low temperatures, low V_p and in PC, the presence of PPy I is still not negligible. Indeed, all that can be said is that these contents are smaller than those ones of PPy II.

Fig. 3.14 shows a section of the oxidation wave of the fourth CV cycle for samples grown at potentials between 0.52 V and 1.20 V (Sample EP01 to EP08). The current measured in each wave was normalized to its maximum value.

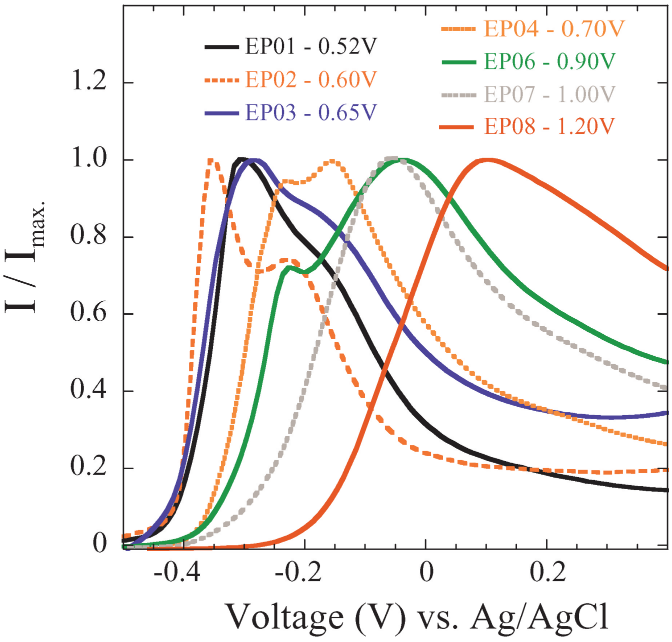

Figure 3.14: *Normalized current vs. voltage for the oxidation wave of the fourth CV cycle for samples grown at potentials between* 0.52 V *and* 1.20 V *(Sample EP01 to EP08).*

From the plots, it is clear that the oxidation potential of the PPy films tends to shift towards more positive values as V_p increases from 0.60 V to 1.20 V. Moreover, the fraction of PPy II increases with decreasing V_p. From Fig. 3.14 it is possible to conclude that, at low polymerization temperatures and using PC as solvent, the amount of both PPy I and PPy II can be adjusted by controlling V_p.

The peak width also tends to become larger as V_p increases. The cyclic voltammogram of the sample grown at 0.52 V indicates the presence of more PPy I than in the sample prepared at 0.60 V, besides the fact that the PPy II oxidation peak is shifted a to more positive value. In order to clarify this point, the analysis of the PPy II oxidation peak position was made for several samples grown at 0.52 V and 0.60 V. The data shows that at both polymerization potentials, the PPy II oxidation peak position showed a deviation of up to ± 7 mV. This deviation is probably due to changes in V_p, caused by inhomogeneities in the electrolyte ionic path at low temperatures. It is worth pointing out that the polymerization under these conditions is close to the limit, namely, for $V_p < 0.52$ V polymerization no longer takes place and the polymerization temperature is close to the freezing point of the electrolyte (235 K).

Fig. 3.15 (a) shows the same type of data as in Fig. 3.14, but for the samples grown between 0.9 V and 1.60 V (Sample EP06 to EP10). The cyclic voltammogram shows that for $V_p > 1.20$ V the PPy oxidation peak begins to shift back towards lower potentials. Additionally, the peak width decreases with increasing V_p. For samples prepared between 0.9 V and 1.40 V, it is simple to identify whether the observed peak is due to the oxidation of PPy I or PPy II. At 0.9 V, both PPy I and PPy II are present. By increasing the potential up to 1.20 V more PPy I is formed than PPy II. But above 1.20 V, the characterization of the peak must be made carefully. Fig. 3.15 (b) presents a section of the oxidation wave of the sample prepared at 1.40 V (EP09). Besides the PPy I oxidation peak clearly visualized at 0.08 V, there is a weak signal of a PPy II oxidation peak at −0.17 V. Moreover, the current increases with the number of cycles over the whole voltage range. This could be an indication that the polymer volume increases by absorbing solvent during the cycling. However, both oxidation peaks are more pronounced after the CV cycles. In Fig. 3.15 (c) a section of the oxidation wave is presented for the samples EP10 grown at 1.60 V. This film shows a very sharp oxidation peak at −0.16 V which was shifted to −0.17 V after cycling and which can be attributed to the oxidation

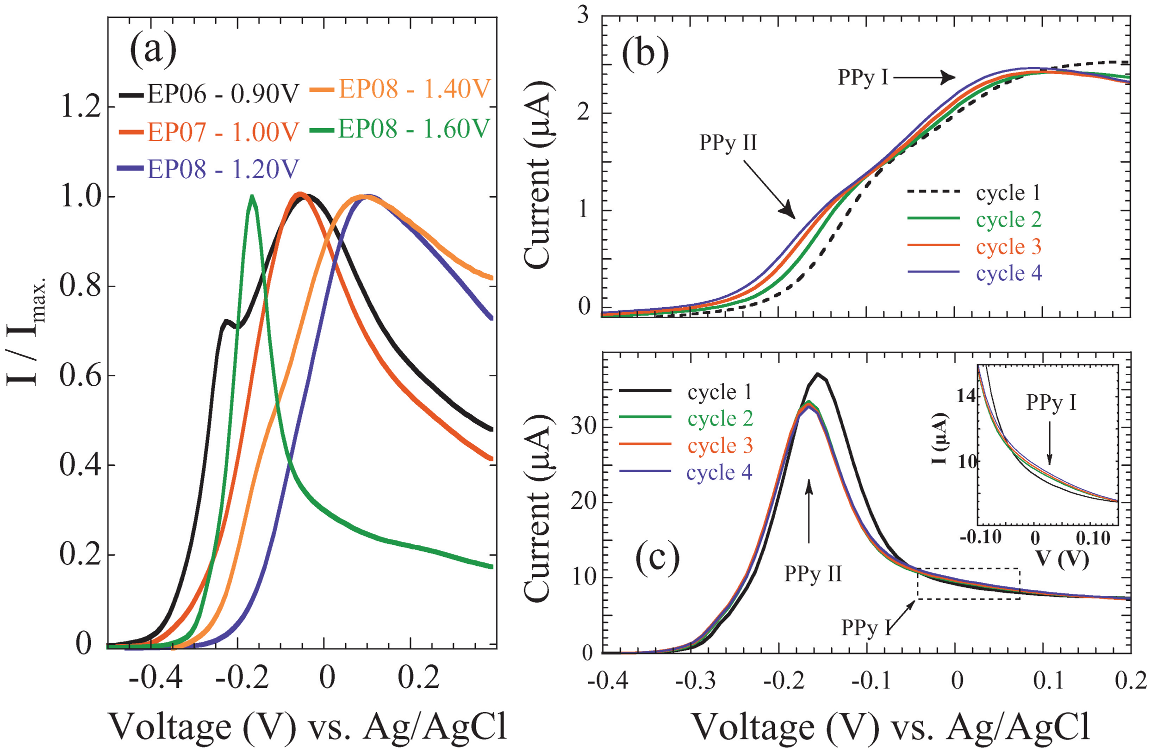

Figure 3.15: *(a) Normalized current vs. voltage for the oxidation wave of the fourth CV cycle for the samples grown between* 0.9 V *and* 1.60 V *(Sample EP06 to EP10). (b) Section of the oxidation wave of the sample prepared at* 1.40 V *(EP09). (c) Section of the cyclic voltammogram of the samples EP10 grown at* 1.60 V*. (inset) Zoom-in onto the region of interest.*

of the PPy II species. By analyzing the zoom-in of Fig. 3.15 (c) (see inset), it is observed that around 0.10 V a slight change is observed. Finally, by comparing the peaks position of this sample with those of the sample EP09, one can verify the they coincide.

Therefore, the fraction of PPy II tends to decrease as V_p increases from 0.52 V up to 1.20 V, where the amount of PPy I is maximum. Above 1.20 V, the fraction of PPy I begins to decrease and at 1.60 V the content of PPy II is higher than that one of PPy I.

3.2.2 Temperature dependence of the conductivity

The samples prepared for the electronic characterization (EP11 to EP20) were synthesized at the same potentials and temperature that those used for CV. The details of the fabrication are described in the Chapter

2 and listed in Appendix A. The resistances were obtained by a standard four-terminal technique as described before (see Section 3.1.3). The measurements as a function of temperature were carried out between 85 K and 300 K in an Linkham nitrogen cryostat. The volume of the PPy films was determined from the lateral geometry, in combination with the measurement of the film thickness with an atomic force microscope. The conductivity values σ_{PPy} were calculated from the $\mathrm{R}_{4\mathrm{p}}$ using $\sigma_{\mathrm{PPy}} = 1/\,\rho_{\mathrm{PPy}}$, and the eqs. 3.1.2 and 3.1.6.

Fig. 3.16 (a) shows the sample conductivity at 300 K as a function of V_{p}.

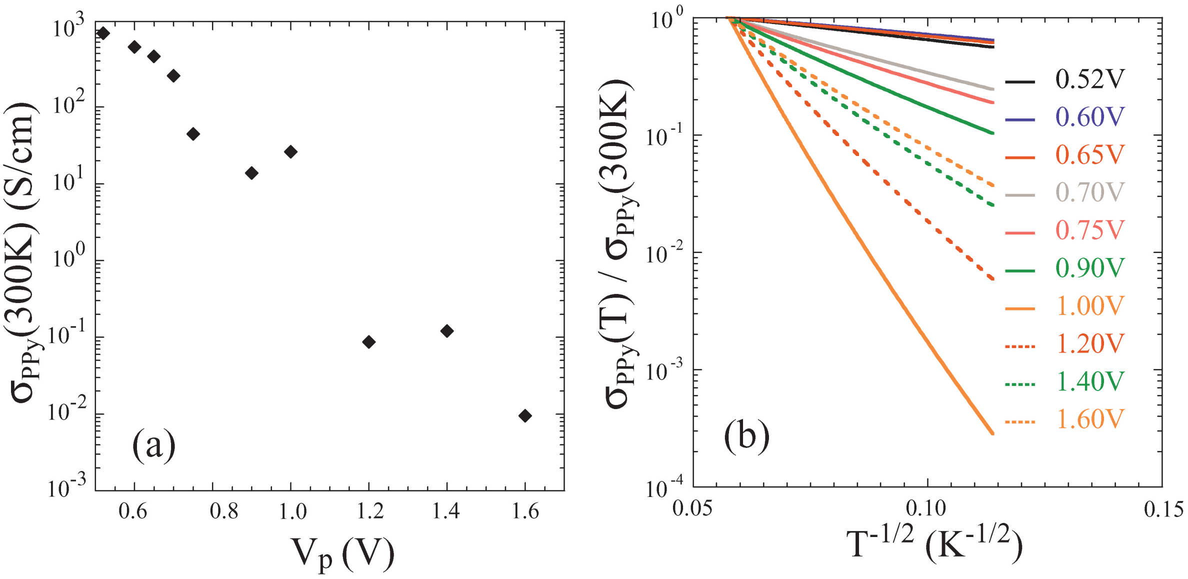

Figure 3.16: *Conductivity of the samples (EP11-EP20) at* 300 K *as a function of* V_{p}. *(b) Temperature dependence of the normalized conductivity for the same samples.*

It was found that the conductivity gets lower as the polymerization potential V_{p} is increased from 0.52 V to 1.60 V. Therefore, by just evaluating $\sigma_{\mathrm{PPy}}(300\,\mathrm{K})$ as a function of V_{p}, one can conclude that there is no clear dependence of the electronic properties of the PPy film on the composition of the film. As observed in the previous section (3.2.1), the fraction of PPy I has a maximum at 1.20 V.

The temperature dependence of the normalized conductivity also changes by varying V_{p} (see Fig. 3.16 (b)). It shows a marked change around $\mathrm{V}_{\mathrm{p}} = 1.00\,\mathrm{V}$. At this potential, the temperature dependence is maximal and decreases for both smaller and larger values of V_{p}, which is roughly in agreement with the CV data which indicates the increasing of the PPy II content above $V_p = 1.20\,V$.

In contrast to the galvanostatically grown samples, in which the temperature dependence of the conductivity in the insulating regime is explained by the 3D VRH, in the potentiostatically grown samples, the temperature dependence is best fitted by ES-VRH (eq. 1.3.5, pg. 20) [99, 100]. Here, the fit correlation is significantly better as compared to Arrhenius type activation and to 3D VRH (eq. 1.3.3, pg. 19).

Fig. 3.17 shows the dependence of ξ, obtained by fitting the data in Fig. 3.16 with eqs. 1.3.3 and 1.3.6 and by using the literature value for $\epsilon_{PPy} = 13.6$ [146, 166], on V_p. By comparing the electronic transport results with the information obtained from CV, it is possible to correlate the amount of PPy I and PPy II to ξ. Between 0.60 V and 1.00 V, the increase of the PPy I fraction is related to the decrease of ξ. Above $V_p = 1.00\,V$ the amount of PPy II increases while ξ gets larger. On the other hand, the conductivity at 300 K does not follow the dependence with the amount of PPy I and II. These results show that the relationship between chain length and conductivity in the potentiostatically grown PPy films is still not clear, even with the evidence that ξ is somehow correlated to the chain length.

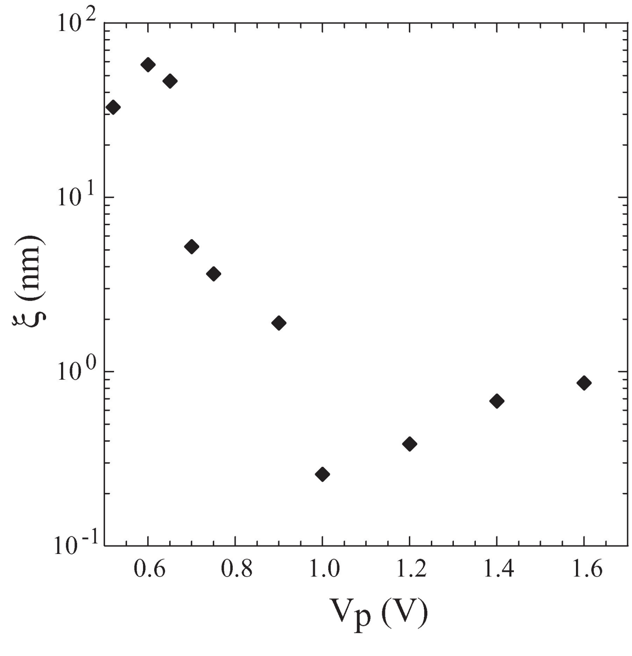

Figure 3.17: ξ *vs.* V_p *for the samples EP11 to EP20.*

3.2.3 Recharge process

The samples grown close to the polymerization limit exhibit both the highest conductivity and localization length (see Fig. 3.16 (a) and 3.17 (a), respectively). In order to investigate the possibility of increasing the conductivity by rising the doping concentration, a set of samples with a high amount of PPy II was synthesized at a temperature of 243 K under $\mathrm{V_p} = 0.52\,\mathrm{V}$. After that, the samples were exposed to a recharging potential $\mathrm{V_r}$ for 5 minutes, and the current was measured. The charging current shows an exponential drop over time. By integrating the current over time and dividing the value by the volume of the film, the embedded charge density is determined. Fig. 3.18 (a) shows the charge density embedded as a function of $\mathrm{V_r}$.

The conductivity of the films recharged at both $\mathrm{V_r} = 0.65\,\mathrm{V}$ and $\mathrm{V_r} = 0.70\,\mathrm{V}$ decreased as compared to the as-grown film, while that one exposed to $\mathrm{V_r} = 0.60\,\mathrm{V}$ increased by roughly a factor of 2 at 300 K (see the inset of Fig. 3.18 (a)). In addition, it was found that the temperature dependence of the conductivity of the as-grown films can be modified by exposing them to $\mathrm{V_r}$ (Fig. 3.18 (b)).

All films exposed to $\mathrm{V_r}$ have in common that the temperature dependence of their conductivity is reduced as compared to the pristine film. Therefore, it is concluded that the conductivity of the film is a monotonously increasing function of the charge embedded, which itself shows a maximum around a charging potential of $\mathrm{V_r} = 0.60\,\mathrm{V}$, which is different from the synthesis potential. Therefore, it was also possible to improve the conductivity of an as-grown film by exposing it to an extra charge potential $\mathrm{V_r}$. Consequently, it was found that the synthesized films are not always "fully charged".

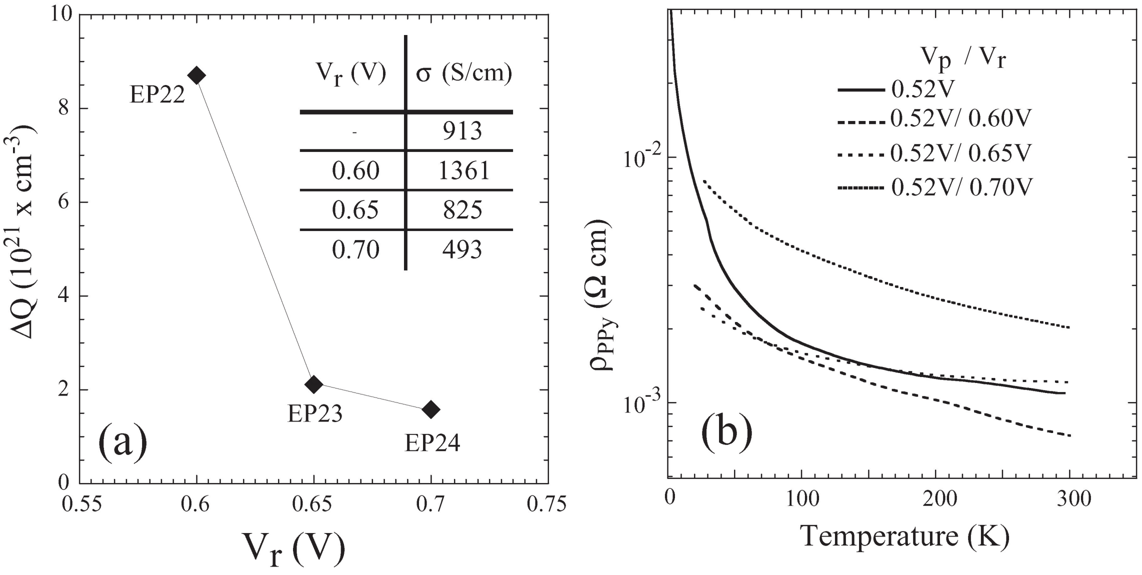

Figure 3.18: *(a) Charge embedded in the film during the recharge process as a function of* $\mathrm{V_r}$*. (inset) Values of the conductivity at* 300 K *after recharge. (b) Temperature dependence of the resistivity for the samples EP21, EP22, EP23 and EP24.*

Chapter 4

Characterization of the films synthesized chemically from vapor

Once the challenge to get PPy thin films patterned was met as described in Chapter 2, the electrochemical characteristics and mainly the electronic properties of those films prepared by vapor-phase polymerization have been investigated, before their potential regarding devices applications is considered in Chapter 5.

Films with thicknesses between 6 nm and 170 nm were investigated. These films exhibit similar electrochemical characteristics than those prepared electrochemically. Nevertheless, the electronic transport in such films revel a system where Coulomb interactions play an important role in determining the properties of the polymer. The electronic transport in electrochemically grown films is better described by 3D VRH and ES-VRH, respectively. However, in the vapor-phase grown films, the presence of a hard gap in the density of states, which is detected by the measurements, indicates that these PPy thin films behave as granular electronic systems. The analysis of the temperature dependence of the differential conductance gives information about the intergrain barrier and indicates that the electric field seems to change the electronic properties of the system. This is supported by magnetoconductance measurements.

4.1 Electrochemical characterization

CV was performed in a solution of 0.1 M of $LiClO_4$ in PC at a scan rate of 10 mV/s. Note that the films get doped only during the chemical polymerization step (see Chapter 2). Fig. 4.1 presents the cyclic voltammogram of the sample VPH06, grown at 293 K.

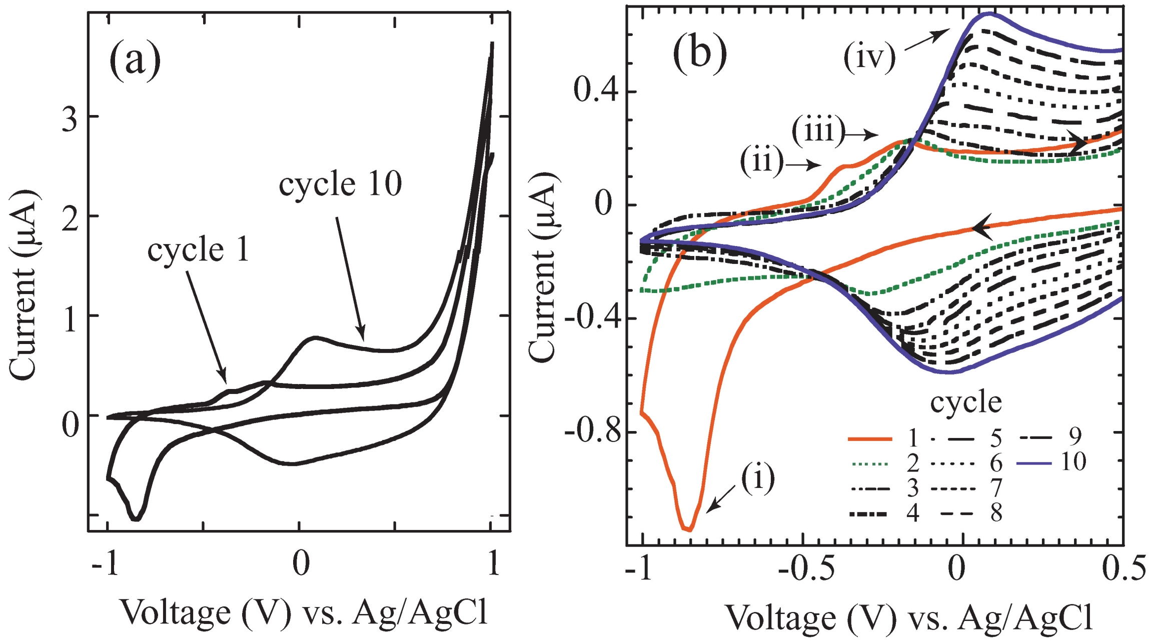

Figure 4.1: *The cyclic voltammetry traces of the sample VPH06, grown at* 293 K*, performed at room temperature. (a) The first and last cycles. (b) Zoom-in in (a) showing the 10 cycles.*

The first CV loop (scan 1) in Fig. 4.1 (a) clearly shows the presence of the two types of PPy (for details see Chapter 3). In the first CV loop (see Fig. 4.1 (b)), a pronounced reduction peak at -0.88 V against Ag/AgCl is observed [peak (i)]. In accordance with more detailed quartz microbalance measurements on other polymers, this peak is interpreted as a transition from predominantly removing Cl^- ions from the film at larger voltages to predominantly inserting Li^+ ions at more negative voltages [87]. The oxidation peak at -0.42 V [peak (ii)] indicates the presence of PPy II, while the peak at -0.23 V [(peak (iii)] is characteristic for PPy I. After the first reduction scan, ${ClO_4}^-$ instead of Cl^- is inserted. Here is worth to remember, from the sample preparation chapter, that Cl^- is the counter ion (e.g., the equivalent of an acceptor) required for charge neutrality, which is embedded into the film during synthesis. Furthermore, as the number of CV cycles is increased, the oxidation peak shifts towards more positive voltages (peak

(iv) in Fig. 4.1 (b)). This behavior is again interpreted as a signature of a transformation of PPy II into PPy I (see section 3.2.1, Chapter 3)[87]. The cyclic voltammograms presented in Fig. 4.1 are very similar to those on PPy films chemically synthesized in H_2O_2 : HCl [72] and it is concluded that the PPy thin films patterned are of comparable order and monodispersity.

Films grown at low temperatures (between 280 K and 293 K) show qualitatively the same behavior than sample VPH06, namely, the presence of PPy I and II in the first scan with the transformation of PPy II in PPy I by cycling. In contrast to the electrochemically grown samples, no systematic dependence of the oxidation and reduction potentials with the changes in the growth temperature was observed. However, it is worth mentioning that the synthesis temperature in the vapor-phase polymerization was varied by 13 K, while the structural modifications observed in electrochemically grown films was reached by changing the synthesis temperature by $\sim 20 - 30\,\mathrm{K}$.

4.2 Electronic characterization

4.2.1 Conductivity measurement setup

The conductivity of the vapor-phase grown samples was obtained by measuring the four-probe resistance, as already discussed in the Chapter 3. In contrast to the structure used for electrochemical deposition, in which a correction was necessary to the van der Pauw geometry, the substrate employed to the vapor-phase polymerization allows the direct measurement of $\mathrm{R_{4p}}$ without corrections. Fig. 4.2 shows a sketch of the four-terminal configuration used.

The film conductivity (σ_{4p}) was obtained from the four-probe resistance $\mathrm{R_{4p}}$ by

$$\sigma_{\mathrm{4p}} = \frac{1}{\rho_{\mathrm{4p}}} = \frac{\mathrm{L}}{\mathrm{R_{4p\,A}}} = \frac{\mathrm{I}}{\mathrm{V_{4p}}}\frac{\mathrm{L}}{\mathrm{A}} \tag{4.2.1}$$

where I is the fixed current, set by the voltage source and the series resistor $\mathrm{R_s}$, ($\mathrm{I} = \mathrm{V}/\mathrm{R_s}$). L is the length parallel to the current direction and A is the area perpendicular to I. The value of A was calculated by

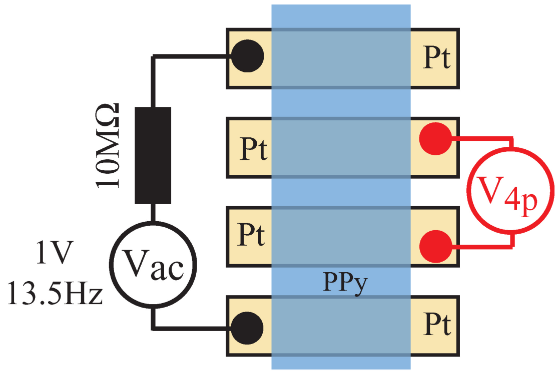

Figure 4.2: *Sketch of the four-terminal configuration used to measure the resistances of the PPy thin films deposited by vapor-phase.*

the product of the stripe line width by the film thickness, which was measured by AFM.

Fig. 4.3 shows the thickness dependence of the conductivity for samples prepared under the same polymerization conditions than sample VPH06, with the exception of the polymerization time, that was changed in order to vary the film thickness. The conductivity was found

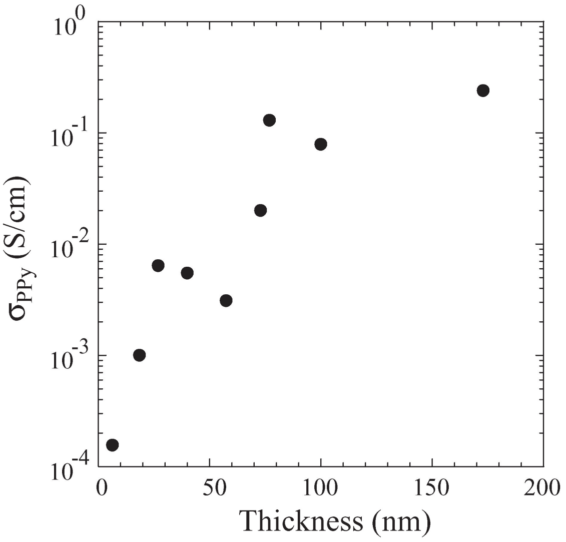

Figure 4.3: *Thickness dependence of the conductivity.*

to be strongly depending on the film thickness from 6 nm up to 100 nm, with an increase of about 3 orders of magnitude. Above 100 nm, the conductivity changes its dependence with the film thickness but without a clear indication of a constant value. Kim and coworkers [77] also reported the same kind of dependence in Fe(III) oxidized PPy films. In addition, they observed that above 600 nm the conductivity became independent of the film thickness.

This thickness dependence of the conductivity was not observed in the electrochemically grown films (Chapter 3), whose films were thicker than 500 nm. However, by comparing the films prepared by both methods, chemical and electrochemical, one can verify from the electrochemical characterization that the amount of PPy I and II is equivalent. Therefore, such a dependence is probably more related to the way that the chains are organized than to their chain length. The surface morphology, analyzed by AFM, shows that thin vapor-phase films have a granular structure, with a egg-like shape and which the size depends on the film thickness (see Chapter 2). On the other hand, thicker electrochemically grown films look like a package of fibers, similar to the PPy *film A*, that grows on top of the droplet of $H_2O_2 : HCl$ during the vapor-phase polymerization (see Fig. 2.15 (b) in Chapter 2).

By using the two-terminal configuration, R_c was evaluated for all the vapor-phase samples fabricated. Samples grown at 293 K show the highest value of R_c. Regardless of the film thickness, these samples presented $0.3\,R_{4p} < R_c < 0.6\,R_{4p}$. This value was reduced to $R_c \sim 0.1R_{4p}$ by using freshly prepared oxidizing solutions. Another way to reduce the contact resistance is performing the synthesis at lower temperatures. Samples such as VPH04 and VPH05 exhibited $R_c < 0.05R_{4p}$. Therefore, a good metal/PPy contact is not reached just by choosing a high work function metal, such as Au and Pt, but also by optimizing the synthesis parameters.

4.2.2 Low temperature measurements

Current-voltage characteristics

For this measurement, samples were prepared by vapor-phase polymerization according to the method described in the Chapter 2. Different films were synthesized at temperatures of 277.5 K, 282 K and 293 K. After growth, two sets of samples were kept under argon atmosphere for 24 hours and for 4 weeks, respectively, prior to the measurements. For details see Appendix A. Fig. 4.4 (a) shows the scanning probe microscope image of the surface morphology of the sample VPH04 (grown at 282 K and kept 4 weeks in argon atmosphere) and the respective four-electrodes device (b). The PPy film covers 4 Pt electrodes (c1 to c4).

The gap between the electrodes is 2 μm and the film width is 60 μm.

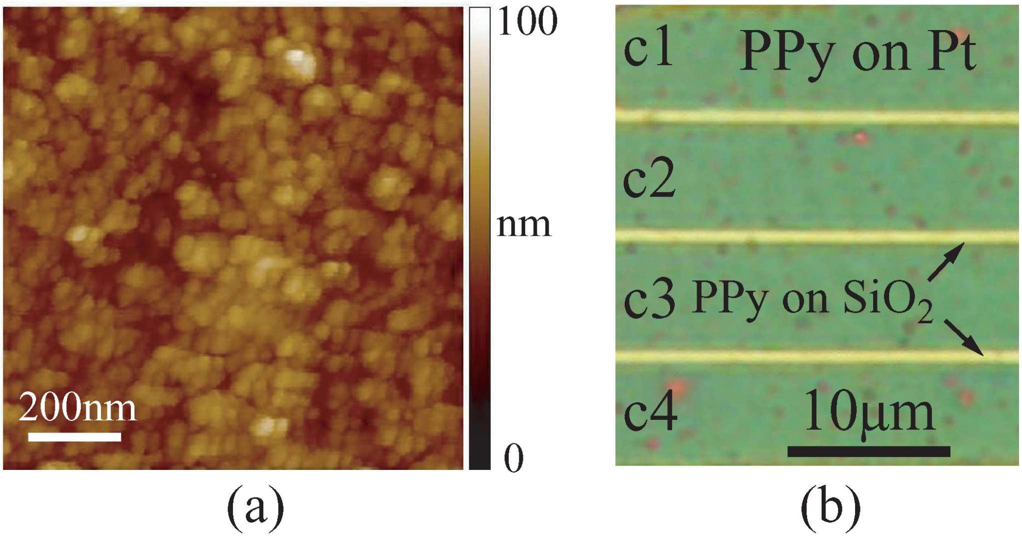

Figure 4.4: *(a) Morphology of the sample VPH04 (grown at* 282 K *and kept 4 weeks under argon atmosphere). (b) Four-electrode device.*

At 300 K, the conductivity is 12 S/cm, 10 S/cm and 8.5 S/cm for samples kept under argon atmosphere during 4 weeks and prepared at 277.5 K (VPH05), 282 K (VPH04) and 293 K (VPH03), respectively. The samples (VPH08-VPH10) that were kept for 24 hours under argon all show the same room temperature conductivity.

The current-voltage (IV) measurement was performed using a four probe geometry, passing a dc current from contact c1 to c4 (ground) and measuring the voltage drop between the contacts c2 and c3. The IV traces were measured for temperatures from 2.1 K to 300 K in an Oxford ^{4}He gas flow cryostat equipped with a superconducting magnet (maximum magnetic field 8 T). Fig. 4.5 shows the nonlinear IV traces as a function of the temperature for sample VPH04. Fig. 4.5 (b) shows a log-log plot of the current as a function of the electric field E for the same data plot in (a). The same nonlinearity is observed for all samples below 90 K and prepared by vapor-phase polymerization. This behavior is not observed in samples prepared by electrochemical methods, which exhibit linear IV traces even at temperatures below 90 K. By comparing two-probe with four-probe measurements, the contact resistances R_c were below $0.1R_{4p}$ for all samples investigated. No hysteresis of the measurement traces was observed under the rate of 1 mV/s.

In addition, a threshold electric field of $E_t = 600$ V/cm at 2.1 K is observed (see Fig. 4.5 (b)), which decreases with increasing temperature and vanishes at 4.6 K. The existence of a threshold electric field

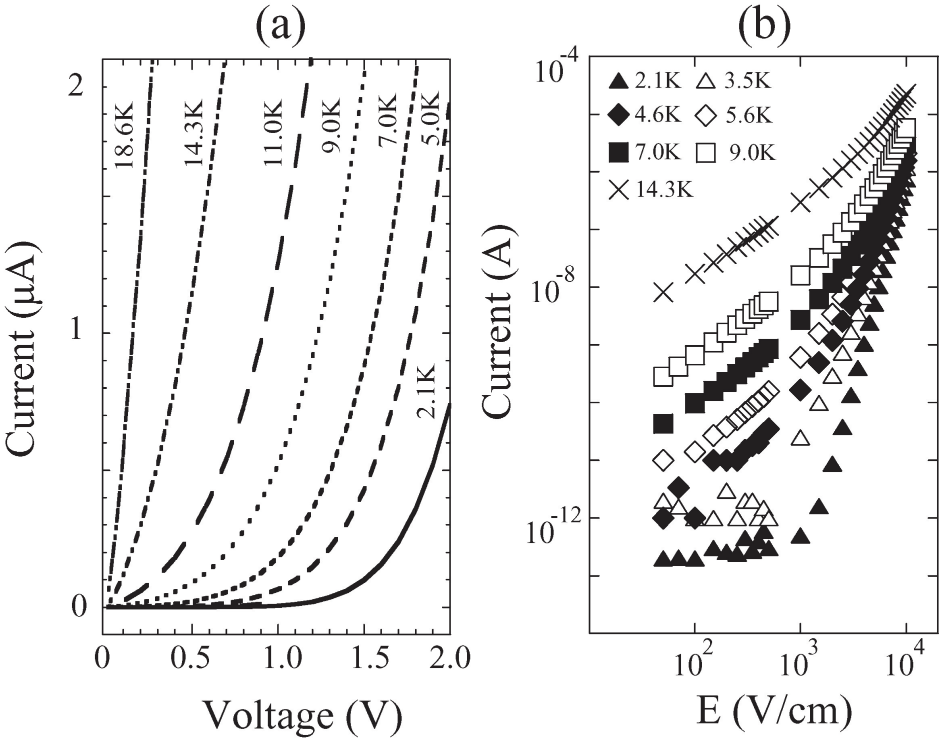

Figure 4.5: *(a) IV characteristics of the samples VPH04 measured at different temperatures. (b) Electric field dependence of the current between* 2.1 K *and* 14.3 K.

is associated with Coulomb blockade transport [102, 103, 104, 105]. In order to transfer charge between conductive islands in the Coulomb blockade transport regime, a Coulomb barrier $E_b = 0.12\,eV \times (2a/\ell)$ at 2.1 K needs to be overcome. Here, $\ell/2a = N$ is the number of islands, with a being the island radius, and $\ell = 2\,\mu m$ denotes the electrodes separation. The Coulomb charging energy E_c is determined by eq. 1.3.7. Using $E_b = E_c$ and $\varepsilon_r = 13.6$ [146, 166] results in $a \approx 30\,nm$, which indicates that one island corresponds to one egg-like structure observed in the morphology (Fig. 4.4 (a)). Therefore, taking into account these results, the PPy thin films behaves like a granular system formed by grains with an egg-like structure, containing many very well interconnected chains (PPy I and II). On the other hand, the grains are weakly coupled between their neighbors. In such a system, the conductivity depends on the properties of the grain and also of the intergrain barrier.

Since the intragrain composition seems not to change with the film thickness (from electrochemical characterization), the dependence of the conductivity with thickness, as observed in Fig. 4.3 can be due to both the grain size and the intergrain coupling. As the film gets thicker, more interconnections are created between separated grains. By increasing the grain size, which is proportional to the film thickness (see Chapter 2), the Coulomb interaction decreases (eq. 1.3.7), leading to an increases of conductivity.

Once the threshold electric field observed in the IV characteristics (Fig. 4.5 (b)) was associated with the Coulomb blockade transport, then the temperature dependence of the conductivity should be described by eq. 1.3.8 [105].

Temperature dependence of conductance

In Fig. 4.6, the differential conductance G(T) is shown for sample VPH04 for various electric fields.

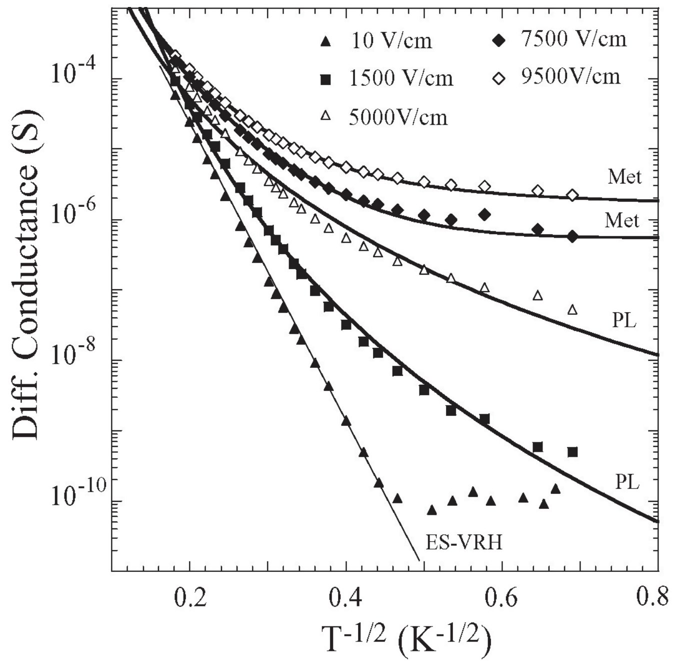

Figure 4.6: *Temperature dependence of the differential conductance* G = dI/dV *for various electric fields* E.

At low electric fields (E = 10 V/cm up to E = 1500 V/cm), G decreases with decreasing temperature following an ES-VRH like dependence [99, 100] instead of an activated transport as shown by eq. 1.3.8. However, as discussed in Chapter 1, the hard gap of the Coulomb blockage excludes the possibility of a soft gap of the ES-VRH. But as described by Zhang [105], a soft gap can be created in the background of density of states near to Fermi level of the hard gap in randomly spread conducting islands, separated by a slightly doped barrier. By adopting this consideration, for $eE\xi \gg k_BT$, the temperature dependence of the differential conductance is given by eqs. 1.3.5 and 1.3.9 [105].

From the low bias measurement at $E = 10\,\mathrm{V/cm}$, T_0 was found to the 235 K, which corresponds to $\xi_\mathrm{g} = \mathrm{a_t r_g/d_g} \approx 14.6\,\mathrm{nm}$. The behavior of G(T) observed for temperatures below 4.6 K at 10 V/cm is a result of $\mathrm{eE}\xi < \mathrm{k_B T}$. In addition, the typical hopping distance, given by the ES-VRH model as

$$r(T) = \left(\frac{e^2\xi}{4\pi\varepsilon_0\varepsilon_r k_B T}\right)^{1/2} \tag{4.2.2}$$

results in $r(2.1\,\mathrm{K}) \approx 93\,\mathrm{nm}$, by considering $\xi = \xi_g$.

From $\mathrm{E} = 1500\,\mathrm{V/cm}$ to $\mathrm{E} = 5000\,\mathrm{V/cm}$, G(T) is better explained by a power law, $\mathrm{G(T)} \propto \mathrm{T}^\gamma$, even though it is still possible to fit the ES-VRH with reasonable agreement, which was evaluated using the linear correlation coefficient (R). R was found to equal 0.99 for the power law and 0.97 for ES-VRH fits. The power law dependence is a characteristic behavior of disordered systems at critical regime, with $0.33 < \gamma < 1$ [173, 174]. From the power law dependence, the fit parameters $\gamma(1500\,\mathrm{V/cm}) = 5.3$ and $\gamma(5000\,\mathrm{V/cm}) = 3.6$ are obtained, which are larger than those observed in other experiments.

At 5000 V/cm and below 6 K ($eE\xi \gg k_bT$), G(T) becomes approximately constant in sample VPH04. Above 5000 V/cm, the Anderson model applied for the metallic regime (Met) in disordered systems was used to fit the temperature dependence at higher electric fields. As described in Chapter 1, in the metallic regime, the temperature dependence of the differential conductivity $\sigma_G(T)$ is modeled by eq. 3.1.11 [107, 115, 116, 168].

Fig. 4.7 (a) shows the reduced activation energy W(T) as a function of temperature for three electric fields. Here, $\mathrm{W(T)} = \mathrm{d(lnG)/d(lnT)}$. The slope of W(T) determines the metallic, critical and insulating regime of the material. According to the definition [168], for 9500 V/cm ($\mathrm{dW/dT} > 0$) the system is in the metallic regime, while for 10 V/cm ($\mathrm{dW/dT} < 0$) the system is insulating. $\mathrm{dW/dT} \simeq 0$ (for 1500 V/cm) indicates that the system is in the critical regime [114, 168].

However, the behavior of G(T) above $\mathrm{E} = 1500\,\mathrm{V/cm}$ can be also attributed to Joule heating instead of electric-field induced metal-insulate transition. The Joule heating in this case occurs at low temperatures

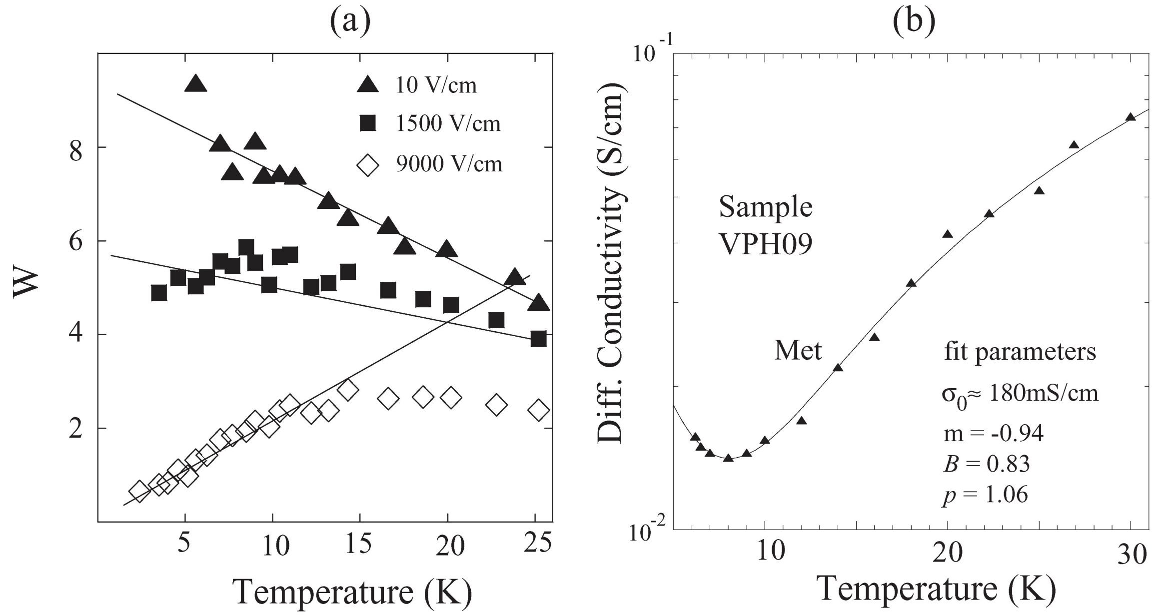

Figure 4.7: *(a) Reduced activation energy for* $E = 10\,\mathrm{V/cm}$*,* $1500\,\mathrm{V/cm}$*, and* $9500\,\mathrm{V/cm}$*. (b) Measurement made on sample VPH09 at* $5000\,\mathrm{V/cm}$*, fit by the Anderson model and with a minimum in the differential conductivity.*

when the electrons take energy from the electric field and phonons are emitted [175]. Consequently, the conductivity tends to saturate.

In contrast with sample VPH04, at 5000 V/cm sample VPH09 (prepared at 282 K and kept 24 hours under argon atmosphere) presents an inversion of the temperature dependence below 8 K (see Fig. 4.7 (b)). The data of sample VPH09 are plotted in terms of the differential conductivity given by $\sigma_\mathrm{G} = \mathrm{GL/A}$. This inversion of $\sigma_\mathrm{G}(\mathrm{T})$ could excludes the possibility of Joule heating. On the other hand, this minimum does not really prove the existence of a metal-insulator transition driven by the electric field, when intragrain transport is assumed [175]. According to Beloborodov and coworkers [107], the conductance in a granular system is due to both the intergranular and intragrain conductances. The intergranular one is much smaller than the intragrain, and is due to tunneling through the barrier separating the grains. Both conductances have their own temperature dependence. Most of the temperature dependence of the differential conductance observed in Fig. 4.6 is due to the intergranular transport. However, if the grain becomes larger, the temperature dependence of the intragrain resistance may also influence in the transport, for instance, leading to the inversion of the dependence of $\sigma_\mathrm{G}(\mathrm{T})$, as observed in Fig. 4.7 (b). But since this trace was a single observation, more experiments are necessary to decide whether either Joule heating or intragrain conductance are relevant.

All samples show a crossover from ES-VRH to an Arrhenius behavior ($G(T) \propto \exp(-U/k_BT)$) at temperatures $\mathrm{T_{cross}} = 25 - 30\,\mathrm{K}$. Fig. 4.8 (a) shows $\sigma_G(T)$ vs. T for sample VPH10, grown at 277.5 K and and kept under argon atmosphere for 24 hours. The activation energy U of sample VPH10 decreases as the electric field increases, changing from ≈ 9 meV at 10 V/cm to 5.5 meV at 5000 V/cm. $\mathrm{E_{dis}} = \mathrm{k_B T_{cross}}$ is interpreted as a characteristic disorder energy which indicates the point where the system crosses from activated to ES-VRH like transport. For sample VPH010, $\mathrm{E_{dis}} = 2.5\,\mathrm{meV}$. A similar behavior has been recently reported in experiments on gold nanoparticle multilayers and thick films [106].

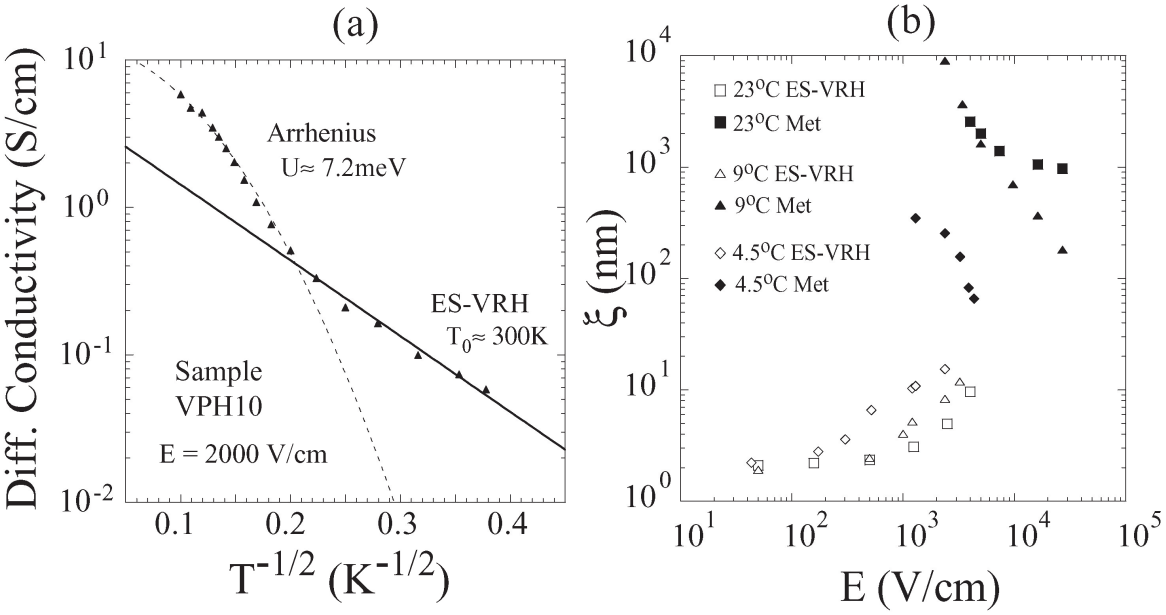

Figure 4.8: *(a) Fits of the experimental data (taken on sample VPH10, grown at* 277.5 K *and and kept under argon atmosphere for 24 hours) to the ES-VRH at low temperatures and to activated transport at temperatures above* 30 K*. (b) Behavior of the correlation length as a function of the* E*, as obtained from fits to ES-VRH in the insulating regime, as well as to the Anderson metal in the metallic like regime.*

As described above, the correlation length can be extracted from the data for both high and low electric fields. Fig. 4.8 (b) presents the localization length as a function of the electric field, as found in the samples grown at 277.5 K (VPH10), 282 K (VPH09) and 293 K (VPH08) and kept under argon atmosphere for 24 hours.

On the insulating side, the ES-VRH was used to fit the data while on the metallic-like side, the Anderson formalism (eq. 3.1.11) has been applied. Even though the data vary strongly from sample to sample, two observations can be made: first of all, the correlation length on the metallic-like side is significantly larger as compared to that one found on the insulating side. Second, there is a tendency for the correlation length to diverge at the critical point.

The localization length for a granular system is given by $\xi_{\mathrm{g}} = \mathrm{a_t r_g/d_g}$ [105, 108], where $\mathrm{d_g}$ and $\mathrm{r_g}$ are the tunneling barrier width between two grains and the grain radius, respectively, while a_t is the tunneling decay length in the insulator. Since $\mathrm{d_g}$ and $\mathrm{r_g}$ are constants, the electric-field dependence of $\xi = \xi_{\mathrm{g}}$ actually describes how the wave function decays inside the barrier as a function of E. As E increases, higher is the probability of tunneling through the barrier.

Electric-field dependence of conductance

According to [105], at high electric fields, the differential conductance G(E) also behaves according to Efros-Shklovskii variable-range hopping (ES-VRH)[176, 177]

$$G(E) \propto \exp(-\sqrt{E_0/E}) \tag{4.2.3}$$

where $\mathrm{E_0 = k_B T_0/2e\xi_{ES}}$ and ξ_{ES} is the localization length [178]. In Fig. 4.9 the differential conductance G is plotted against $E^{-1/2}$ for temperatures between 2.1 K and 18.6 K. The data presented could not be fitted by eq. 4.2.3. Possibly, the electric field was not high enough.

Magnetoconductance

The magnetoconductance was determined from IV measurements at 2.1 K for magnetic fields ranging from −8 T to 8 T. In Fig. 4.10 (a), the differential conductance as a function of a magnetic field G(B), normalized to its value at B = 0, is shown for sample VPH04, for electric fields of 2500 V/cm and 9500 V/cm . Apparently, the external magnetic field tends to localize the charge carriers. In the metallic regime, this effect is a consequence of electron-electron interactions and arises from the Zeeman splitting between spin-up and spin-down electrons [114]. The

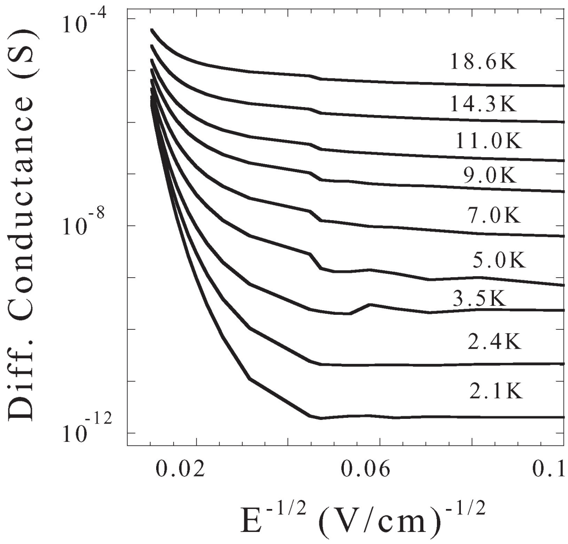

Figure 4.9: *Differential conductance* G *vs.* $E^{-1/2}$.

data follow the dependence $G \propto B^2$ up to 3.5 T where $g\mu_B B \ll k_B T$ and $G \propto B^{1/2}$ at larger magnetic fields, where $g\mu_B B \gg k_B T$ [179, 180].

Fig. 4.10 (b) shows how $G(B) = [G(8T) - G(0)]/G(0)$ changes as function of the electric field. The larger the electric field, the harder it is for the magnetic field localize the carriers.

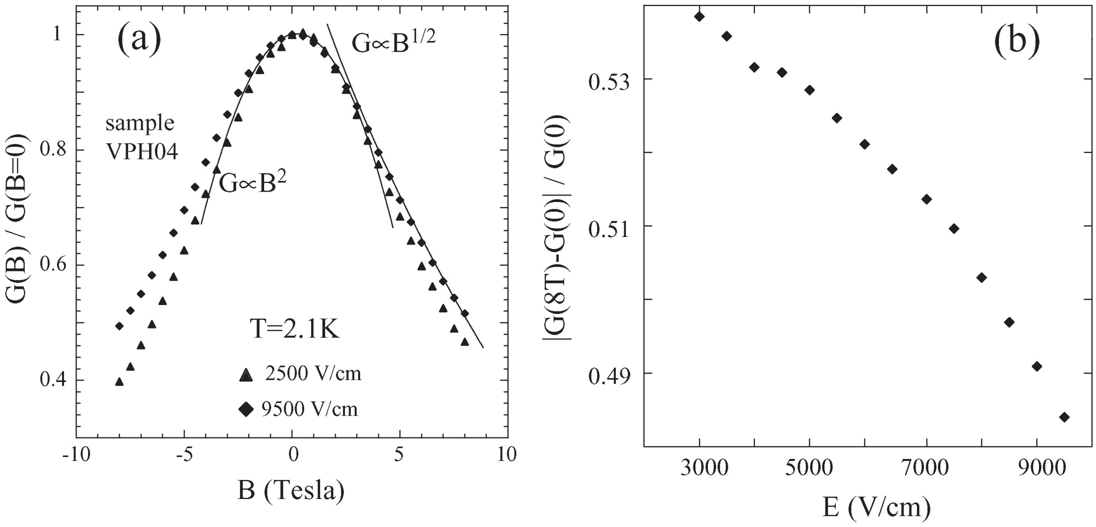

Figure 4.10: *(a) Differential magnetoconductance for intermediate and strong electric fields (symbols). The full lines are fits to the low- and high field regime, see text. (b) Normalized differential conductance as a function oft the electric field.*

Scaling

By assuming that the electric field induced metal-insulator transition occurs and can be mapped onto an equilibrium phase transition, it should be scalable, even though the scaling law is unknown. As a first try, the data presented in Fig. 4.6 cannot be scaled by the conventional scaling applicable for metal insulator transitions as a function of an equilibrium parameter like the carrier density. However, was found a reasonable scaling according to

$$\frac{I}{T^{\alpha+1}} \propto \frac{eV}{k_B T} \tag{4.2.4}$$

where I denotes the current, see Fig. 4.11. This scaling law has been derived and applied for excitations in Luttinger liquids [181, 182, 183]. The samples presented are definitely not Luttinger liquids, so the question arises why this scaling law works here. Please note that the strong deviations from this scaling law are exclusively due to the Coulomb blockade transport regime. For sample VPH04 at temperatures between 12K and 32K, it is furthermore also possible to fit the temperature dependence of the conductance at zero bias with a power law ($G_0 \propto T^{\alpha}$) with $R = 0.98$ and $\alpha \approx 6.1$ (inset of Fig. 4.11). Nevertheless, a fit to ES-VRH with a crossover around T = 30 K to Arrhenius provides a significantly better fit.

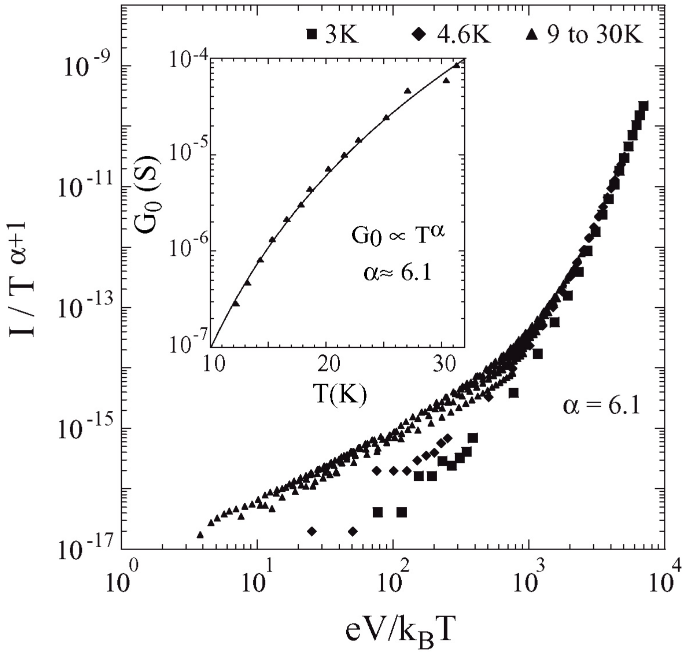

Figure 4.11: *Scaling of the data according to* $I/T^{\alpha+1} \propto eV/k_BT$.

Chapter 5

Polypyrrole devices

The aim of this chapter is to demonstrate that the PPy thin films prepared by vapor-phase polymerization can be used as devices such sensors and transistors.

In the case of sensors, as discussed in Chapter 1, there are several reports in the literature indicating the sensitivity of PPy films to oxygen [41, 56, 151, 152, 153, 154, 155]. Thus, an oxygen sensor, prepared by using the same procedure than sample VPH02 is demonstrated. The main advantage of this sensor is the possibility of patterning by a standard silicon processing. In addition, the thin film thickness (below 50 nm) makes the device respond to oxygen within 2 s.

Besides the application as a sensor, in this chapter it is also demonstrated that a patterned PPy film can be operated as a transistor, which is explained in terms of a Schottky barrier field effect transistor.

5.1 Oxygen gas sensor

In order to fabricate an oxygen gas detector, a thin PPy film was prepared by vapor-phase polymerization as described in Chapter 2. The sensor is formed by two Pt contacts, separated by a 2 μm gap and deposited on a doped-Si/SiO$_2$, and by a 5 μm wide and 40 nm thick PPy stripe line, patterned perpendicular to the Pt contacts (sample VPH07). An image of the device is shown in Fig. 5.1 (a). The sensor was biased with a constant voltage of -1 V while the doped Si back gate was grounded. In order to test the sensitivity to oxygen, the sample was placed in a gas cell (see the schematic diagram in Fig. 5.1 (b)). The cell is formed by a sample chamber where the nitrogen and oxygen gas lines are connected. Both gas pressure and gas flux are controlled during the experiment.

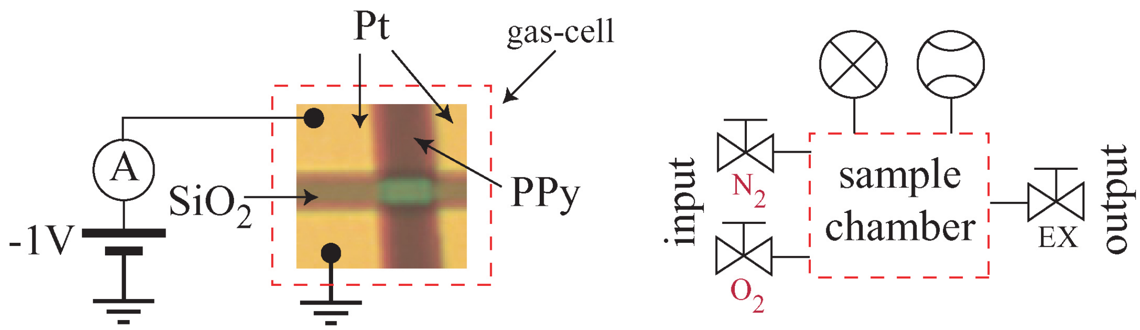

(a) (b)

Figure 5.1: *(a) Image of the oxygen gas sensor. (b) Scheme of the gas cell.*

Fig. 5.2 shows the response of the film to oxygen exposure. Prior to the experiment, the sample was left in a nitrogen atmosphere with 50 mbars overpressure for a few hours. At time "a" in Fig. 5.2, the atmosphere was changed to oxygen (opening O_2 and EX valves in Fig. 5.1 (b)) with 50 mbars overpressure by rinsing with a 0.5 l/h oxygen flux for 5 seconds and subsequent closing of the exhaust line (EX valve). The reverse procedure was performed at time "b" to replace the oxygen by nitrogen. As the oxygen is added (time "a"), the current in the PPy film increases by 6% within 2 s. Afterwards, the current slowly decays

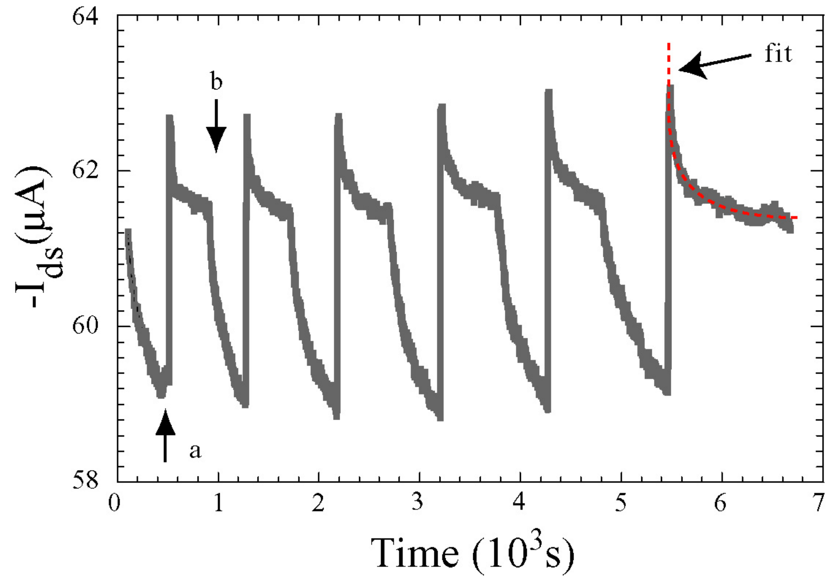

Figure 5.2: *Operation of the PPy film as oxygen detector. The dashed line in the last cycle shows a fit to a stretched exponential decay.*

to a value which remains significantly above that one before oxygen exposure. This decay does not follow a simple exponential law, but can be well described by a stretched exponential (Kohlrausch) law,

$$I(t) = I_0 \exp\left[-\left(\frac{t}{\tau}\right)^{\beta}\right] \tag{5.1.1}$$

which is frequently attributed to diffusion processes in amorphous materials [34, 184]. A typically long time constant of 3.2×10^7s and a value for $\beta = 0.4$ was found, indicating a very slow relaxation process. This behavior is interpreted as follows: immediately after oxygen exposure, the oxygen molecules diffuse into the PPy where they undergo a charge transfer process, act as acceptors and consequently increase the film conductance. On a longer time scale, some oxygen molecules are caught in deep traps or interface states, where they form scattering centers or change the band bending, respectively, thereby reducing the conductance. In the sample, there is a dynamic equilibrium between O_2^- ions and O_2 molecules. As a pure nitrogen atmosphere is offered, neutral oxygen diffuses out of the film, the concentration of O_2^- in the film gets reduced, and the current decreases. The response of the sensor was observed to be independent of the bias voltage, indicating that drift effects are irrelevant.

5.2 Thin-Film Field-Effect Transistor

The same device evaluated as an oxygen sensor (sample VPH07) was used as a transistor as well. Besides VPH07, another 8 samples with film thicknesses ranging from 6 nm to 120 nm have been prepared from oxidizing solutions of identical molarities. Out of these, the four samples with film thicknesses between 22 nm and 50 nm could be operated as transistors, all showing qualitatively identical behavior.

Here, the focus is on the device that was used as oxygen sensor (VPH07). The conductivity of the ungated (p-type) polymer film is $\sigma = 5.5 \times 10^{-3}$ S/cm. In Fig. 5.3, the current-voltage characteristics of the device is shown. The measurements are carried out in a nitrogen atmosphere at room temperature. The upper left inset of Fig. 5.3 shows a sketch of the transistor cross section and its electrical setup. At a drain-source bias voltage of 10 V, a transconductance of 4.8 μS was found. The voltage range is limited by the breakdown voltage of the gate oxide ($\sim 45\,\mathrm{V}$). At positive bias voltages, the onset of saturation is observed at all voltages around a drain-source voltage V_d of 9 V. The current as a function of the gate voltage in the device measured indicates a p-type doping with no signatures of the formation of an inversion layer at high positive gate voltages (lower right inset in Fig. 5.3), when compared with the n-MOSFET described in Chapter 1. In conclusion, inversion has not been established in the PPy transistor.

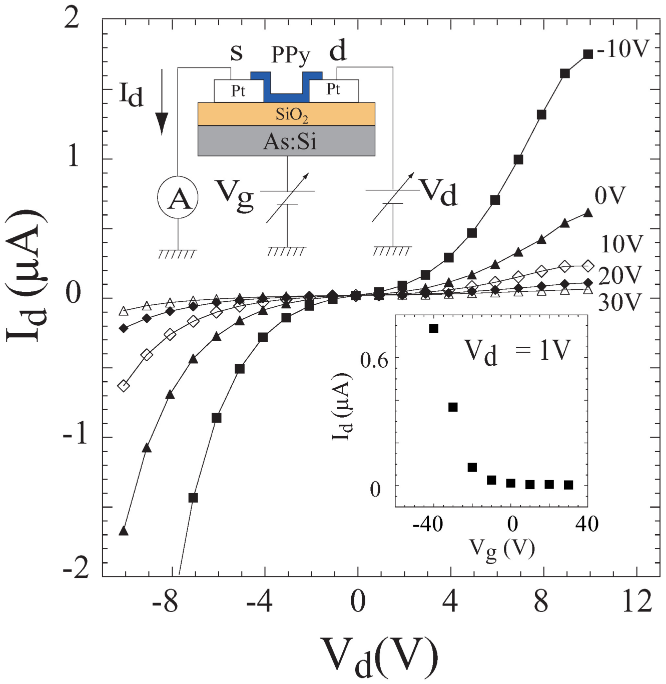

Figure 5.3: *Current-voltage characteristics (main figure) and gate voltage characteristics (lower inset) of the PPy transistor sketched in the upper inset (sample VPH07).*

The transistor behavior observed is qualitatively similar to those ones observed in other PPy transistors reported so far [26, 28]. For positive values of V_d the current-voltage characteristics agrees with the behavior of the Co-PPy-Co transistor reported by Chung [26] (see Fig. 1.26 in Chapter 1). Note that it is inconsistent with the behavior of a conventional n-MOSFET where for positive values of V_d, I_d increases by increasing V_g (see Section 1.5.2 in Chapter 1). Here, for $V_d > 0$, I_d increases by driven V_g towards negative values. Additionally, the transistor behavior in Fig. 5.3 is also in qualitative accordance with that one published by Lee [28] by using Fe(III) oxidation. The difference comes from the fact that the transistor presented here cannot be explained by the TFT transistor model [157, 158] while the Lee transistor [28] could.

As described in the literature [146], it is well established that the contact between a PPy film and a high work function metal electrode (e.g. Au and Pt) can form a Schottky barrier under certain synthesis conditions. In Chapter 4, it is also indicated that vapor-phase grown samples, when prepared at room temperature, exhibited a high contact resistance, which can be associated with the formation of a Schottky barrier between Pt and PPy. Therefore, the current-voltage characteristics of the transistor are interpreted in terms of a Schottky barrier field effect transistor [185, 186, 187, 188, 189, 190]. Assuming that hole transport dominates for all gate voltages, the transistor consists of two Schottky barriers in series, biased in opposite direction (see the sketch of the band diagram in Fig. 5.4). In addition, it is assumed that the current is mostly due to tunneling through the Schottky barriers and that thermionic emission can be neglected [188].

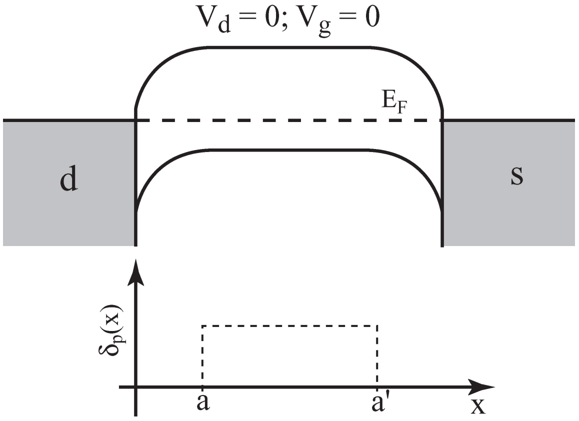

Figure 5.4: *Sketch of the band diagram of the device at* $V_d = 0$ *and* $V_g = 0$.

By setting $V_d = 0$ and $V_g = 0$, both drain and source Schottky barriers have the same width and the density of holes δ_p is constant inside of the channel (between the points a-a' in Fig. 5.4).

Next, the transistor is biased as indicated in Fig. 5.5. Accordingly, the drain contact is reverse biased, while the contact close to the grounded source is forward biased. Inside the PPy channel, the density of holes is larger close to the source contact than to the drain contact (see the continuous black line at the $\delta_p(x)$ vs. x dependence in Fig. 5.5).

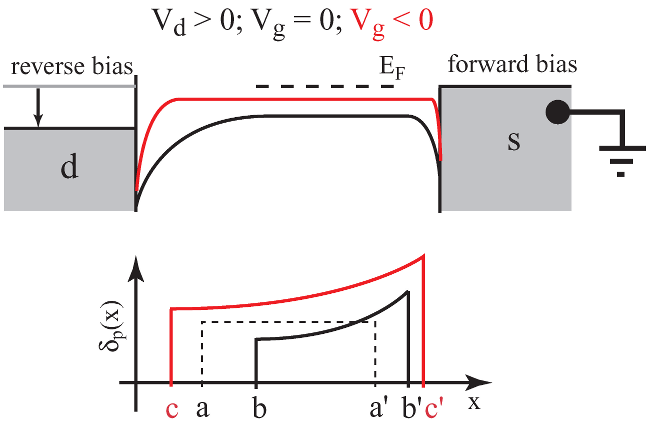

Figure 5.5: *Sketch of the band diagram of the device at* $\mathrm{V_d} > 0$, $\mathrm{V_g} = 0$ *and* $\mathrm{V_g} < 0$.

In fact, the current is dominated by the junction under reverse bias, which controls the tunneling current. Clearly, for $\mathrm{V_d} < 0$ the tunnel barrier for holes is larger at the drain than at the source contact. By driving $\mathrm{V_d}$ towards more negative values two opposing effects are expected: (a) the barrier width gets larger, which tends to decreases the tunneling current and, simultaneously, (b) the energy of the holes at the drain contact gets higher, therefore increasing of the tunneling current. The analysis of the current-voltage characteristics of the transistor indicates that the increase of the holes energy dominates over the barrier width effect. In addition, the saturation would be reached when the increase of the barrier width compensates the enhancement of the holes energy.

By decreasing $\mathrm{V_g}$ (see the continuous red line in Fig. 5.5), the charge density inside the channel increases by accumulation of holes along the interface $\mathrm{SiO_2}$/PPy. Consequently, the barrier width gets shorter at both contacts, what leads to an enhancement of the tunneling current. This explains the increase of $\mathrm{I_d}$ by driven $\mathrm{V_g}$ towards more negative values. In the opposite case, the device is biased as indicated in Fig. 5.6. The drain contact is forward biased while the contact close to the grounded source is reverse biased. Under such bias conditions, the contact resistance due to the barrier width at the drain contact can be considered negligible when compared to that one at the source contact. Thus, it can be assumed that a large amount of the voltage applied to the device drops across the source barrier, which is responsible for increasing the holes energy and controlling their tunneling. The current-voltage characteristics of the transistor for $\mathrm{V_d} < 0$ indicate that the

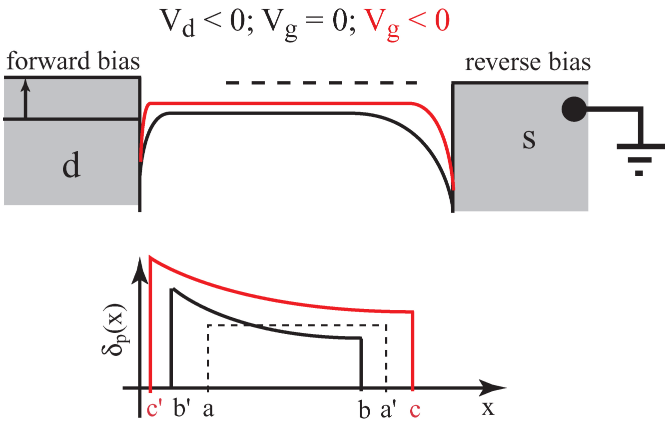

Figure 5.6: *Sketch of the band diagram of the device at* $V_d < 0$, $V_g = 0$ *and* $V_g < 0$.

tunneling current through the source barrier is mostly due to the increase of the hole energy. Once more, by driving V_g towards more negatives values, the hole density gets higher in the channel, thereby decreasing the barrier width and increasing the tunneling current.

The asymmetry in the source-drain voltage (V_d) reflects the fact that the structure of the reversely biased Schottky barrier is not symmetric under inversion of the drain - source voltage, due to the effect of the gate potential.

Devices with film thicknesses below 22 nm or above 50 nm could not be operated as transistors. Possibly, in ultrathin films, the transconductance ($g = dI_d/dV_g$) is suppressed due to interface states, while for high film thicknesses, the bulk conductivity in parallel to the gate-induced charge layer dominates the transport properties.

Fig. 5.7 (a) shows the current-voltage characteristics of another transistor (VPH11), with a 6 μm wide and 22 nm thick PPy channel. (b) shows $\mid I_d \mid$ vs. V_g for both positive and negative values of V_d.

From the IV data of the transistor VPH11 in (a) one can verify the same qualitative behavior exhibited by VPH07. Despite of this, the $\mid I_d \mid$ vs. V_g dependence in (b) shows that in VPH11, the changes in I_d due to the variation of the charge density by V_g it is not as pronounced as in VPH07. Here, probably the interface states can already change the band bending at the interface SiO_2/PPy.

For $V_d = -1$ V, the drain contact is forward biased while the contact close to the grounded source reversed biased (see Fig. 5.6). In this configuration a major fraction of the voltage applied drops across the source barrier. Therefore, by driving V_g towards more negative values,

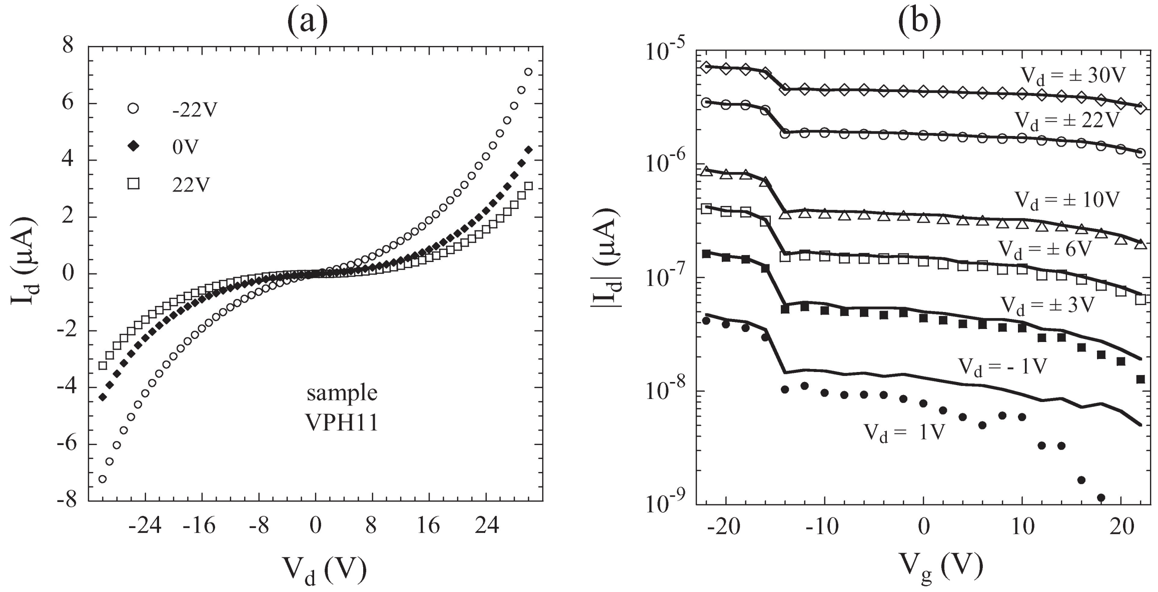

Figure 5.7: *(a) IV characteristics of the transistor VPH11, with a* 6 μm *wide and* 22 nm *thick PPy channel.(b)* | $\mathrm{I_d}$ | *vs.* $\mathrm{V_g}$ *for both positive and negative values of* $\mathrm{V_d}$*. The symbols represent the positive values of* $\mathrm{V_d}$*, while the solid line the respective negative values of* $\mathrm{V_d}$*.*

more charge is accumulated close to the interface $\mathrm{SiO_2}$/PPy and an increase of the tunneling current is observed. Instead of a continuous increase of $\mathrm{I_d}$ by $\mathrm{V_g} < 0$, a current step of unknown origin is observed at $\mathrm{V_g} = -14\,\mathrm{V}$. For positive values of $\mathrm{V_g}$, $\mathrm{I_d}$ decreases due to charge depletion at the interface.

For $\mathrm{V_d} = 1\,\mathrm{V}$, which corresponds to the situation where the drain contact is reverse biased and source contact forward biased (see Fig. 5.5), $\mathrm{I_d}$ increases by driven $\mathrm{V_g}$ towards negative values, as expected. Again, $\mathrm{I_d}$ increases with a small slope and an abrupt change is observed at $\mathrm{V_g} = -14\,\mathrm{V}$. For $\mathrm{V_g} > 0$, the decrease of $\mathrm{I_d}$ is more pronounced for $\mathrm{V_d} = 1\,\mathrm{V}$ than for $\mathrm{V_d} = -1\,\mathrm{V}$. The same it is observed when $\mathrm{V_d}$ increases towards more positive values. This behavior can be understood in terms of the effective voltage applied to the interface region $\mathrm{SiO_2}$/PPy/drain ($\mathrm{V_{eff}} \simeq \mathrm{V_g} - \mathrm{V_d}$). First, by taking into account the bias condition (see Fig. 5.5), at $\mathrm{V_g} = 18\,\mathrm{V}$, for instance, $\mathrm{V_{eff}} = 17\,\mathrm{V}$ for $\mathrm{V_d} = 1\,\mathrm{V}$. By increasing $\mathrm{V_d}$ towards more positive values, $\mathrm{V_{eff}}$ tends to increase the charge density close to the drain barrier, what is reflected in the tunneling current.

The difference between positive and negative drain voltage behavior by varying $\mathrm{V_g}$ disappears for $|\mathrm{V_d}| > 6\,\mathrm{V}$. On the other hand, the current step observed at $\mathrm{V_g} = -14\,\mathrm{V}$ remains over the whole range of

$\mathrm{V_d}$ measured and its value decreases by increasing $|\mathrm{V_d}|$.

Fig. 5.8 shows the $\mathrm{I_d}$ vs. $\mathrm{V_g}$ dependence for $\mathrm{V_d} = 30\,\mathrm{V}$ where a complete cycle, starting from $\mathrm{V_g} = 22\,\mathrm{V}$ to $\mathrm{V_g} = -22\,\mathrm{V}$ and back to $\mathrm{V_g} = 22\,\mathrm{V}$, was performed at scan rate of $100\,\mathrm{mV/s}$. The trace indicates that under the scan rate used, no hysteresis effects was observed.

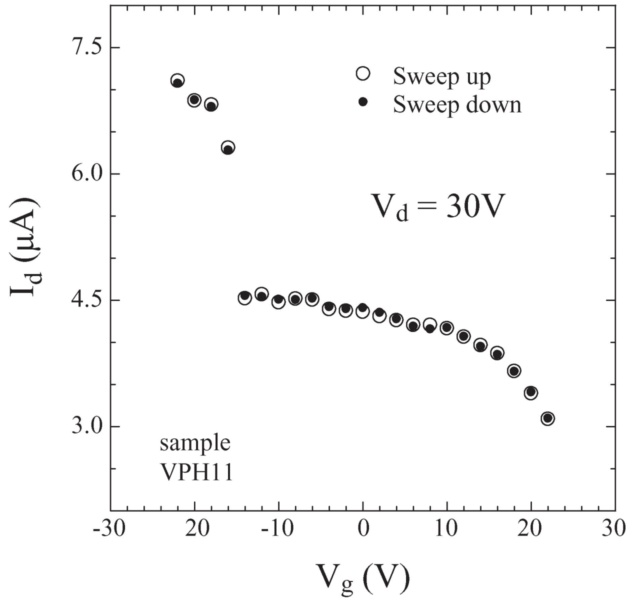

Figure 5.8: $\mathrm{I_d}$ *vs.* $\mathrm{V_g}$ *dependence for* $\mathrm{V_d} = 30\,\mathrm{V}$ *where a complete cycle, starting from* $\mathrm{V_g} = 22\,\mathrm{V}$ *to* $\mathrm{V_g} = -22\,\mathrm{V}$ *and back to* $\mathrm{V_g} = 22\,\mathrm{V}$*, was performed at scan rate of* $100\,\mathrm{mV/s}$.

Fig. 5.9 (a) shows the IV characteristics of a transistor (VPH12), with a $6\,\mu\mathrm{m}$ wide and $55\,\mathrm{nm}$ thick PPy channel and (b) presents its respective $|\ \mathrm{I_d}\ |$ vs. $\mathrm{V_g}$ for some values of $\mathrm{V_d}$.

Sample VPH12 shows the effect of the bulk conductivity on the transistor operation. This $55\,\mathrm{nm}$ thick PPy channel device shows a conductivity of $\sim 20\,\mathrm{mS/cm}$ and its charge density seems to be enough to dominate the transport. Fig. 5.9 (a) shows that a small change in $\mathrm{I_d}$ is observed due to $\mathrm{V_g}$. The same effect is better visualized in (b) where $\mathrm{I_d}$ is basically independent of $\mathrm{V_g}$ between $-30\,\mathrm{V}$ and $30\,\mathrm{V}$ for all values of $\mathrm{V_d}$.

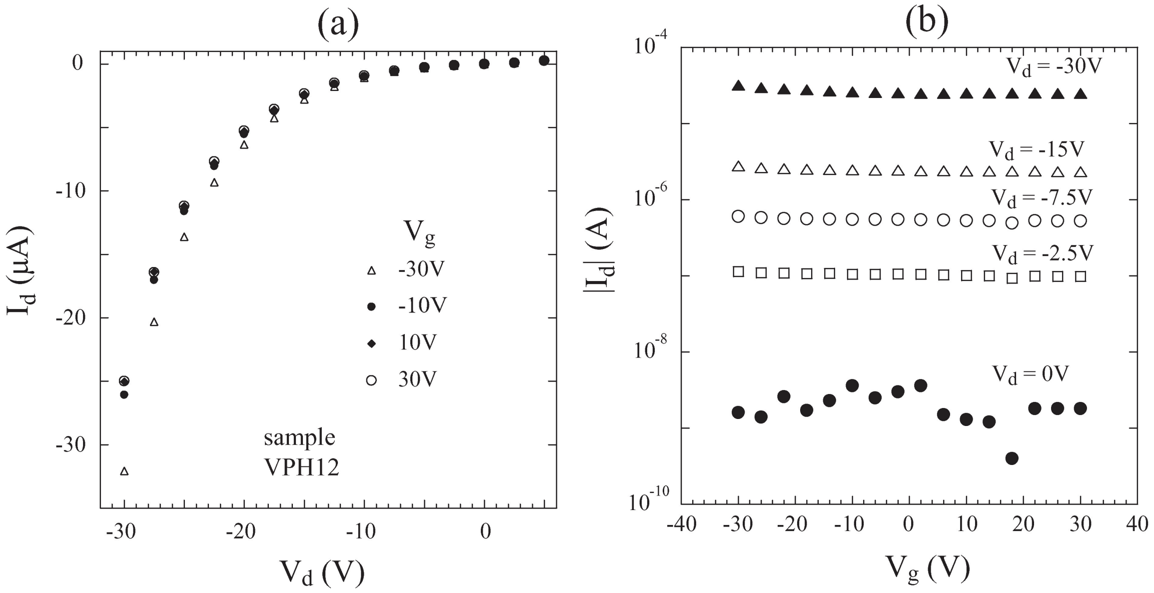

Figure 5.9: *(a) IV characteristics of the sample VPH12, with a* 6 μm *wide and* 55 nm *thick PPy channel and (b) presents its respective* | $\mathrm{I_d}$ | *vs.* $\mathrm{V_g}$ *dependence for some values of* $\mathrm{V_d}$*. The traces were measured at scan rate of* 100 mV/s.

Chapter 6

Conclusions

From the galvanostatically grown films, it has emerged that although PPy II consists of significantly shorter chains (8-12 units) as compared to PPy I (32 units), films containing more PPy II show a larger conductivity. In addition, the measurements also indicate that, as the amount of PPy II increases, the samples can be driven in the "bad metal" regime, i.e. the regime where the temperature dependence of the conductivity can be explained within the Anderson formalism. In order to explain these findings, we have argued that increasing the PPy II fraction goes along with an increased localization length of the current carrying states. Such a consideration is also supported by measurements on potentiostatically grown films, where the localization length was clearly dependent on the PPy I and II contents. A possible mechanism could be that the PPy II oligomers form a higher degree of short-range order than PPy I chains. Nevertheless, this short-range order is also determined by the method used to polymerize.

The samples grown at low potentials exhibited a large amount of PPy II, comparable to those grown galvanostatically, besides the highest value of conductivity, but without any evidence of a metal-insulator transition, even when an additional amount of charge was embedded in order to increase the doping concentration. Therefore, the constant current synthesis process seems to be more suitable to prepare locally ordered PPy films than the constant potential method. This leads to the conclusion that the amount of PPy II is strongly correlated with the localization length, but it is not the only factor which determines the crystallinity.

The induced and presumably small changes of the disorder due to changes on the growth temperature, growth potential or due to voltammetric cycling can have such a profound effect on the resistivity since, even in metallic samples, only a small fraction of the charge carriers resides in delocalized states. The presented results thus support the conclusions drawn from recent broadband reflectivity measurements by others [119, 120, 121], which indicate that 98% or more of the carriers are localized even in the metallic regime.

In the electrochemically grown samples, it can furthermore be determined which type of hopping transport takes place. The electronic transport in the galvanostatically grown films in the insulating regime, where a large amount of PPy I is present, was explained in terms of three-dimensional variable range hopping. However, a sample with the same amount of PPy I, also in the insulating regime, but prepared by potentiostatic polymerization, exhibits a temperature dependence according the Efros-Shklovskii hopping, where the transport takes place in the presence of Coulomb interaction. For the latter, regardless of the potential used to polymerize, the Efros-Shklovskii hopping dominates for all polymerization potentials available at low temperatures, while in the former, changes in the current density used to polymerize can drive the system across a metal-insulator transition. Again, the polymerization method adopted influences the electronic transport in PPy.

We found evidence that chain length and localization length are related. In order to further clarify the role of the different pyrrole oligomers for the transport properties of PPy films, it would be desirable to determine and control both the structure and the conductance on a microscopic scale. In order to reach this microscopic scale the first challenge was to solve the patterning problem.

For this purpose, a novel technique used to pattern PPy films prepared by vapor-phase polymerization was developed. This technique allows the deposition of the PPy thin films (thicknesses ranging from 6 nm to 170 nm) onto a processed silicon substrate by using $H_2O_2 : HCl$ as oxidizing agent. The films comprise a low roughness that scales with their thickness.

PPy thin films made by vapor-phase polymerization behave as granular systems, formed by grains with an egg-like structure. These grains are separated by barriers which contain a certain level of dopants. This creates a soft gap in the background of density of the states near the Fermi level of the band structure including the hard gap. The conductance of this system depends basically on both the intragrain and the intergranular conductance. A strong Coulomb interaction is observed in the IV measurements of such a PPy thin film which manifests itself in a threshold voltage at low temperatures. The localization length depends on the applied electric field. In this system, the localization length describes how much the wave function decays inside the barrier.

The patterned film was applied in devices. The PPy film is sensitive to oxygen exposure and can be used as oxygen detector. The thin film could also be employed as an active layer of a transistor, the operation of which is explained in terms of a Schottky barrier field effect transistor.

Finally, despite the fact that PPy has been intensively studied in the last years, the electronic properties of thin films (below 100 nm), which behave differently than the same material in a bulk form, still presents interesting features to be investigated. In this work, the investigation of the properties of this system has just started and the challenge to understand the conduction mechanisms of conducting polymers at a molecular level remains.

Chapter 7

Outlook

The possibility of synthesis and patterning PPy thin films gives rise to new perspectives.

First, the patterning technique allows a reduction of the structure dimensions basically down the grain size. To measure the electronic characteristics of a few or even a single grain can give access to information about the conduction mechanisms. The dominant component of the conductance is due to the intergranular conduction through ”dirty” barriers, i.e. barriers with a certain amount of dopants. Therefore, by varying the charge density via depletion or accumulation by using a gate voltage, it could become possible to change the barrier width.

Additionally, it is still not clear whether the electric-field dependence of the conductivity is an effect that really comes from Joule heating. More experiments should be performed, especially increasing the grain size in order to verify whether the minimum in the temperature dependence of the conductance can be related to the interplay between intergrain and intragranular conductance.

The research in more applied fields is also promising. Besides the oxygen sensitivity, the doping concentration in PPy increases in the presence of hydrogen peroxide. Since hydrogen peroxide is a product of several biochemical reactions, the application of patterned PPy thin film as biosensors is feasible. In addition, the patterning technique allows the integration of several micro-sensors on the same chip, which is technologically attractive.

The research regarding the properties of the Schottky barrier field effect transistor is another future direction. Here simulations are required to test the models.

Appendix A

Sample list

This appendix includes the list of the most important samples included in the work. Columns:

- j - the density of current used in the polymerization.
- t_p - the polymerization time.
- T_g - polymerization temperature.
- Elec. - solution used to polymerization.
- Process - additional process in which the sample was submitted after polymerization. The additional processes like, reduction and CV are made in the monomer-free solution used to polymerization.
- Application - the purpose of the sample.
- transport - electric transport.
- CV - cyclic voltammetry.
- AFM - atomic force microscopy.
- UV - ultra violet-to-visible spectroscopy.

ACN* - polymerization solution: 0.5 M $TBAPF_6$, 0.5 M Py, 1% distilled water and 1% HCl in ACN.

PC* - polymerization solution: 0.5 M $LiClO_4$ and 0.5 M Py in PC.

Galvanostatically grown samples

Sample	$j\,(mA/cm^2)$	t_p	T_g(K)	Elec.	Process	Application
EG01	6.6	30 s	273	ACN*	–	transport
EG02	6.6	30 s	273	ACN*	$\frac{\text{CV}}{\text{1 cycle}}$	CV and transport
EG03	6.6	30 s	273	ACN*	$\frac{\text{CV}}{\text{2 cycles}}$	CV and transport
EG04	6.6	30 s	273	ACN*	$\frac{\text{CV}}{\text{3 cycles}}$	CV and transport
EG05	6.6	30 s	273	ACN*	$\frac{\text{CV}}{\text{4 cycles}}$	CV and transport
EG06	6.6	30 s	293	ACN*	–	transport
EG07	6.6	30 s	293	ACN*	$\frac{\text{CV}}{\text{1 cycle}}$	CV and transport
EG08	6.6	30 s	293	ACN*	$\frac{\text{CV}}{\text{2 cycles}}$	CV and transport
EG09	6.6	30 s	293	ACN*	$\frac{\text{CV}}{\text{3 cycles}}$	CV and transport
EG10	6.6	30 s	293	ACN*	$\frac{\text{CV}}{\text{4 cycles}}$	CV and transport
EG11	0.36	3 min.	293	ACN*	$\frac{\textit{reduction}}{-1.2\,\text{V}}$	UV
EG12	0.06	3 min.	243	ACN*	$\frac{\textit{reduction}}{-1.2\,\text{V}}$	UV
EG13	0.06	3 min.	293	PC*	$\frac{\textit{reduction}}{-1.2\,\text{V}}$	UV

Potentiostatically grown samples

Sample	V_p(V)	$\mathrm{t_p}$	$\mathrm{T_g}$(K)	Electrolyte	Process	Application
EP01	0.52	24 hours	243	PC*	$\frac{\text{CV}}{4\,\text{cycle}}$	CV
EP02	0.60	15 hours	243	PC*	$\frac{\text{CV}}{4\,\text{cycle}}$	CV
EP03	0.65	1 hour	243	PC*	$\frac{\text{CV}}{4\,\text{cycles}}$	CV
EP04	0.70	30 min.	243	PC*	$\frac{\text{CV}}{4\,\text{cycles}}$	CV
EP05	0.75	20 min.	243	PC*	$\frac{\text{CV}}{4\,\text{cycles}}$	CV
EP06	0.90	10 min.	243	PC*	$\frac{\text{CV}}{4\,\text{cycles}}$	CV
EP07	1.00	60 s	243	PC*	$\frac{\text{CV}}{4\,\text{cycle}}$	CV
EP08	1.20	5 min.	243	PC*	$\frac{\text{CV}}{4\,\text{cycles}}$	CV
EP09	1.40	5 min.	243	PC*	$\frac{\text{CV}}{4\,\text{cycles}}$	CV
EP10	1.60	5 min.	243	PC*	$\frac{\text{CV}}{4\,\text{cycles}}$	CV
EP11	0.52	24 hours	243	PC*	-	transport
EP12	0.60	15 hours	243	PC*	-	transport
EP33	0.65	1 hour	243	PC*	-	transport
EP14	0.70	30 min.	243	PC*	-	transport
EP15	0.75	20 min.	243	PC*	-	transport
EP16	0.90	10 min.	243	PC*	-	transport
EP17	1.00	60 s	243	PC*	-	transport
EP18	1.20	5 min.	243	PC*	-	transport
EP19	1.40	5 min.	243	PC*	-	transport
EP20	1.60	5 min.	243	PC*	-	transport
EP21	0.52	24 hours	243	PC*	-	transport
EP22	0.52	24 hours	243	PC*	$\frac{recharge}{0.60\,\text{V}}$	transport
EP23	0.52	24 hours	243	PC*	$\frac{recharge}{0.65\,\text{V}}$	transport
EP24	0.52	24 hours	243	PC*	$\frac{recharge}{0.70\,\text{V}}$	transport

Vapor-phase grown samples

All samples were prepared using H_2O_2 : HCl (1000:1 volume fraction) as oxidant agent and commercially available liquid Py (Aldrich) was evaporated from a source by heating it to 383 K.

Sample	Ar flux	t_p	T_g(K)	Details	Application
VPH01	0.1 l/h	30 s	293	24 hours in Ar	opt. microscopy/AFM
VPH02	0.1 l/h	3 min.	293	24 hours in Ar	patterning /AFM
VPH03	0.1 l/h	2 min.	293	4 weeks in Ar	transport/AFM
VPH04	0.1 l/h	25 min.	282	4 weeks in Ar	transport/AFM
VPH05	0.1 l/h	60 min.	277.5	4 weeks in Ar	transport/AFM
VPH06	0.1 l/h	3 min.	293	24 hours in Ar	CV
VPH07	0.1 l/h	3 min.	293	24 hours in Ar	O_2 sensor/transistor
VPH08	0.1 l/h	2 min.	293	24 hours in Ar	transport/AFM
VPH09	0.1 l/h	25 min.	282	24 hours in Ar	transport/AFM
VPH10	0.1 l/h	60 min.	277.5	24 hours in Ar	transport/AFM
VPH11	0.1 l/h	2 min.	293	24 hours in Ar	transistor
VPH12	0.1 l/h	5 min.	293	24 hours in Ar	transistor

Appendix B

Abbreviations

List of the main abbreviations and symbols used in this work.

Symbol	Explanation
ACN	Acetonitrile
Ag/AgCl	Silver-silver chloride electrode
C(f)	Capacitance as a function of the frequency
C_c	Capacitance of the contact Pt/PPy
CE	Counter electrode
CV	Cyclic voltammetry
E_c	Coulomb blockade energy
ES-VRH	Efros-Shklovskii variable range hopping
ϵ_{PPy}	Dielectric constant of the PPy
Fe(III)	Fe_3Cl_2 - Iron (III) Chloride
G	Differential conductance
I_d	Drain current
$I_{d,sat}$	Saturation current
ITO	Indium-tin oxide
L_c	Localization length in the 3D VRH
L_m	Localization length in the metallic regime
n-MOSFET	n-channel metal-oxide.semiconductor field-effect transistor
NHE	Normal hydrogen electrode
$N(E_F)$	Density of states at the Fermi level
n_{sch}	Density of the charge carriers

Symbol	Explanation
OFET	Organic field-effect transistor
OLED	Organic light-emitting diode
PANI	Polyaniline
PC	Propylene carbonate
PPy	Polypyrrole
Py	Pyrrole
$\mathrm{R_c}$	Contact resistance Pt/PPy
RE	Reference electrode
$\mathrm{R_{el}}$	Resistance of the electrolyte
ρ_{4p}	Four-probe resistivity
ρ_{PPy}	Resistivity of a PPy film
ρ_{vp}	Resistivity measured by the van der Pauw method
$\mathrm{R_s}$	Series resistor
$\mathrm{R_{2p}}$	Two-probe resistance
$\mathrm{R_{4p}}$	Four-probe resistance
SCE	Saturated calomel electrode
σ_{G}	Differential conductivity
σ_{PPy}	Conductivity of a PPy film
TFT	Thin-film-transistor
$\mathrm{V_{ac}}$	ac voltage
$\mathrm{V_{appl}}$	Potential applied by the potentiostat/galvanostat
$\mathrm{V_{bi}}$	Built-in voltage between Pt and PPy
$\mathrm{V_d}$	Drain-source voltage
$\mathrm{V_g}$	Gate voltage
VP	Vapor-phase synthesis
$\mathrm{V_p}$	Polymerization potential
$\mathrm{V_{sat}}$	Saturation voltage
$\mathrm{V_t}$	Threshold voltage
$\mathrm{V_{WE}}$	Potential of the WE

Symbol	Explanation
UV-vis	Ultraviolet-visible absorption spectroscopy
W	Reduced activation energy
WE	Working electrode
XPS	X-ray photo-electron spectroscopy
ξ	Localization length in the ES-VRH
ξ_{g}	Localization length in a granular system
3D VHR	Three dimensional (3D) variable range hopping

Publications

Papers

1. *Relationship between Chain Length, Disorder, and Resistivity in Polypyrrole Films*, C.C. Bof Bufon, J. Vollmer, T. Heinzel, P. Espindola, H. John, and J. Heinze, **J. Phys. Chem. B**. 109, 19191, 2005.

2. *A polypyrrole thin-film field-effect transistor*, C.C. Bof Bufon and T. Heinzel, **Appl. Phys. Lett.** 89, 012104, 2006.

3. *Electric-field dependence of the conductance in polypyrrole thin films*, C.C. Bof Bufon and T. Heinzel, **Manuscript in preparation**.

4. *Electronic properties of potentiostatically grown polypyrrole films*, C.C. Bof Bufon, T. Heinzel, P. Espindola, H. John, and J. Heinze, **Manuscript in preparation**.

5. *Capacitance Spectroscopy in InAs1-xPx Self Assembled Quantum Dots embedded in GaAs*, C. C. B. Bufon, E. Ribeiro, W. Carvalho Jr., and G. Medeiros-Ribeiro, **Manuscript in preparation**.

Conference contributions

1. *Relationship between Chain Length, Disorder, and Resistivity in Polypyrrole Films*, **Meeting of the German Physical Society**, Dresden, Germany, March, 27th to 31th, 2006.

2. *Preparation and characterization of a polypyrrole transistor*, C.C. Bof Bufon and T. Heinzel, **Satellitentreffen (Polymere) im Rahmen des DFG Schwerpunktprogramms OFET** , Wuppertal, Germany, October, 06th, 2006.

Bibliography

[1] R. McNeill, R. Siudak, J. H. Wardlaw, and D. Weiss *Aust. J. Chem.*, vol. 16, p. 1056, 1963.

[2] B. A. Bolto and D. E. Weiss *Aust. J. Chem.*, vol. 16, p. 1076, 1963.

[3] B. A. Bolto, R. McNeill, and D. E. Weiss *Aust. J. Chem.*, vol. 16, p. 1090, 1963.

[4] H. Shirakawa, E. J. Louis, A. G. MacDiarmid, C. K. Chiang, and A. J. Heeger *J. Chem. Soc. Chem. Commun.*, p. 578, 1977.

[5] C. K. Chiang, C. R. F. Jr., Y. W. Park, A. J. Heeger, H. Shirakawa, E. J. Louis, S. C. Gau, and A. G. MacDiarmid *Phys. Rev. Lett.*, vol. 39, p. 1098, 1977.

[6] J. H. Burroughes, D. D. C. Bradley, A. R. Brown, R. N. Marks, K. Mackay, R. H. Friend, P. L. Burn, and A. B. Holmes *Nature*, vol. 347, p. 539, 1990.

[7] C. J. Drury, C. M. J. Mutsaers, C. M. Hart, M. Matters, and D. M. de Leeuw *Appl. Phys. Lett.*, vol. 73, p. 108, 1998.

[8] Z. V. Vardeny, A. J. Heeger, and A. Dodabalapur *Synth. Met.*, vol. 148, p. 1, 2000.

[9] T. A. Skotheim, R. L. Elsenbaumer, and J. R. Reynolds, eds., *Handbook of Conducting Polymers.* New York: Marcel Dekker, 2nd edn ed., 1998.

[10] S. Asavapiriyanont, G. Chandler, G. Gunawardena, and D. Pletcher *J. Electroanal. Chem.*, vol. 177, p. 229, 1984.

[11] J. Rodriguez, H. J. Grande, and T. F. Cooper, *Handbook of Organic Conductive Molecules and Polymers.* New York: John Wiley & Sons, 1997.

[12] J. Simonet and J. R. Berthelot *Prog. Solid State Chem.*, vol. 21, p. 1, 1991.

[13] T. Ishiguro, H. Kaneko, T. Nogami, H. Ishimoto, H. Nishiyama, J. Tsukamoto, A. Takahashi, M. Yamaura, T. Hagiwara, and K. Sato *Phys. Rev. Lett.*, vol. 69, p. 660, 1992.

[14] K. Sato, M. Yamamura, T. Hagiwara, K. Murata, and M. Tokumoto *Synth. Met.*, vol. 40, p. 35, 1991.

[15] M. Yamamura, T. Hagiwara, and K. Iwata *Synth. Met.*, vol. 26, p. 209, 1988.

[16] K. Kanazawa, A. F. Diaz, W. D. Gill, P. M. Grant, G. B. Street, G. P. Gardini, and J. F. Kwak *Synth, Met.*, vol. 1, p. 329, 1980.

[17] A. Diaz, J. M. V. Vallejo, and A. M. Duran *IBM J. Res. Dev.*, vol. 25, p. 42, 1981.

[18] S. D. Marcos and O. S. Wolfbeis *Sens. Mater.*, vol. 9, p. 253, 1997.

[19] G. Bidan *Sens. Act. B*, vol. 6, p. 45, 1992.

[20] A. Malinauskas *Polymer*, vol. 42, p. 3957, 2001.

[21] L. Geng, X. Huanga, Y. Zhaoa, P. Lia, S. Wanga, S. Zhanga, and S. Wu *Sol. State Elec.*, vol. 50, p. 723, 2006.

[22] S. Cosnier *Appl. Biochem. Biotechnol.*, vol. 89, p. 127, 2000.

[23] T. F. Otero and M. Broschart *J. Appl. Electrochem.*, vol. 26, p. 205, 2006.

[24] L. Koene, W. J. Hamer, and J. H. W. D. Wit *J. Appl. Electrochem.*, vol. 36, p. 545, 2006.

[25] H.-K. Song and G. T. R. Palmore *Adv. Mater.*, vol. 18, p. 1764, 2006.

[26] H.-J. Chung, H. Jung, Y.-S. Cho, S. Lee, J.-H. Ha, J. Choi, and Y. Kuk *Appl. Phys. Lett.*, vol. 86, p. 213113, 2005.

[27] A. Mohammadi, M.-A. Hasan, B. Liedberg, I. Lundstrm, and W. R. Salaneck *Synth. Met.*, vol. 14, p. 189, 1986.

[28] M. Lee, H. Kang, H. Kang, J. Joo, A. Epstein, and J. Lee *Thin Solid Film*, vol. 477, p. 169, 2005.

[29] C. O. Yoon, H. Sung, J. H. Kim, E. Barsoukov, J. H. Kim, and H. Lee *Synth. Met.*, vol. 99, p. 201, 1999.

[30] R. Menon, C. O. Yoo, D. Moses, and A. J. Heeger, *Handbook of Conducting Polymers.* New York: Marcel Dekker, 2nd edn ed., 1998.

[31] R. S. Kohlman and A. J. Epstein, *Handbook of Conducting Polymers.* New York: Marcel Dekker, 2nd edn ed., 1998.

[32] J. Joo, J. K. Lee, S. Y. Lee, K. S. Jang, E. J. Oh, and A. J. Epstein *Macromolecules*, vol. 33, p. 5131, 2000.

[33] S. Sadki, P. Schottland, N. Brodie, and G. Sabouraud *Chem. Soc. Rev.*, vol. 29, p. 283, 2000.

[34] H. S. Kang, H. S. Kang, J. K. Lee, and J. Joo *J Nonlinear Opt Phys Mater*, vol. 13, p. 633, 2004.

[35] Y. T. Kim, R. W. Collins, K. Vedom, and D. L. Allara *J. Electrochem. Soc.*, vol. 138, p. 3266, 1991.

[36] Y. J. Qiu and J. R. Reynolds *J. Polym. Sci., Part A: Polym. Chem.*, vol. 30, p. 1315, 1992.

[37] M. T. K. Tanaka, T. Shichiri and T. Yamabe *Synth. Met.*, vol. 30, p. 271, 1989.

[38] M. T. K. Tanaka, T. Shichiri and T. Yamabe *Synth. Met.*, vol. 33, p. 389, 1989.

[39] B. L. Funt and A. Diaz, *Organic Electrochemistry: an Introduction and a Guide.* New York: Marcel Dekker, 1991.

[40] E. M. Genies, G. Bidan, and A. F. Diaz *J. Electroanal. Chem.*, vol. 149, p. 101, 1983.

[41] P. Pfluger, M. Krounbi, and G. B. Street *J. Chem. Phys.*, vol. 76, p. 3212, 1983.

[42] P. Pfluger and G. B. Street *J. Chem. Phys.*, vol. 80, p. 544, 1984.

[43] G. B. Street, *Handbook of Organic Conductive Molecules and Polymers.* New York: Marcel Decker, 1nd edn ed., 1986.

[44] R. H. Geiss, G. B. Street, W. Volksen, and J. Economy *IBM J. Res. Dev.*, vol. 27, p. 321, 1983.

[45] A. Smie and J. Heinze *J. Angew. Chem. Int. Ed. Engl.*, vol. 36, p. 363, 1997.

[46] A. Smie, A. Synowczyk, J. Heinze, P. Tschuncky, G. Gtz, and P. Buerle *J. Electroanal. Chem.*, vol. 452, p. 87, 1998.

[47] J. Heinze, H. John, M. Dietrich, and P. Tschuncky *Synth. Met.*, vol. 119, p. 49, 2001.

[48] J. Heinze, P. Tschuncky, and A. Smie *J. Solid State Electrochem.*, vol. 2, p. 102, 1998.

[49] J. Heinze, C. Willman, and P. B

[50] A. Merz, J. Kronberger, L. Dunsch, A. Neudeck, A. Petr, and L. Parkanyi *Angew. Chem.*, vol. 111, p. 1533, 1999.

[51] A. Merz, J. Kronberger, L. Dunsch, A. Neudeck, A. Petr, and L. Parkanyi *Angew. Chem. Int. Ed. Engl.*, vol. 38, p. 1442, 1999.

[52] P. Tschuncky, J. Heinze, A. Smie, G. Engelmann, and G. Komehl *J. Electroanal. Chem.*, vol. 433, p. 223, 1997.

[53] J. Heinze *Private communication*, 2005.

[54] G. B. Street, T. C. Clarke, M. T. Krounbi, K. K. Kanazawa, V. Y. Lee, P. Pfluger, J. C. Scott, and G. Weiser *Mol. Cryst. Liq. Cryst.*, vol. 83, p. 253, 1982.

[55] J. L. Bredas, B. Themans, and J. M. Andre *Phys. Rev. B*, vol. 27, p. 7827, 1983.

[56] J. L. Bredas, J. C. Scott, K. Yakushi, and G. B. Street *Phys. Rev. B*, vol. 30, p. 1023, 1984.

[57] W. K. Ford, C. W. Duke, and W. R. Salocneck *J. Chem. Phys.*, vol. 77, p. 5030, 1982.

[58] C. D. Chouvy, M. C. Bernard, H. Cachet, and C. Deslouis *Surf. Interface Anal.*, vol. 38, p. 531, 2006.

[59] A. Bard and L. Faulkner, *Electrochemical Methods: Fundamentals and Applications.* New York: John Wiley & Sons, 2004.

[60] D. Beljonne and J. L. Bredas *Phys. Rev. B*, vol. 50, p. 2841, 1994.

[61] S. M. Sze, *Physics of Semiconductor Devices.* New York: John Wiley & Sons, 2nd edn ed., 1981.

[62] J. Shewchun, J. Dubow, C. W. Wilmsen, R. Singh, D. Burk, and J. F. Wager *J. Appl. Phys.*, vol. 50, p. 2832, 1979.

[63] T. Ishida, H. Kobayashi, and Y. Nakano *J. Appl. Phys.*, vol. 73, p. 4344, 1993.

[64] H. J. Lee and S. M. Park *J. Phys. Chem. B*, vol. 108, p. 1590, 2004.

[65] S. M. Ahmed, T. Nagaoka, and K. Ogra *Analytical Sciences*, vol. 14, p. 535, 1998.

[66] M. Zhou and J. Heinze *Electrochimica Acta*, vol. 44, p. 1733, 1999.

[67] C. O. Yoon, R. M., D. Moses, and A. J. Heeger *Phys. Rev. B*, vol. 49, p. 10851, 1994.

[68] M. Su, L. Fu, N. Wu, M. Aslam, and V. Dravid *Appl. Phys. Lett.*, vol. 84, p. 828, 2004.

[69] U. S. Ramelow, J. H. Ma, and R. Darbeau *Mat. Res. Innovat.*, vol. 5, p. 40, 2001.

[70] F.-L. Cheng, M.-L. Zhang, and H. Wang *Sensors*, vol. 5, p. 245, 2005.

[71] B. Langsdorf, B. MacLean, J. E. Halfyard, J. Hughes, and P. Pickup *J. Phys. Chem. B*, vol. 107, p. 2480, 2003.

[72] I. Jureviciute and S. Bruckenstein *J. Solid State Electrochem.*, vol. 7, p. 554, 2003.

[73] D. Chowdhury, A. Paul, and A. Chattopadhyay *Langmuir*, vol. 21, p. 4123, 2005.

[74] M. Salmon, K. K. Kanazawa, A. F. Diaz, and M. Krounbi *J. Polym. Sci. Polym. Lett. Ed.*, vol. 20, p. 187, 1982.

[75] S. Khedkar and S. Radhakrishnan *Thin Solid Film*, vol. 303, p. 167, 1997.

[76] S. K. Dhawan and D. C. Trivedi *Bull. Mater. Sci.*, vol. 16, p. 371, 1993.

[77] J. Kim, D. Sohn, Y. Sung, and E.-R. Kim *Synth. Met.*, vol. 132, p. 309, 2003.

[78] B. Winther-Jensen, J. Chen, K. West, and G. Wallace *Macromolecules*, vol. 37, p. 5930, 2004.

[79] J. Jousse and L. Olmedo *Synth. Met.*, vol. 41-43, p. 385, 1991.

[80] Y. Fu, R. Weiss, P. Gan, and M. Bessette *Polym. Eng. Sci.*, vol. 38, p. 857, 1998.

[81] Y. Kamiura and F. Hashimoto *Appl. Phys. Lett.*, vol. 53, p. 1711, 1988.

[82] O. Kononchuk, K. G. Korablev, N. Yarykin, , and G. A. Rozgonyi *Appl. Phys. Lett.*, vol. 73, p. 1206, 1998.

[83] D. A. Ramappa and W. B. Henley *J. Electrochem. Soc.*, vol. 146, p. 3773, 1999.

[84] P. T. Kissinger and W. R. Heineman *J. Chem. Educ.*, vol. 60, p. 702, 1983.

[85] G. A. Mabbott *J. Chem. Educ.*, vol. 60, p. 697, 1983.

[86] S.Petrovic *Chem. Educator*, vol. 5, p. 231, 2000.

[87] M. Zhou, M. Pagels, B. Geschke, and J. Heinze *J. Phys. Chem. B*, vol. 106, p. 10065, 2002.

[88] J. Heinze, P. Tschuncky, and A. Smie *Top. Curr. Chem.*, vol. 152, p. 1, 1990.

[89] J. Heinze, *Electrochemistry of Conducting Polymers in Organic Electrochemistry.* New York: Marcel Dekker, 2001.

[90] J. Heinze, *Encyclopedia of Electrochemistry*, vol. 8. Germany: Wiley-VCH: Weinheim, 2004.

[91] M. D. Levi, C. Lopez, E. Vieil, and M. A. Vorotyntsev *Electrochimica Acta*, vol. 42, p. 757, 1997.

[92] K. Meerholz and J. Heinze *Synth. Met.*, vol. 41-43, p. 2871, 1991.

[93] M. Pagels, J. Heinze, B. Geschke, and V. Rang *Electrochimica Acta*, vol. 46, p. 3943, 2001.

[94] G. Zotti, A. Berlin, G. Pagani, G. Schiavon, and S. Zecchin *Adv. Mater.*, vol. 6, p. 231, 1993.

[95] S. W. Feldberg and J. R. Rubinstein *J. Electroanal. Chem.*, vol. 240, p. 1, 1988.

[96] M. G. Hill, J. F. Pebbeau, B. Zinger, K. R. Mann, and L. L. Miller *Chem. Mater.*, vol. 4, p. 1106, 1992.

[97] M. D. Levi, E. Lankri, Y. Gofer, D. Aurbach, and T. Otero *J. Electrochem. Soc.*, vol. 149, p. E204, 2002.

[98] N. F. Mott, *Metal Insulator Transitions.* London: Tayler and Francis, 1974.

[99] B. I. Shklovskii and A. L. Efros, *Electronic Properties of Doped Semiconductors.* Springer-Verlag, 1988.

[100] A. L. Efros and B. I. Shklovskii *J. Phys. C*, vol. 8, p. L49, 1975.

[101] N. F. Mott, *Conduction in Non-Crystalline Materials.* Oxford: Clarendon, 2nd edn ed., 1993.

[102] C. T. Black, C. B. Murray, R. L. Sandstrom, and S. Sun *Science*, vol. 290, p. 1131, 2000.

[103] A. S. Cordan, Y. Leroy, A. Goltzen, A. Ppin, C. Vieu, M. Mejias, and H. Launois *J. Appl. Phys.*, vol. 87, p. 345, 2000.

[104] A. A. Middleton and N. S. Wingreen *Phys. Rev. Lett.*, vol. 71, p. 3198, 1993.

[105] J. Zhang and B. I. Shklovskii *Phys. Rev. B*, vol. 70, p. 115317, 2004.

[106] T. B. Tran, I. S. Beloborodov, X. M. Lin, T. P. Bigioni, V. M. Vinokur, and H. M. Jaeger *Phys. Rev. Lett.*, vol. 95, p. 076806, 2005.

[107] I. S. Beloborodov, A. V. Lopatin, V. M. Vinokur, and K. B. Efetov *cond-mat/0603522*, 2006.

[108] B. I. Shklovskii *Sov. Phys. Solid State*, vol. 26, p. 353, 1984.

[109] D. Sutar, M. Mithra, R. Menon, and S. V. Subramanyam *Synth. Met.*, vol. 119, p. 455, 2001.

[110] A. Diaz and B. Hall *IBM J. Res. Dev.*, vol. 27, p. 342, 1983.

[111] M. Ogasawara, K. Funahashi, T. Demura, T. Hagiwara, and K. Iwata *Synth. Met.*, vol. 14, p. 61, 1986.

[112] R. Roy, S. K. Sen, M. Digar, and S. N. Bhattacharyya *J. Phys.: Cond. Matter.*, vol. 3, p. 7849, 1991.

[113] J. Dugdale, *The Electrical Properties of Disordered Metals.* U.K.: Cambridge University Press:Cambridge, 1995.

[114] P. A. Lee and T. V. Ramakrishnan *Rev. Mod. Phys.*, vol. 57, p. 287, 1985.

[115] A. B. Kaiser *Rep. Prog. Phys.*, vol. 64, p. 1, 2001.

[116] B. L. Altshuler and A. G. Aronov *Solid State Commun.*, vol. 46, p. 429, 1983.

[117] N. F. Mott and M. Kaveh *Adv. Phys.*, vol. 34, p. 329, 1985.

[118] W. L. MacMillan *Phys. ReV. B*, vol. 24, p. 2739, 1981.

[119] H. C. F. Martens, H. B. Brom, and R. Menon *Phys. Rev. B*, vol. 64, p. 201102, 2001.

[120] I. G. Romijn, H. J. Hupkes, H. C. F. Martens, H. B. Brom, A. K. Mukherjee, and R. Menon *Phys. Rev. Lett.*, vol. 90, p. 176602, 2003.

[121] K. Lee and A. J. Heeger *Phys. Rev. B*, vol. 68, p. 035201, 2003.

[122] K. Lee, S. Cho, S. H. Park, A. J. Heeger, C. W. Lee, and S.-H. Lee *Nature*, vol. 441, p. 65, 2006.

[123] M. Ahlskog, A. K. Mukherjee, and R. Menon *Synth. Met.*, vol. 119, p. 457, 2001.

[124] H. C. F. Martens and H. B. Brom *Phys. Rev. B*, vol. 70, p. 241201, 2004.

[125] V. G. Prigodin and K. Efetov *Phys. Rev. Lett.*, vol. 70, p. 2932, 1993.

[126] J. M. Ribo, M. C. Anglada, J. M. Hernandez, X. Zhang, N. Ferrer-Anglada, A. Chaibi, and B. Movaghar *Synth. Met.*, vol. 97, p. 229, 1998.

[127] V. Gomis, N. Ferrer-Anglada, B. Movaghar, J. M. Rib, Z. El-Hachemi, and S. H. Jhang *Phys. Rev. B*, vol. 68, p. 2003, 2003.

[128] A. S. Dhoot, G. M. Wang, D. Moses, , and A. J. Heeger *Phys. Rev. Lett.*, vol. 96, p. 246403, 2006.

[129] F. Ladieu, D. L'Hte, and R. Tourbot *Phys. Rev. B*, vol. 61, p. 8108, 2000.

[130] B. I. Shklovskii and A. L. Efros *Sov. Phys. Usp.*, vol. 18, p. 845, 1975.

[131] S. Fend and J. L. Pichard *Phys. Rev. Lett.*, vol. 67, p. 753, 1991.

[132] B. I. Shklovskii *Sov. Phys. Semicond.*, vol. 6, p. 1964, 1973.

[133] R. M. Hill *Philos. Mag.*, vol. 24, p. 1307, 1971.

[134] T. C. Clarke, J. C. Scott, and G. B. Street *IBM J. Res. Dev.*, vol. 27, p. 313, 1983.

[135] P. Pfluger, U. M. Gubler, and G. B. Street *Solid State Commun.*, vol. 49, p. 911, 1984.

[136] G. Zotti, S. Martina, G. Wegner, and A.-D. Schlter *Adv. Mater.*, vol. 4, p. 798, 1992.

[137] K. Yakushi, L. J. Lauchlan, T. C. Clarke, and G. B. Street *J. Chem. Phys.*, vol. 79, p. 4774, 1983.

[138] C. Y. Kim, D. Y. Kim, J. Y. Lee, and D. K. Moon *Synth. Met.*, vol. 69, p. 471, 1995.

[139] J. L. Bredas, R. Silbey, D. S. Boudreaux, and R. R. Chance *J. Am. Chem. Soc.*, vol. 105, p. 6555, 1983.

[140] L. Xu, W. Chen, A. Mulchandani, and Y. Yan *J. Angew. Chem. Int. Ed. Engl.*, vol. 44, p. 6009, 2005.

[141] M. F. Suarez and R. G. Compton *J. Electroanal. Chem.*, vol. 462, p. 211, 1999.

[142] J. M. Ko, H. W. Rhee, S.-M. Park, and C. W. Kim *J. Electrochem. Soc.*, vol. 137, p. 905, 1990.

[143] B. J. Hwang, Y.-B-Shim, and S.-M. Park *J. Electrochem. Soc.*, vol. 147, p. 2252, 2000.

[144] H. J. Lee and S. M. Park *J. Phys. Chem. B*, vol. 109, p. 13247, 2005.

[145] Y.-M. Uang and T.-C. Chou *Electronalysis*, vol. 14, p. 1564, 2002.

[146] C. N. Van and K. Potje-Kamloth *J. Phys. D: Appl. Phys.*, vol. 33, p. 2230, 2000.

[147] A. Assadi, A. Spetz, M. Willander, C. Svensson, I. Lundstrm, and O. Ingan

[148] T. Hanawa, S. Kuwabata, and H. Yoneyama *J. Chem. Soc., Faraday Trans. I*, vol. 84, p. 1587, 1988.

[149] K.-S. Teh and L. Lin *J. Micromech. Microeng.*, vol. 15, p. 2019, 2005.

[150] J.-H. Kim, B.-G. Kim, J.-B. Yoon, E. Yoon, and C.-H. Han *Sens. Actuator A*, vol. 95, p. 108, 2002.

[151] J. C. Scott, P. Pfluger, M. T. Krounbi, and G. B. Street *Phys. Rev. B*, vol. 28, p. 2140, 1983.

[152] P. Rapta, A. Neudeck, A. Bartl, and L. Dunsch *Electrochimica Acta*, vol. 44, p. 3483, 1999.

[153] D. Schmeiβer, A. Bartla, L. Dunsch, H. Naarmann, and W. G

[154] N. Kemp, G. Fianagan, A. Kaiser, H. Trodahl, B. Chapman, A. Partridge, and R. Buckley *Synth. Met.*, vol. 101, p. 434, 1999.

[155] K. Mizoguchi, N. Kachi, H. Sakamoto, K. Yoshioka, S. Masubuchi, and S. Kazama *Solid State Commun.*, vol. 105, p. 81, 1998.

[156] M. Shur, *Physics of Semiconductor Devices.* Engleewood Cliffs: Prentice-Hall, 1990.

[157] G. Horowitz *Adv. Mater.*, vol. 10, p. 365, 1998.

[158] G. Horowitz *Adv. Mater.*, vol. 8, p. 177, 1996.

[159] P. K. Weimer *Proc. IRE.*, vol. 20, p. 1492, 1962.

[160] T. Riihisaari, A. Kiviranta, S. Lehto, J. Likonen, S. Ernen, E. Sandell, J. Virtanen, and M. Viitanen, *Cleaning Technology in Semiconductor Device Manufacturing VI.* Pennington, NJ: Electrochemical Society, 2000.

[161] A. Sehgal, M. R. Yalamanchili, and J. J. Rosato *Future Fab. Intl.*, vol. 10, p. 1, 2001.

[162] C. D. Dimitrakopoulos and P. R. L. Malenfant *Adv. Mater.*, vol. 14, p. 99, 2002.

[163] P. Buerle, T. Fischer, B. Bidlingmaier, A. Stabel, and J. P. Rabe *Angew. Chem., Int. Ed. Engl.*, vol. 34, p. 303, 1995.

[164] P. Buerle, T. Fischer, B. Bidlingmaier, A. Stabel, and J. P. Rabe *Angew. Chem.*, vol. 107, p. 335, 1995.

[165] L. J. van der Pauw *Philips Res. Repts.*, vol. 13, p. 1, 1958.

[166] H. Koezuka and S. Etoh *J. Appl. Phys.*, vol. 54, p. 2511, 1983.

[167] P. S. Abthagir and R. Sarashwati *J. Appl. Polym. Sci.*, vol. 81, p. 2127, 2001.

[168] A. G. Zabrodskii and K. N. Zinoveva *Sov. Phys. JETP*, vol. 59, p. 425, 1984.

[169] N. W. Ashcroft and N. Mermin, *Solid State Physics.* New York: Holt Rinehart & Winston, 2002.

[170] D. Belitz and K. I. Wysokinski *Phys. Rev. B*, vol. 36, p. 9333, 1987.

[171] Y. S. Cohen, M. Levi, and D. Aurbach *Langmuir*, vol. 23, p. 9804, 2003.

[172] M. Zhou and J. Heinze *J. Phys. Chem. B*, vol. 103, p. 8443, 1999.

[173] D. E. Khmelnitskii and A. I. Larkin *Solid State Commun.*, vol. 39, p. 1069, 1981.

[174] R. Menon, C. O. Yoon, D. Moses, and A. J. Heeger *Phys. Rev. B*, vol. 48, p. 17685, 1993.

[175] D. Basko *Private communication*, 2006.

[176] N. Apsley and H. P. Hughes *Philos. Mag.*, vol. 31, p. 1327, 1975.

[177] A. V. Dvurechenskii, V. A. Dravin, , and A. I. Yakimov *JETP Lett.*, vol. 48, p. 155, 1988.

[178] D. Yu, C. Wang, B. L. Wehrenberg, and P. Guyot-Sionnest *Phys. Rev. Lett.*, vol. 92, p. 216802, 2004.

[179] P. Dai, Y. Zhang, and M. P. Sarachik *Phys. Rev. B*, vol. 45, p. 3984, 1992.

[180] P. Dai, Y. Zhang, and M. P. Sarachik *Phys. Rev. B*, vol. 46, p. 6724, 1992.

[181] A. N. Aleshin, H. J. Lee, Y. W. Park, and K. Akagi *Phys. Rev. Lett.*, vol. 93, p. 196601, 2004.

[182] A. N. Aleshin, H. J. Lee, S. H. Jhang, H. S. Kim, K. Akagi, and Y. W. Park *Phys. Rev. B*, vol. 72, p. 153202, 2005.

[183] M. Bockrath, D. H. Cobden, J. Lu, A. G. Rinzler, R. E. Smalley, L. Balents, and P. L. Mceuen *Nature(London)*, vol. 397, p. 598, 1999.

[184] J. Kakalios, R. A. Street, and W. B. Jackson *Phys. Rev. Lett.*, vol. 59, p. 1037, 1987.

[185] J. R. Tucker, C. Wang, and P. S. Carney *Appl. Phys. Lett.*, vol. 65, p. 618, 1994.

[186] M. Jang, K. Kang, and S. Lee *Appl. Phys. Lett.*, vol. 82, p. 2718, 2003.

[187] R. Martenl, C. Lavoie, J. Appenzeller, K. K. Chan, J. Tersoff, and P. Avouris *Phys. Rev. Lett.*, vol. 87, p. 256805, 2001.

[188] J. Appenzeller, J. Knoch, V. Derycke, R. Martelm, S. Wind, and P. Avouris *Phys. Rev. Lett.*, vol. 89, p. 126801, 2002.

[189] V. Derycke, R. Martel, J. Appenzeller, and P. Avouris *Appl. Phys. Lett.*, vol. 80, p. 2773, 2002.

[190] S. Heinze, J. Tersoff, R. Martel, V. Derycke, J. Appenzeller, and P. Avouris *Phys. Rev. Lett.*, vol. 89, p. 106801, 2002.

Acknowledgements

There are several people I wish to acknowledge for helping me during the difficult, yet rewarding, path towards a Ph.D. Without them, it would have been harder for me to overcome the challenges.

First, I would like thank to Prof. Dr. Thomas Heinzel, who gave me the opportunity to work in this project, encouraged me to perform the work and provided me with all technical and moral support during all these years. He supported me in developing my own ideas, while being there to guide me at the same.

I would like to extend my thanks to Dr. Marcel Lorenz and Stefan Meckler, former members of this group, for supporting me in working out the necessary arrangements when first arrived in Germany.

I also gratefully acknowledge Prof. Dr. Jürgen Heinze, from the Department of Physical Chemistry of the Freiburg University, for valuable discussions and cooperation in the electrochemical branch of this project. All the solutions used for electrochemical polymerization and cyclic voltammetry were kindly prepared by Pamela Espindola, to whom I am also thankful for constant disposition to help. I also acknowledge Hermann John for the UV-vis measurements.

I am grateful to Judith Vollmer for her help in some of the synthesis and measurements of the electrochemically grown films.

I am thankful to Harald Götz and Doru Gherban for the technical support in this project.

I am very grateful to our secretary, Klaudia Lütjens, for the time spent to help me solving the endless bureaucracy.

I will remember my colleagues Stefan Hugger, Dr. Mihai Cerchez and Marcus Friedrich. I am grateful for their friendship and translation.

I also acknowledge Prof. Dr. Klaus Schierbaum to be the co-referee of this thesis.

I am thankful the financial support of the DFG SFB 428, the ”Fonds der Chemischen Industrie", and of the Heinrich-Heine-Universität Düsseldorf.

I am extremely grateful to my family in Brazil, that even far from me, always supported me.

All my gratitude goes to my wife Dina, for her love, patience and support. Without her the life certainly would be harder. I need also to thank my five months daughter Johanna for waking me up every day at 5 a.m. to write this thesis.

Finally I am thankful to God for bringing wonderful people into my life, and for everything I have achieved up to this day.

Die hier vorgelegte Dissertation habe ich eigenständig und ohne unerlaubte Hilfe angefertigt. Die Dissertation wurde in der vorgelegten oder in ähnlicher Form noch bei keiner anderen Institution eingereicht. Ich habe bisher keine erfolglosen Promotionsversuche unternommen.

Düsseldorf, den 30.11.2006

Carlos César Bof' Bufon